Marcin Michał Kożak

Development of Thulium-Doped Fluoride Fiber Amplifers
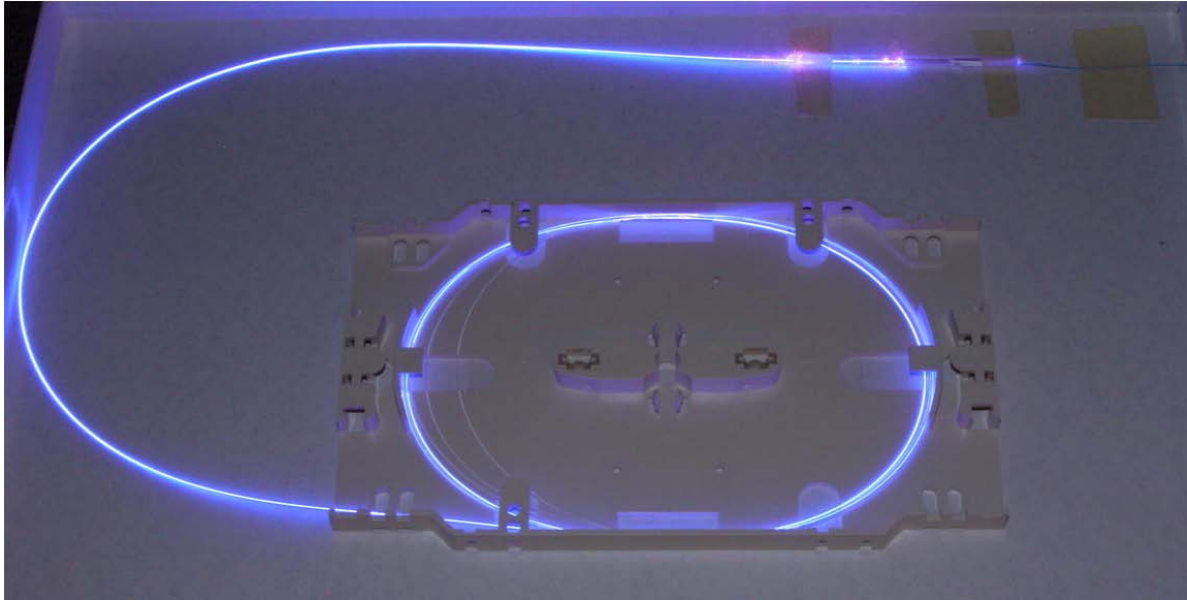
Development of Thulium-Doped Fluoride Fiber Amplifiers

Von der Fakultät für Elektrotechnik und Informationstechnik
der Technischen Universität Carolo-Wilhelmina zu Braunschweig

zur Erlangung der Würde

eines Doktor-Ingenieurs (Dr.-Ing.)

genehmigte Dissertation

von:	Dipl.-Ing. Marcin Michał Kożak
aus:	Oława (Polen)
eingereicht am:	03.11.2005
mündliche Prüfung am:	22.12.2005

Referenten: Prof. Dr.-Ing. Wolfgang Kowalsky
                Prof. Dr. rer. nat. Andreas Waag

2005

1. Auflage, 2006
Gedruckt auf säurefreiem Papier

Acknowledgements

Kurzzusammenfassung

Ziel dieser Arbeit ist die Entwicklung von Thulium-dotierten Faserverstärkern (TDFA) und deren Untersuchungen in verschiedenen Pumpanordnungen. Im Vergleich zum Erbiumdotierten Faserverstärker (EDFA), der mittlerweile in vielen optischen Kommunikationssystemen vorhanden ist, bietet der TDFA die Möglichkeit, die Bandbreite von derzeitigen Übertragungssystemen zu erweitern. Weil viele Energieniveaus am Verstärkungsprozess beteiligt sind, ist die Entwicklung eines TDFAs sehr aufwändig. Das liegt zum einen daran, dass die Anzahl von Energieniveaus, die für den Verstärkungsprozess relevant sind, im TDFA grösser ist als in EDFA, zum anderen erfolgt die Verstärkung hier zwischen zwei angeregten Energieniveaus. Außerdem sorgt ein Zwischenniveau dafür, dass das obere Verstärkerniveau aufgrund schneller nicht strahlender Übergänge entleert wird. Deshalb werden speziele Fluoridglasfasern (ZBLAN) verwendet, die die Effizienz des Emissionsüberganges deutlich erhöhen.

Nach einer kurzen Einleitung, in der die aktuellen optischen Übertragungssysteme präsentiert werden, erfolgt eine Darstellung verschiedener Verstärkertypen der optischen Nachrichtentechnik mit dem Fokus auf Seltenerd-dotierten Faserverstärkern. Anschließend wird die Funktionsweise eines TDFAs erläutert und seine Grundparameter, wie Gewinn, Rauschzahl und Pumpwirkungsgrad, definiert.

Der experimentelle Teil dieser Arbeit beginnt mit spektroskopischen Untersuchungen an zwei unterschiedlichen Thulium-dotierten Fluoridgläsern (ZBLAN und IBZP). Die Emissions- und Absorptionsübergänge wurden identifiziert und gemessen. Außerdem wurden auch Absorptionsübergänge gemessen, die aus dem ersten angeregten Zustand erfolgen. Dafür wurde eine neuartige Messmethode eingesetzt. Alle Spektren wurden anschließend in Absorptions- und Emissionsquerschnitte für die nachfolgenden Berechnungen und Vergleiche umgerechnet. Außerdem wurden auch die Lebensdauern beider Verstärkerniveus und das Konzentrationsquenching ausführlich untersucht. Abschließend wurden die Messergebnisse mit den Werten aus der Literatur verglichen.

Weil mehrere Laserquellen mit verschiedenen Wellenlängen in den TDFA-Aufbauten zum Einsatz kamen, waren auch spezielle Faserkoppler nötig. Mit Hilfe eines einfachen Simulationsmodells kann die Entwicklung derartiger Koppler wesentlich vereinfacht worden. Die Modellergebnisse werden mit den Messungen verglichen.

Eine stabile und zuverlässige Verbindungstechnik zwischen Quarz- und ZBLAN-Glasfasern ist ebenfalls ein wichtiger Aspekt, der aufgrund von verschiedenen Temperatureigenschaften beider Gläser intensiv untersucht wurde. In dieser Arbeit wird eine Klebespleisstechnik eingesetzt. Die Untersuchungsergebnisse dieser Spleisstechnik sind in einem weiterem Kapitel zusammengefasst.

Die aus den experimentellen Teil dieser Arbeit gewonnenen Ergebnisse werden verwendet, um einen TDFA zu simulieren und anschließend zu realisieren. Es werden Messergebnisse des aufgebauten TDFA für verschiedene Pumpkonfigurationen vorgestellt. Abschließend wird ein neuartiger TDFA, der mit einem Faserlaser bei 1900 nm und einer externen Laserdiode bei 805 nm gepumpt wird, präsentiert.

Contents

Introduction

Rare-earth doped fiber amplifiers are key devices in high capacity long haul optical telecommunication systems. Their best representative is the compact erbium-doped fiber amplifier (EDFA), which since 90's of the last century found many applications in terrestrial and submarine optical links [1]. They forced a rush development of the new communication era, in which the interpersonal communication changed the operation domain from electrical to optical. The limitations of electronic telecommunications such as low frequency of the transmitted signals or easiness to intercept were simply overcome by using optical fibers. Moreover, due to the enormous transmission bandwidth of the fiber (about 50 THz compared to 1 GHz in the case of advanced copper twisted pair cables) the capacity of transmission systems reaches totaly new dimensions. The change from electrical to optical telecommunication was an impulse to develop more efficient transmission techniques as wavelength- or time-division multiplexing which help to make effectively use of the transmission bandwidth.

Nowadays, the transparent optical networks operate mainly in the wavelength range 1530 to 1570 nm employing EDFAs. The WDM technique with increasing bitrates per channel and decreasing channel spacing are used to assure high data capacity of the longhaul systems. Unfortunately, due to the limitations of the detectors such an evolution of the transmission systems was slew down. The detectors used in receiver units are typically polarization and phase insensitive and detect the intensity of the signal radiation with maximum 1 bit/s of data rate for each Hz of optical bandwidth in a single transmission fiber. It limits the capacity of transmission systems based on EDFAs and gain-shifted EDFAS to 10 Tbit/s. Although this value may seem to be very large (it is equivalent to 160 million ISDN connections or 5 million video streams 2 Mbit/s each), the experiments with similar capacities were already reported [2].

To avoid the mentioned capacity limit, a new generation of polarization or phase sensitive transmitters and receivers has to be developed or new transmission bands have to be opened for signal amplification. Since the total available bandwidth is 5 times larger than actually used, the second solution seems to be easy to realize. Thulium-doped fiber amplifier (TDFA) seems to be one of the most suitable candidates to upgrade EDFA-based longhaul optical links. First experiments with TDFAs were performed already in 1993, but the complexity of the amplifier and the still sufficient capacity of today's transmission systems are the factors, which delay its commercial premiere.

Unfortunately, the development of the TDFA is much more complicated than that of EDFA. The problem starts with many energy levels involved in the amplification process. In contrast to the EDFA, amplification occurs between two excited levels. Moreover, there is one

energy level between the upper and lower amplification level leading to a fast non-radiative decay. The depopulation of the upper energy level occurs due to multiphonon relaxation. Phonons are the quantized vibrations of the glass matrix and its number needed to bridge the given energy gap is different in silica and fluoride glasses. The energy gap of $1000\,\mathrm{cm}^{-1}$ is bridged by 1 phonon in silica but 2 phonons in fluoride glasses. High maximum phonon energy in silica glass limits the efficiency of the radiative transitions in the amplifier. For that reason glasses with low maximum phonon energy are the best hosts for the amplifier. On the other hand, the predominant ionic type of bindings in the fluoride glass matrix, which causes decrease of the phonon energy results also in impair of the thermal and mechanical properties of the fibers made out of the fluoride glass. This fact hinders its connection to the silica transmission fiber.

Since many energy levels are involved in the amplification process, several pumping schemes of the amplifier are possible. Moreover, the TDFA employs two-stage pumping, for which pumps at different wavelengths are used. They are combined with the signal wavelength in a single fiber using special WDM couplers, which are commercially not available. All these issues make the TDFA development not trivial, and their solutions are of basic importance for TDFA performance.

The advanced study on TDFA presented in this work consists of seven chapters, the contest of which is given below.

Chapter 1. This chapter provides an introduction into the optical transmission systems. The amplifier types present in different fiber links are described with the special attention to their particular applications. Besides semiconductor and Raman amplifiers the state-of-art for rare-earth doped fiber amplifiers in S-, C- and L-band is given and a comparison of amplifier types for the S-band is given.

Chapter 2. In this chapter the operation principle of the thulium-doped fiber amplifier is described. Also the relevant transitions in thulium-doped fluoride glass (ZBLAN) are presented and their importance for the amplifier's performance is discussed. Since fluoride fibers are chosen as host glass for the TDFA, the features of low phonon energy glasses are compared with that of silica glass. Finally, the definitions of basic amplifier parameters as gain, noise figure, and power conversion efficiency are provided.

Chapter 3. The analysis of the amplification process in TDFA provided in previous chapter shows that special attention has to be paid on spectroscopic investigations of thulium in the glass matrix. Therefore a number of ground- and excited-state absorption as well as emission lines was investigated in two fluoride glass systems (ZBLAN and IBZP). Also the life time measurements were performed for both glass types and the concentration quenching process was observed for highly thulium-doped samples.

Chapter 4.   The problem of several different radiation sources needed for the amplification process and their combination in a single fiber is subject of this chapter. The development of different types of fiber couplers was supported by a simple coupler model, the description of which is provided here. Finally, examples of various 2λ- and 3λ-WDM couplers are given.

Chapter 5.   In this chapter the differences of thermal and mechanical properties of fluoride and silica glasses are discussed. Because of the fact that both fiber types can not be spliced using welding arc makes the development of a new stable and reliable connection technique necessary. As shown in lifetime measurements described in this chapter, the glue-splice technique seems to be a solution of this connection problem. Its limitations influencing the operation under high power conditions indicates the direction of further investigations.

Chapter 6.   The results of investigations described in the three previous chapters are used here to simulate the complete TDFA setup. The amplifier model presented in this chapter is used to simulate the performance of the TDFA, however due to many unknown parameters required for amplifier's description the simulation results are not quantitatively comparable with measurements. The spacial aspects of TDFA operation as gain-shift and amplification in TDFA operating with a cooperative fiber laser at about 1900 nm are given as simulation examples.

Chapter 7.   In this chapter measurements of the thulium-doped fiber amplifier in different pump configurations are reported. Special attention is given to the single-wavelength pumping scheme employing high-power 1056 nm laser diodes as a pump sources. Strong cross-relaxation observed for highly thulium-doped fibers is an explanation for efficient operation of this type of amplifier. As next, the investigations on typical double-wavelength pumping schemes are reported. Section 7.4 collects the measurement results of the advanced pumping scheme using a fiber laser at 1849 nm to depopulate the lower amplification level and making possible to pump the amplifier with just an 805 nm pump laser.

1 Optical transmission systems

The rush development of the optical transmission systems in the last years of the 20th century clearly shown, that the interest in the new applications (e.g. video on demand, interactive media) of the optical telecommunications systems will drastically increase. This means increase in bandwidth demands, which can be satisfied by using fiber transmission bandwidths besides the standard C- and L- band and/or developing of optical transmission systems, which allow to transmit many signal channels. This forced the development of two main transmission techniques: optical time division multiplexing (TDM) and wavelength division multiplexing (WDM).

In the time domain multiplexing systems many single signals can be transmitted over a single transmission path. Each lower-speed signal is time-sliced into one high-speed transmission. For example, four incoming 1000 bit/s signals can be interleaved into one 4000 bit/s signal. The receiving end divides the single stream back into its original signals [3]. The bottleneck of TDM systems is the dispersion of the fiber, which limits the transmission distances for the higher capacities. However, by using dispersion compensation techniques it is possible to transmit high-capacity signals over long distances [4].

In the WDM technique several wavelengths are used to simultaneously transfer the data over a single fiber. Each of the wavelengths is modulated by the data stream (text, video, voice), which dramatically increases the capacity of the transmission systems. Typical channel distance in the commercial WDM systems is 200, 100 or 50 GHz. Applying several wavelengths with channel spacing of 100 GHz it is possible to increase the capacity of the transmission systems to several Tbit/s. The wavelength division multiplexing is present in different variations, for example course-WDM (CWDM) or dense-WDM (DWDM).

For the short transmission distances the best solution for WDM systems seems to be CWDM, also known as "wide WDM". In this technique several channels are transmitted simultaneously and the channel spacing is much bigger than in standard WDM. Typical spacing between the channels is up to 20 nm (2.5 THz) and transmission is realized for relatively short distances (up to 60 km). The wider spacing tolerates higher temperature fluctuation, which makes the CWDM a low-cost version of a WDM system. Its significant cost advantage is caused by the fact, that the signal lasers do not have to be thermally stabilized and can be modulated directly by changing the drive current. Such a systems operate in the wavelength range of 1270 and 1610 nm, but due to larger channel spacing this technique is not suitable to transmit high data capacities. Nevertheless, the experiments with 40 Gbit/s transmission were reported in [5, 6].

The dense wavelength division multiplexing systems are characterized by the high total transmission capacity (up to several Tbit/s). Such a high capacity is achieved by combining many single transmission channels in one optical data stream. The wavelength of the signal can be chosen from any of the transmission bands, which cover more than 450 nm optical bandwidth. This bandwidth is divided into several bands, according the ITU recommendation G.694.1 (06/02) [7] as shown in figure 1.1.
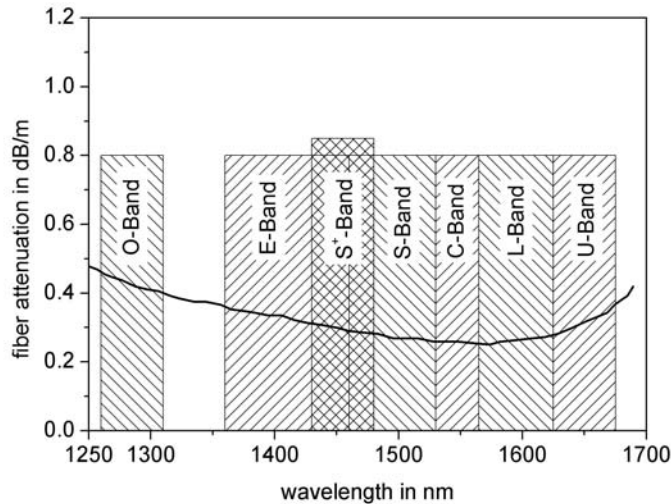
Figure 1.1: The normalized ITU bands for optical transmission systems

The broadband DWDM systems operate in more than one band. Therefore the signal bandwidth can not be covered by the single amplifier. As result one has to use a separate amplifier for each transmission band. For the most common C- and L-band erbium-doped fiber amplifiers (EDFA) are used. The signals around 1300 nm (O- or E-band) may be amplified by the praseodymium or neodymium doped fiber amplifiers, however due to the narrow flat gain bandwidth these amplifiers are not very suitable for multichannel WDM systems. The natural extension of present systems basing on EDFA are the thulium-doped fiber amplifiers (TDFA). They operates in the S- and S^+-band and reach up to 30 dB gain [8], but in contrast to EDFA they can be effectively realized in low phonon energy glasses like ZBLAN only. The transmission capacities of DWDM depends on the number of channels and their spacing and reach more than 10 Tbit. As an example 3.08 TBit/s transmission using 77 channels with the single capacity of 42.7 Gbit/s was reported in [9]. The channel spacing was 0.8 nm and to cover the whole amplification region, EDFAs and Raman amplifiers were used. The largest reported

transmission capacity of almost 11 TBit/s was achieved for 230 optical channels spaced with 100 GHz (0.8 nm) located in S-, C- and L- band and described in [10].

The large enthusiasm and research activities on the telecommunication market were slowed down after the "dot-com collapse" and in the meantime the research projects concentrate on more efficient usage of the current transmission systems working in C- and partially in L-band. However, one can expect, that the problems with non-linear effects in DWDM systems and growing bandwidth demand will force the development of new rare-earth doped fiber amplifiers like the TDFA.

In the next sections, different types of amplifiers used in optical communications systems are briefly presented. They are divided in three groups according to their operation principle, manufacturing process and/or application field.

1.1   Semiconductor amplifiers in optical communication systems

The semiconductor optical amplifiers (SOA), schematically shown in figure 1.2, are constructed similar to laser diodes, but without end mirrors.
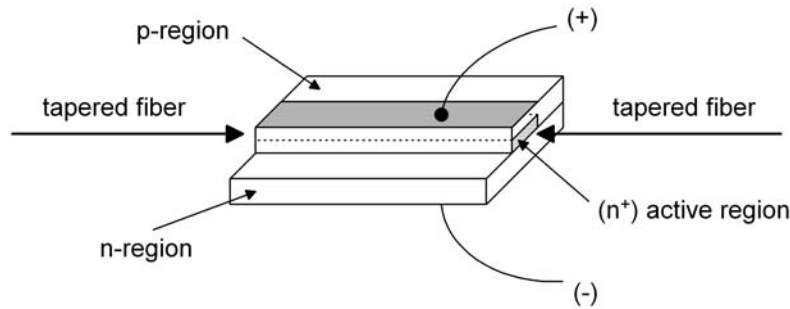
Figure 1.2: Schematic diagram of an SOA

The active region in the semiconductor amplifier generates optical gain due to stimulated emission. The operation principle bases on the pumping process, which is realized electrically by current injection. The electrons are excited from the valence to the conductive band by absorbing the energy which is higher than the energy gap in semiconductor. This results with the formation of the holes in the valence band and free electrons in the conductive bands and finally with population inversion. The signal is amplified due to the stimulated emission, but the accompanying spontaneous emission leads to noises at the signal output. The amplification bandwidth of the SOA is larger than 30 nm, which is comparable with that of EDFA.

Except of standard application of SOAs as preamplifier, in-line amplifier and postamplifier they found also many others application fields. One uses them as wavelength converters, optical gates, optical logic, multiplexers or optical pulse generators [11]. For these applications amplifiers are driven in saturation mode, where non-linear effects play an significant role.

Semiconductor amplifiers found also many applications in metropolitan area networks, which in contrast to long-haul systems are using less number of WDM channels per fiber and the transmission distances are relatively short [12]. The semiconductor amplifiers are commonly used as channel power equalizers [13]. This decreases the complexity of the power splitting-nodes and significantly reduces the costs of the networks. In the local access star passive optical networks the SOAs are used to amplify signals in less critical upstream [14]. Their low costs and broad application spectrum makes the SOAs one of the important devices for optical telecommunication systems.

1.2   Raman amplifiers in transmission systems

Another type of optical amplifier is the Raman fiber amplifier (RFA) basing on non-linear effects in transmission fiber. Its molecular vibrational level system is shown in figure 1.3 together with the Raman gain coefficient in the SiO_2 fiber.
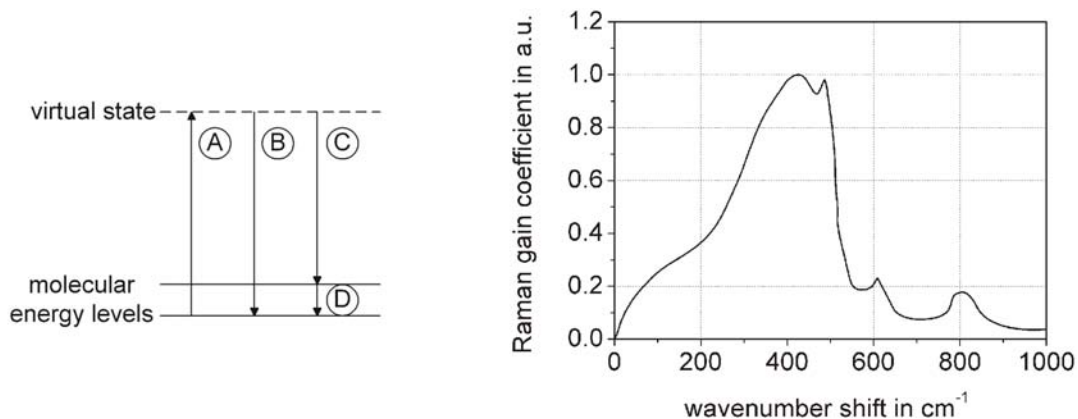
Figure 1.3: Energy diagram of RDFa and Raman gain coefficient of the SiO_2 fiber

Although the setup of Raman amplifier, which consists of high power pump diode, WDM coupler, and the transmission fiber is very simple, its operation principle is more complicated [15]. During the optical pumping process pump photon energy is absorbed into the short-lived virtual excited state (transition labelled as "A" in figure 1.3). Due to the relaxation of the molecule a photon at the same wavelength as the pumping photon is emitted (B). This dominating process is called Rayleigh scattering and acts as a source for optical losses. There

is, however, a small probability, that the photon with lower energy (longer wavelength) is emitted due to spontaneous Raman scattering. The difference (D) between the pump photon and the spontaneous emission does not depend on the pump wavelength and is known as Raman shift. For SiO_2 fibers its spectrum shows a maximum at about $450\,cm^{-1}$ [16] what corresponds to a difference of about $100\,nm$ between the pump and the signal wavelength. If sufficient pump power is coupled into the fiber, the population inversion between virtual state and the final state reaches the threshold value. This causes amplification of signal due to stimulated Raman scattering (C). Since the Raman gain coefficient for typical SiO_2 fiber is very low, the length of the fiber required to achieve high gain is very long (several kilometers). The Raman gain coefficient is a material property and it can be improved by applying high germanium doped silica fibers [15]. But due to the large dimensions those amplifiers (discrete RFAs) are not very convenient for optical transmission systems.

Another group of RFAs (distributed RFAs) gained big interest in the last time. They consist of counter-directionally pumped transmission fiber and they are of great importance for high capacity optical systems. An upgrade of actual transmission systems from $10\,Gbit/s$ to $40\,Gbit/s$ has a large influence on their power budget, since it causes reduction of the individual data channel power of factor 4 and degradation of signal-to-noise-ratio. The decrease of the power can not be compensated by higher output power of the preceding repeater because the total input power is limited to $500\,mW$ for safety reason. Nevertheless, this unfavorable situation can be improved assuring amplification of the optical data stream along the transmission fiber.

Since the gain spectrum can be modified by varying the pump wavelength, the RFAs are wavelength independent. This feature makes possible to construct broadband Raman amplifiers, pumped with several high-power laser diodes [17] or using second order pump wavelength [18, 19]. The highest amplification bandwidth of more than $130\,nm$ was reported for amplifier using interleaving allocation of pump and signal wavelengths [20].

Several experiments with amplifying of $40\,GBit/s$ optical signals using Raman amplifier were reported [18, 21, 22]. The extremely inefficient energy transfer process in RFAs can be improved by applying the pump source with the wavelength corresponding to the second order Raman shift. The signal power improvement comparing to the conventional bi-directional pumping scheme was $5\,dB$ and the total pump power was less than $600\,mW$ for approx. $80\,km$ of the self-developed dispersion modified fiber.

The RFAs are commonly used to amplify signals together with the C- and/or L-band EDFAs [9, 23, 24]. As an example, an RFA was used together with the L-band EDFA to enhance the gain of the transmission system [24]. In the experiment forty $0.8\,nm$ spaced channels located in the wavelength region from 1571 to $1604\,nm$ were amplified using almost $1\,W$ of the total pump power. The gain reported for $-2\,dBm$ of the total signal power was

higher than 16 dB, which is up to 6 dB more comparing to the setup with L-band EDFA only.

1.3 Applications of the rare-earth doped fiber amplifiers

The rare-earth doped fiber amplifiers offer an alternative for SOAs and Raman amplifiers because of their good performance. Therefore they are widely used in optical communication systems. Since thulium-doped fiber amplifier is the subject of this work, in this chapter only the basics of rare-earth doped fiber amplifiers operation will be given. The detailed description along with the physical background will be considered in chapter 2.

The simple operation setup and the rare-earth ion energy level diagram are shown in figure 1.4.
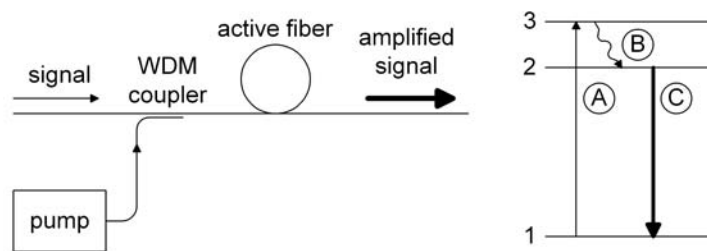
Figure 1.4: Simple setup of the rare-earth doped fiber amplifier and the 3-level energy diagram

The most important part of the amplifier setup is the fiber doped with one of the rare-earth elements like neodymium, praseodymium, erbium or thulium. Since different rare-earths are used as active dopants, the gain spectrum and the pumping wavelengths depend on the emission and absorption properties of the dopant. In general, any of the dopant emission lines can be used to design a fiber amplifier, but since we are interested in the optical telecommunication systems we will concentrate on the amplifiers operating in the infrared region 1200 - 1700 nm).

The wavelength dependent coupler (WDM) in the setup of the amplifier is used to couple signal and pump radiation, which are guided through the optically active fiber. The operational principle of the amplifier can be explained based on the energy level diagram of the rare-earth ion. The amplification process can occur only when the population inversion between the energy levels involved in the amplification process (levels 1 and 2 in the figure 1.4) is achieved. Due to the pump absorption ("A" in the figure) the rare-earth ions are excited into the higher lying energy levels. Due to the short lifetime of the level 3, the ions change their energy state non-radiatively (B) and relax into the lower lying metastable level 2. This level is the upper amplification level and is characterized by the long lifetime. As next, the

transition into ground level occurs due to stimulated emission leading to photon emission (C). The emitted photon is identical with the incoming signal photon. The relaxation process can occur also spontaneously. Both, stimulated and spontaneous emissions are amplified along the active fiber. The first causes signal amplification, and the other which is known as amplified spontaneous emission (ASE) propagates in each direction and acts as a noise.

Different rare-earth amplifiers found the applications in optical telecommunication systems, but the most popular are the erbium-doped fiber amplifiers characterized by their excellent performance. In the meantime they became a key device for the transparent optical networks and therefore the state-of-the-art for the rare-earth doped fiber amplifiers in C-, L- and S- band is given in following sections.

1.3.1   EDFA for C-band applications

The first reported amplifier working in C-band was realized by the research group in Southampton [25] in 1987. Using Ar^{3+}-pumped DCM-dye lased operating at 650 nm apart of flash lamp used as pump source in previous amplifier setups, it was possible to achieve a gain of over 20 dB around 1550 nm. The setup used in the experiments employed low-loss high numerical aperture erbium doped fiber, which maintained effective using of the pump power due to the high pump power density.

The significant improvement in the fiber amplifier technique was achieved in next years, after the high power laser diodes at 1480 nm [26] or 980 nm [27] were realized. They allowed to avoid inefficient pumping at 800 nm, which suffered from significant excited state absorption starting from the upper amplification level [28] and realize efficient all-fiber EDFA setup, which was a milestone towards the robust, compact and portable amplifier setup for the optical transmission systems.

Already the first transmission experiments with EDFAs showed no cross-talk between transmitted channels [29] and the NTT reported the first long-haul transmission over 212 km fiber using 2 EDFAs as power booster and pre-amplifier [30]. This experiment caused strong competition on the optical communication market and the most important players were British Telecom Research Laboratory, KDD R&D Labs, Bell Labs, Fujitsu, NTT and Alcatel. Since 1989 a drastic increase in the capacity of the long-haul optical links consisting of C-band EDFAs was observed. As an example, the transmission over 2223 km employing 25 EDFAs was reported in [31] and the bitrates up to 11 Gbit/s for single channel [32], or up to total 400 Gbit/s in multi channel systems using only C-band EDFAs were demonstrated [33].

Since the WDM transmission over the fiber link consisting of the C-band EDFA was successfully demonstrated, a lot of effort was made to enhance the transmission bandwidth of the flat gain in the amplifier, which is limited to about 30 nm in common EDFAs. Several approaches like new glass types and compositions [34, 35] or using dual-core erbium-doped

fibers [36] was investigated to enhance the amplification bandwidth and/or flatten the amplification curve. Already in 1990 it was found that the amplification beyond C-band can be achieved relatively easy using gain-shifted erbium-doped fiber amplifiers (GS-EDFAs) [37].

1.3.2   GS-EDFA for L-band applications

The main difference of EDFAs optimized for the L-band compared to C-band EDFAs is their low mean population inversion (approx. 0.3 compared to 0.7 in C-band EDFA). It describes the percentage of the excited erbium ions and depends on the position along the fiber. At the beginning of the fiber it achieves the highest value and decreases along the fiber and its mean value depends on the length of the fiber and the pump power.

The optical amplifier gain characteristic is the superposition of the absorption and emission spectra. For small population inversion (as it is the case of L-band amplifier) the gain spectrum in C-band is determined by the high absorption whereas in L-band some positive gain can be expected, due to reusing C-band amplified spontaneous emission to pump the erbium-doped fiber. But since the gain coefficient is very low, significantly longer or highly doped fibers have to be used in GS-EDFAs to achieve signal gain above 20 dB.

There are very few publications describing WDM transition realized with L-band EDFAs only. In [38] a transmission experiment with 64 channels, each with the capacity of 10 Gbit/s was reported. The total length of the fiber span was almost 11 km and a flat gain spectrum was achieved for the wavelengths from 1573 to 1600 nm. In many experiments GS-EDFAs are used simultaneously to Raman amplifier [39] or C-band EDFAs [40] enlarging significantly the optical transmission bandwidth and thus the total capacity of the WDM system.

The amplification in L-band was demonstrated also for non-silica based EDFAs. The gain of 30 dB was achieved for the fluoride based L-band EDFA [41]. On the other hand applying the antimony silicate fibers promises the extension of operation bandwidth up to 1620 nm with the gain larger than 17 dB, as it was reported in [42].

1.3.3   Fiber amplifiers for S- and S$^+$-band applications

Since the amplification using erbium-doped fibers is typical for C- and L-band, the fiber amplifiers doped with thulium have to be applied to amplify signals with the wavelengths shorter than 1520 nm. Nevertheless, the S-band EDFA supporting more than 20 dB gain in the wavelength region of 1480 to 1530 nm was successfully demonstrated in [43]. Due to the very high absorption and weak erbium emission for the wavelengths below 1530 nm very high attenuation at the wavelength for which the EDFA reaches its gain maximum (approx. 1530 nm) has to be introduced to achieve the significant gain in S-band. This was achieved by applying specially designed refractive index profile of the fiber, which caused blocking propagation of the wavelengths longer than 1530 nm. The amplifier based on such a fiber reaches more than

20 dB gain and its noise figure is less than 8 dB for the total pump power of 250 mW at 980 nm.

Since the previous method requires special silica fiber, the amplification in the S- and S$^+$-band can be achieved more convenient by employing the fibers doped with the thulium ions. Several types of hosts like silica [44] or tellurite [45] based glasses were use for the experiments, but the most promising seem to be fluoride based glasses. They are characterized by the low phonon energy (see chapter 2.2) and therefore the properties of thulium can be used much more effectively in the fluoride glasses compared to other glass types.

Nevertheless, the highest gain of thulium-doped **silica** fiber amplifier was reported to be 13 dB at 1515 nm for almost 2 W of the total pump power at 1047 and 1410 nm [44]. Additionally, the TDF was cooled down to 77 K, which is inapplicable for most applications.

The TDFAs based on **tellurite** glass exhibit much higher and broader amplification than the silica based amplifiers, but their disadvantages are high refractive index ($n \sim 2$) and relatively high phonon energy. The high refractive index causes significant reflections on the interface to the silica fiber. The highest reported gain of 26 dB was achieved for double-wavelength pump configuration (800+1064 nm) and the noise figure was less than 4 dB [45].

Most research activities concerning TDFA focus on **fluoride** based fibers as a host for the amplifier. The fluoride and silica fibers can not be thermally spliced due to their different thermal properties (see chapter 5.3.1) but their refractive index does not differ much from that of silica fibers, which makes the connection technique not so critical as in case of tellurite fibers. Nevertheless, a stable and reliable connection method is one of the key issue for TDFA (see chapter 5).

The first S-band thulium-doped fiber amplifier was constructed by NTT in 1993 [46]. Except of NTT also NEC, Alcatel and temporarily British Telecom [47] and Nortel Networks [48] exhibited some activities in the amplifier development and optimization. Since the fibers used in optical telecommunication systems suffer from the OH-absorption peak at about 1400 nm the natural amplification bandwidth of TDFA has to be shifted towards the longer wavelengths. The first gain-shifted TDFA was realized in 1999 by NEC [8]. The gain and noise figure for 1047+1560 nm pumping configuration were 30 dB and 5 dB, respectively.

In the next years different pumping configurations supporting even lower noise figure and even higher power conversion efficiencies (PCE) were reported. The highest reported PCE was larger than 50 % and it was achieved by the Alcatel group for the dual wavelength pump configuration 790+1400 nm [49]. Apart from the attempts to maximize the pumping efficiency, big effort was applied to develop high-gain and low-loss gain-shifted amplifiers working in the S-band. The gain-shift effect was achieved mostly by careful choice of the pump wavelength and power management [8], but also due to high dopant concentration [50].

Like in the case of L-band EDFAs, transmission systems based purely on the TDFAs were not yet investigated. The reason of it is the fact, that these amplifiers were developed as

an upgrade for EDFA-based systems and their performance was investigated only in setups consisting of C- and L-band EDFAs [10] or Raman amplifiers [51].

1.4   Optical amplifiers - comparison

Beside SOAs and RFAs, fluoride based TDFAs are an alternative for the amplifiers for wavelengths beyond C- and L-band. In table 1.1 important parameters of these three types of amplifiers are collected. We concentrate only on the amplifiers for the S- and S$^+$-band.

Table 1.1: Performance comparison of amplifiers for for S- and S$^+$-band

feature	SOA	RFA	TDFA
small signal gain in dB	>30	>40	>25
noise figure in dB	~5	>4[a]	<4
gain bandwidth in nm	30-50	>20[b]	up to 50[c]
output signal power in dBm	>20	>30	>20
coupling loss in dB	3-5	<0.1	<1
power conversion efficiency	good	poor	moderate

Notes:
[a] dependent on the pump direction,
[b] for the amplifier pumped with a single pump, for many pumps - up to 137 nm [52],
[c] both S- and S$^+$-band

Due to the large gain bandwidth and low noise figure, TDFA is a good candidate for optical communication systems. Compared to Raman fiber amplifiers only few meters of active fiber and a pump power in the order of some hundreds of miliwatts is needed to achieve more than 25 dB gain. For the comparable gain achieved by RFA one needs typically about 1 W of the pump power and several kilometers of the transmission fiber. The long length of the fiber causes problems with the dispersion management, which is not the case in thulium-doped fiber amplifiers with the typical active fiber length of several meters. The advantage of TDFA comparing to SOAs is the fact, that the former is the all-fiber device, which makes possible to achieve the low-loss connections to other parts in the transmission system setup while the fiber-SOA connection losses are much larger than in RFAs or even TDFAs.

In fact, this comparison shows that all three groups can find the applications in the optical transmission systems. The semiconductor amplifiers will win in most low-end solutions, where the cost of the device is the decisive application criterium. The TDFAs and Raman amplifiers will find their applications in more complex WDM transmission systems, however the RFAs based flat gain systems seem to be sensitive on the failure of the pump laser [53]. The biggest

problem of TDFAs is the reliable fiber connection technique, which becomes significant for high pump and/or signal powers.

In the next chapters we will concentrate on issues important for designing efficient fluoride based thulium-doped fiber amplifier. But before we concentrate on the thulium spectroscopy let us have first focus on the operation principles and specialities of this kind of fiber amplifier.

2 Thulium-doped fiber amplifier - operation principles

The rare-earth doped fiber amplifier is one of the key devices in optical telecommunication systems. It allows to amplify simultaneously many optical signals without their conversion into electrical domain. The most popular rare-earth doped fiber amplifier is EDFA, which due to the continuous development and enhancement of its performance found applications in the optical communication systems.

Erbium- and thulium-doped fiber amplifiers differ in many aspects of the operation principles. Their parameters are determined by the rare-earth dopant ion, but the energy structure of both elements is different, especially the lifetimes of the levels which are involved in the amplification process. In the next chapters the operation principle of TDFA will be discussed and its special issues will be compared with the well-established EDFA.

2.1 Energy levels of thulium

The performance of any rare-earth doped fiber amplifier is determined by the dopant properties and its interactions with the host glass. Therefore the fiber amplifier analysis requires the understanding of both of these aspects. The best starting point for that analysis is the energy level diagram of triply ionized thulium ion, which is shown in figure 2.1.

The allowed energy states of a thulium ion can be represent as 13 energy levels, however only a few of them are directly involved in the amplification process. The arrows in the figure corresponds to two processes, which are indispensable for designing of any fiber amplifier. They can be divided into two groups: **absorptions** (from the ground or any of the excited levels) and **emissions**. The absorption is used to optically pump the amplification medium, result of which is to supply the energy needed to change the thulium ion's energy state. The absorption of the pump radiation leads to the **population inversion**, which is necessary to observe the signal amplification.

Theoretically, one can employ any of the absorption lines shown in the energy level diagram to form the population inversion, but the additional parameter in form of the **lifetime** of the energy level has to be taken into account. The lifetimes shown in figure 2.1 are typical literature values and they correspond to the host-independent radiative lifetimes of thulium ions. Typical for thulium is its long lifetime of the lower amplification level, which is about 10 ms. Comparing to about 1.3 ms for $^3F_4$ level it is clear that the population inversion can not be achieved with single pump because of the bottleneck effect caused by the long lifetime of the $^3F_4$ level. Pumping with 800 nm laser source the ions are excited shortly into the upper amplification level, but then they relax into the $^3F_4$ level, where they stay for a longer time.
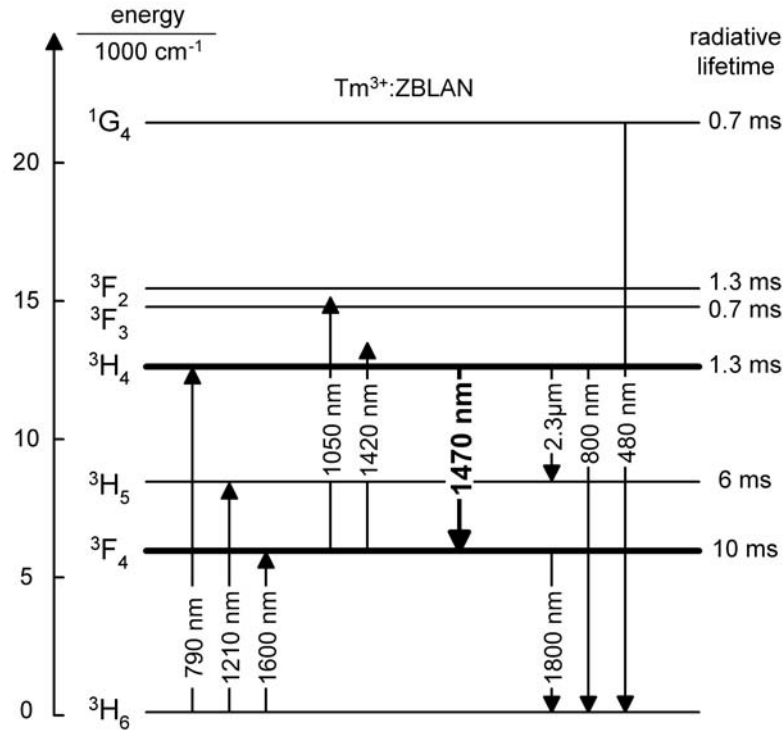
Figure 2.1: Energy level diagram of Tm^{3+} : ZBLAN

As a result, the large part of the ions occupy the lower amplification level and only some of them stay in the excited state $^3H_4$. Therefore the auxiliary pump corresponding to the excited state absorption centered at 1050 or 1420 nm has to be used to effectively excite the thulium ions and form the population inversion.

There are several emission lines starting from one of the excited states. Due to the different population of the higher lying levels they strengths differs. Also the emissions starting from the same level differ in efficiency. For TDFA the amplifier transition occurs between $^3H_4$ and $^3F_4$ level and it is centered at approx. 1470 nm. Nevertheless the strength of the competitive emission lines $^3H_4 \rightarrow ^3H_5$ or $^3H_4 \rightarrow ^3H_6$ limits its efficiency. The efficiency of the fluorescence corresponding to the emission is also influenced by the glass matrix, which in the case of TDFA is much more critical than in EDFA. The glass composition and its properties can cause the broadening of the gain spectra (like in telluride or fluoride based EDFAs) and due to the **phonon energy** has an influence of the amplifier's performance, which is particularly critical in TDFA. The non-radiative transitions in the amplifier's host glasses are very critical and therefore they are discussed in details in the next section.

2.2   Low phonon energy glasses

To understand the differences between glass compositions we start with the most common SiO_2 glass matrix. It consists of silica and oxygen atoms with 1:2 atomic ratio. The structure of the glass depends on on the spatial arrangement of the Si^{4+} and O^{2-} ions which is affected by the size of the ions [54]. Due to the radius ratio of the silicon and oxygen ions, which is 0.3, the glass matrix consists of $[SiO_4]$ tetrahedrons, where each oxygen belongs to two silicon atoms. The bonds between the atoms forming the glass structure are combination of covalent, ionic and double bond, which are present in the same fraction. The tetrahedrons are joined to each other with vertices and form the spatial structure shown in figure 2.2.
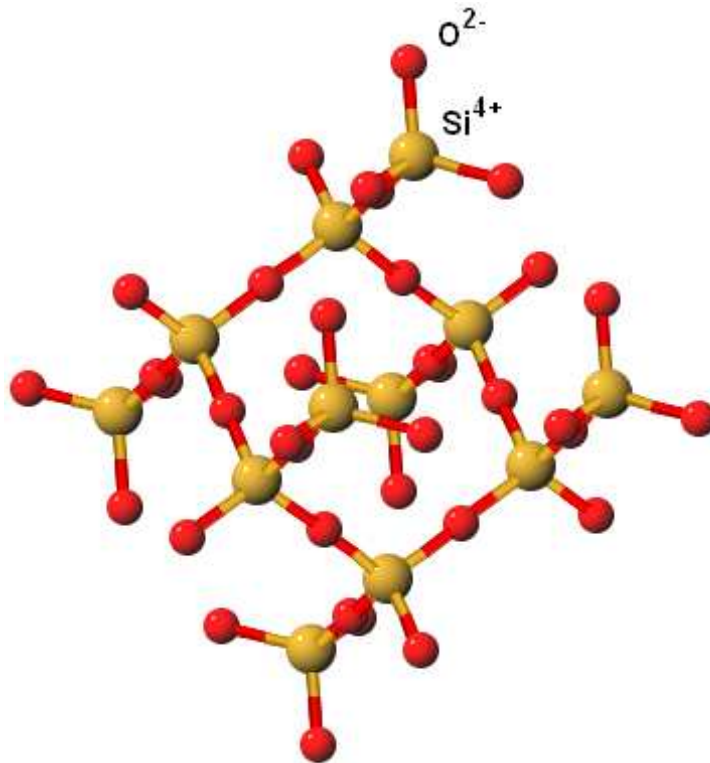
Figure 2.2: 3D lattice structure of SiO_2 crystal [55]

This structure is characterized by its small ions, which are located relatively far from each other. The distance between the neighboring oxygen ions is approx. $0.163\,\text{nm}$ and $0.35\,\text{nm}$ between two silicon ions [54]. This means that the glass structure is "sparse" and the space between the atoms can be filled with additional elements (e.g. rare-earth ions) modifying properties of the glass. The long and strong bonds between the atoms lead to strong thermally caused vibrations in the glass matrix. The energy of these vibrations is quantized and

its smallest part is called **phonon**. The value of the phonon energy in SiO_2 glasses is large and reaches $1050\,\mathrm{cm^{-1}}$.

The phonon energy can be drastically reduced by using so called low phonon energy glasses. This name applies to all glasses with the phonon energies lower than that of pure silica. Some of these glasses are collected in table 2.1. Since the phonon energy influences also the glass transmission, the LPE glasses are characterized by the significant shift of their transparency towards infrared (IR). The IR absorption edge is also given in the table 2.1. For the comparison the parameters of the SiO_2 glass are also given.

Table 2.1: SiO_2 and some LPE glasses with their phonon energies and IR absorption edge measured for the glass sample [56]

glass	phonon energy in cm^{-1}	IR abs. edge in μm
SiO_2	1050	2.5
GN^a	850	-
$GPBZK^b$	820	5.3
TB^c	610	-
$ZBLAN^d$	580	~7
$IBZP^e$	~510	~7
BIG^f	~450	7.5
$CNBK^g$	370	~10
CdX^h	236	~10
GLS^i	425	~10

Glass composition:
[a] $90GeO_2 - 10Na_2O$,
[b] $55GeO_2 - 20PbO - 10BaO - 10ZnO - 5K_2O$,
[c] $80TeO_2 - 20BaO$,
[d] $53ZrF_4 - 20BaF_2 - 3.875LaF_3 - 3AlF_3 - 20NaF - 0.125InF_3$,
[e] $28InF_3 - 18BaF_2 - 20ZnF_2 - 4SrF_2 - 6PbF_2 - 5YF_3 - 7AlF_3 - 2LiF - 10NaF$,
[f] $20BaF_2 - 18InF_3 - 12GaF_3 - 20ZnF_2 - 10YbF_2 - 6ThF_4 - 4ZrF_4$,
[g] $33CdCl_2 - 17CdF_2 - 34NaF - 13BaF_2 - 3KF$,
[h] $CdX_2 - BaX_2 - NaX$ with high Cl-ratio,
[i] $70Ga_2S_3 - 30La_2S_3$

As expected, the highest phonon energy among the presented glasses was measured for pure SiO_2 glass. Nevertheless, it is also possible to achieve LPE oxide glasses by increasing the atomic mass of the oxides forming the glass matrix. In this way germanium or tellurite glasses were developed with the phonon energy 40 % smaller than for the pure SiO_2 [56]. Due to the low phonon energy, the tellurite glasses are one of the most interesting oxide glasses for amplifier and laser application.

Another family of LPE glasses are zirconium-fluoride based glasses, with its most popular type ZBLAN. Since the phonon energy depends on the bond strength, the fluoride glasses show worse mechanical, thermal, and chemical stability comparing to SiO_2. But the refractive index similar to silica glasses and relatively well-developed manufacturing procedure together with the optical transparency up to more than $7\,\mu m$ make them ideal candidates for the fiber amplifier and/or laser. The structure of ZBLAN is more complex than that of SiO_2 and therefore difficult to present. Schematic representation of the fluoride glass is shown in figure 2.3.
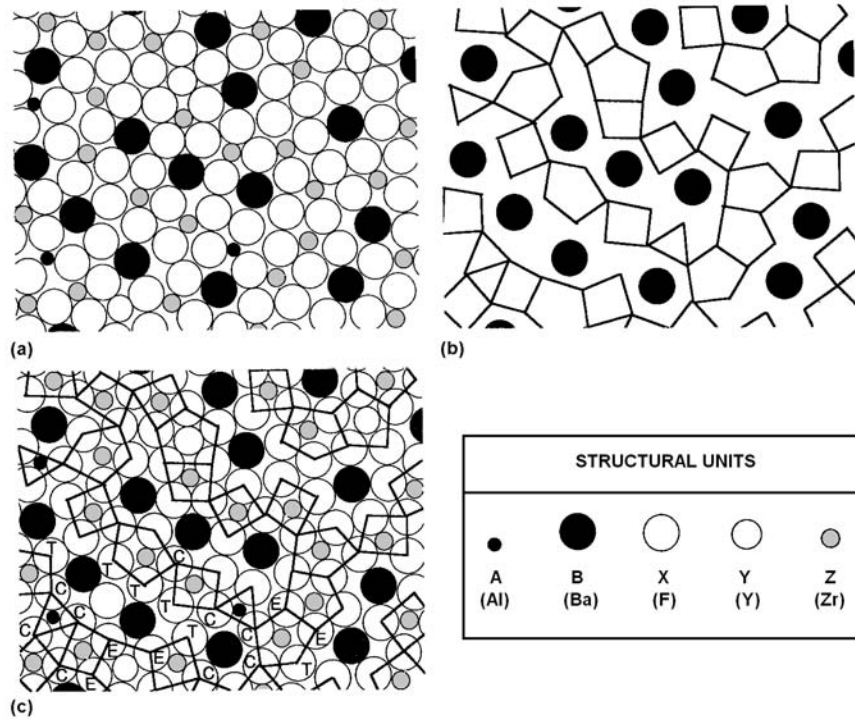
Figure 2.3: Schematic representation of a fluoride glass: (a) random close-packed model, (b) network model, (c) relation between (a) and (b) [57].

There are two main models of complex glass matrices and their detailed description is given in [57]. According to the random close-packed model, the bond lengths in ZBLAN glasses are about $0.21\,nm$ for $Zr - F$ and $0.26\,nm$ for $Ba - F$ connection, which is less than in silica glass. Also the glass spatial structure is different from that of SiO_2. The coordination number, defined as the number of binds, for main components is constant and lies between 7 and 8 for zirconium and 10 for barium ions. Aluminium fits octahedral sides while lanthanide ions are expect to have the coordination numbers between 8 and 9. The coordination number

of fluoride is close to 10.

From the network glass model some conclusions can be gained according to the bonds between zirconium fluoride polyhedra and the effect of the fluoride chain formation. Nevertheless, it can be seen that the structure of ZBLAN glass is much more "dense" than that of SiO_2 and the bonds are ionic. Also the ions forming the glass matrix exhibit bigger ionic radii (e.g. approx. $0.13\,\mu$m for fluor or $0.152\,\mu$m for barium) comparing to silica ($0.026\,\mu$m). This result in lowering the phonon energy and the red shift of the IR transparency edge, as it was already mentioned.

Beside of the oxide and fluoride based glasses also some halide and indium based glass compositions with low phonon energy were developed. They are more difficult to handle and some of them (for example CdX) show bad transmission properties. This makes them inapplicable in praxis despite their very low phonon energy. Due to the high chloride ratio the CdX fibers are even less stable and more hygroscopic than ZBLAN.

The chalcone based glasses are the youngest LPE glass family. Also this glasses are characterized by their low mechanical and thermal stability and due to the fact that these glasses are relatively young their practical applications in the fiber amplifier or lasers were not yet reported.

The advantages of the LPE glasses can be now summarized in several points [56].

- non-radiative, multiphonon transitions from the neighboring levels are expected to be decreased, because more than one phonon will be needed to bridge the difference in the energy states,

- lifetimes of the excited levels in LPE glasses are longer than in SiO_2. There are more metastable levels and one can expect higher quantum efficiency. Also the emission lines are expected to be broader,

- the absorptions from the excited states are more efficient due to the longer lifetime. This can be used for optimal optical pumping (like in the case of Tm^{3+} : ZBLAN fiber amplifier).

This makes the LPE glasses, and particularly ZBLAN, very useful for up-conversion fiber lasers. Due to the high efficiency of the thulium and praseodymium fluorescence in fluoride glasses they are ideal host for the fiber amplifiers and therewith interesting for this work.

2.3   Amplification process in TDFA

Differently than in EDFA, which is simple three-level atomic system, thulium doped fiber amplifier works in principle as a multi-level system. For comparison, energy levels for thulium

and erbium are shown in figure 2.4.
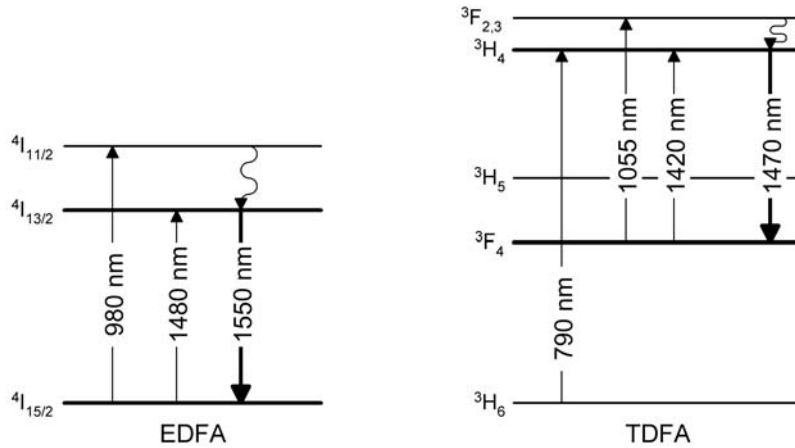
Figure 2.4: Comparison between energy levels of the EDFA and TDFA

In the three-level system, to obtain population inversion at least half the population of atoms have to be excited from the ground state $^4I_{15/2}$ effectively to the metastable $^4I_{13/3}$ level via $^4I_{11/3}$ level, which is characterized by short lifetime. It requires very strong pumping of the laser medium and makes such a system inefficient.

The unambiguous classification of TDFA as three- or four-level system is impossible. When pumping at 790 nm the TDFA shows the properties of a typical four-level amplifier system, which is transparent, when the pump power is not applied. On the other hand the main energy circulation takes place between three excited levels $^3F_4$, $^3H_5$ and $^3H_4$ therefore one speaks about quasi-three-level operation scheme. It assumes, that due to the long lifetime of the $^3F_4$ level and high ground state absorption at 790 nm, corresponding to the $^3H_6 \rightarrow ^3H_4$ transition, the ground $^3H_6$ level is fully depleted. It means, that at that point the ground level plays the minor role in the absorption processes leading to achieving the population inversion. As a result the population inversion can be observed only by employing **two-stage pumping process**. This approach was already realized in the one-color up-conversion pumping scheme employing 1064 nm radiation emitted by the Nd:YAG laser [46]. The non-resonant ground state absorption at the pump wavelength was a limiting factor to achieve high pumping efficiency, nevertheless it was compensated by the high power delivered by the laser. Such an energetically inefficient system was improved by using the pump wavelengths corresponding to the resonant ground- and excited-state absorptions.

The quantitative description of the amplification process requires a brief introduction into the theory describing the interactions between the electro-magnetic field and the matter.

Assuming a two-level energy system, as shown in figure 2.5, one can observe three simultaneously occurring processes. These are already mentioned absorption, and stimulated and spontaneous emission which can be characterized by Einstein coefficients B_{12}, B_{21} and A_{21}.
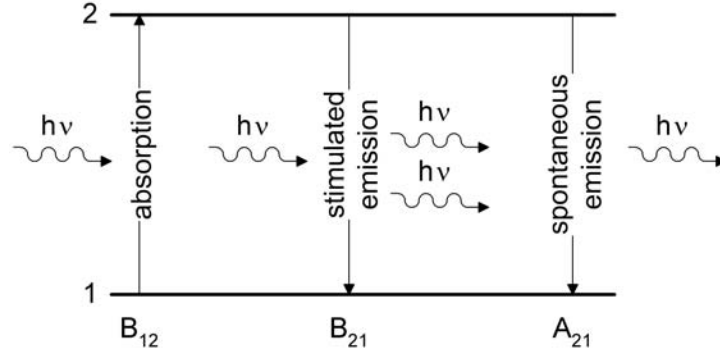
Figure 2.5: Three basic interactions between the electro-magnetic field and the matter

Using these three parameters one can describe the population of both energy levels in the equilibrium state of absorption and emission according following equation:

$$N_1 B_{12} \varrho_\nu = N_2 (B_{21} \varrho_\nu + A_{21}) \ , \tag{2.1}$$

where N_i is the population of the level i (and $\Sigma \, N_i = 1$) and ϱ_ν is the spectral energy density of the radiation field at frequency ν, which is given by the Planck's law:

$$\varrho_\nu d\nu = \frac{8\pi\nu^2 n^3}{c^3} \frac{h\nu}{\exp^{h\nu/k_B T} - 1} d\nu \ . \tag{2.2}$$

The constant c in previous equation is the speed of light in vacuum, n is the refractive index of the host material, k_B is the Boltzmann's constant, and T is the temperature. If the system is in thermal equilibrium state, the relative occupations can be calculated according of the Boltzmann statistics:

$$\frac{N_2}{N_1} = \frac{g_2}{g_1} \exp^{-\frac{h\nu}{k_B T}} \tag{2.3}$$

where g_i is the degeneracy of the ith state. The Einstein coefficients satisfy following conditions:

$$\frac{A_{21}}{B_{21}} = \frac{8\pi\nu^2 n^3}{c^3} \tag{2.4}$$

and

$$\frac{B_{21}}{B_{12}} = \frac{g_1}{g_2} \ . \tag{2.5}$$

Since the energy level diagram of the rare-earth ion is more complex than simple two level systems, the final equations describing the Einstein parameters are more complicated. The advanced analysis, described in details in [58], can be used to obtain important spectroscopic quantities as radiative lifetimes, branching ratios or oscillator strengths.

The absorption and emission processes described for two-level system, in TDFA can generally occur between any energy levels, which has to be taken into account for the modelling of the amplifier as shown in chapter 6.2. The description of the amplifier operation can be now enhanced with the fact that both stimulated and spontaneous emission occurs simultaneously, but they have to be treated in a different way. The stimulated emission is induced by the incoming signal photon and leads to emission of second, coherent photon and finally to the signal **gain**. The spontaneous emission leads to emission of the broadband, low-power, stochastic radiation, which amplified along the active fiber acts as a **noise** source. Both, the gain and noise figure are two of the basic TDFA parameters and they will be described in next sections.

2.4   Basic parameters of the TDFA

The rare-earth doped fiber amplifiers found many applications in optical transmission systems. The most important are shown in figure 2.6.
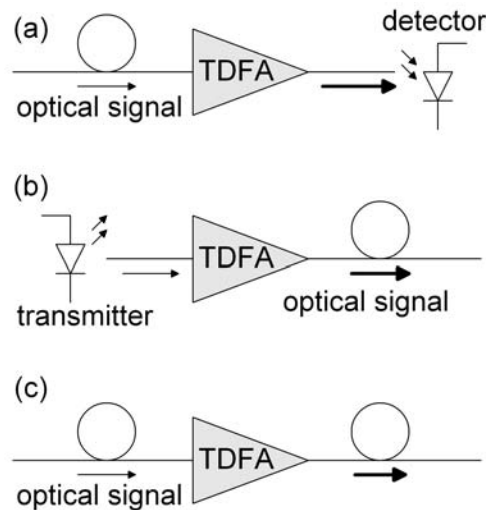
Figure 2.6: Applications of the optical fiber amplifiers, (a) preamplifier, (b) power booster, (c) optical repeater

Since the most simple optical transmission system consists of transmitter, receiver, and fiber link connecting both of them, there are generally three possible scenarios, which employ

TDFAs. In the first case the amplifier is placed just before the end terminator of the optical line (detector) and operates as a **preamplifier**, which increases the sensitivity of the detector. Signal amplification performed just in front of the receiver results in boosting the weak optical signal and accompanying noise above the thermal noise of the detector.

Another application for the amplifier is the **power booster** used just behind the signal source (or the signal multiplexer in wavelength division multiplexing (WDM) systems). Such an amplifier is used to increase the transmitted signal power and therefore allow the optical transmission over long distances, which is critical for submarines telecommunication systems.

Due to the fact, that the distance between the signal regenerators in the transmission systems depends mostly on the signal losses in the fiber, it is not required to completely re-generate the signal in every amplifier. It is a common solution, that the signals are amplified (*re-transmitted*) using the in-line amplifier called also **optical repeaters**, while *re-shaping* the signal is realized by the dispersion modified fibers. The *re-timing*, which is essential in high bitrates systems, is realized electronically or optically as described in [59].

The requirements for the fiber amplifier depends on its operating point. In next sections we will focus on such important parameters of the TDFA as gain, noise figure and power conversion efficiency.

2.4.1   Signal gain

One of the basic parameters of any amplifier is the signal **gain**, which is defined as the difference between the signal output power and the signal input power. According to the International Electrotechnical Commission (IEC) its quantitative description is given by:

$$G^{dB} = 10 \log \frac{P_{out} - P_{ASE}}{P_{in}} \, , \tag{2.6}$$

where P_{out} is the output optical power, P_{in} is the input optical power and P_{ASE} is the power of the amplified spontaneous emission (ASE) as it was shown in figure 2.7.

Since the optical spectrum at the output of the amplifier includes also broadband ASE, which acts as a noise, it is necessary to estimate its value as it is necessary for using equation (2.6). The ASE level at the signal wavelength can not be measured directly but it has to be interpolated by measuring the noise level at two wavelengths to the right and to the left of the signal wavelength as it was shown in figure 2.7. The TDFA analysis can be performed automatically by the optical spectrum analyzer, but the special care has to be taken during the estimation of the ASE level. The amplified spontaneous emission is fitted with a gaussian curve, which can lead to some discrepancies in the wavelength regions, where ASE is very weak (beginning and end of the gain spectrum).
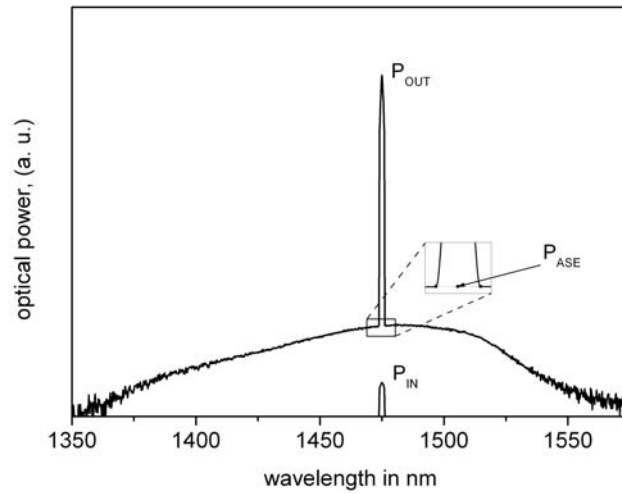
Figure 2.7: A method to estimate the individual power levels for P_{in}, P_{out} and P_{ASE}

According to applications of the fiber amplifiers, different gain characteristics are expected. Since the optical repeater and pre-amplifiers operate on very weak optical signals, their small-signal gain has to be large, however their performance for high input power is not so important. On the other hand, the amplifier operating as the power booster works in the saturation regime and it is more appropriate to characterize it by the signal output power.

It is obvious that the working point of the amplifier determines its design. Different performance can be observed when changing the pumping scheme and direction, but for the optimum length of the active fiber high gain and low noise figure can be expected when the co-directional pumping scheme is applied. The backward pumping leads to high population inversion close to the receiver end of the amplifier, where the signal is weak and the signal to noise ratio is poor. As a result, high output power can be expected, but accompanied by higher noise figure. Therefore the co-directional pumping is used in the in-line amplifiers and power amplifiers while backward pumping is more suitable for the preamplifiers or the appropriate stages in multi-stage amplifiers.

The amplifier's gain and its shape depend strongly on the length of the rare-earth doped fiber. In a too short fiber the pump power is not fully absorbed and therefore the pumping process not efficient. In the case of long fibers the pump power is fully absorbed, but the unpumped part of fiber acts as an attenuator leading to decrease in the gain. Nevertheless, long thulium-doped fibers are used in the S-band and the process employed there is called **gain shift**. In the long fiber only the first part is inverted while the rest absorbs the amplified

signal and uses the generated ASE. This result with the decreasing of the inversion parameter defined as:

$$D = \frac{N_{upp} - N_{low}}{\sum N_i} \; , \tag{2.7}$$

where N_{upp} and N_{low} are the population of the upper and the lower amplification level, respectively and N_i is the population of the ith level. According to this equation, for the fully inverted TDF $D = 1$ and $D = -1$ is to expect when the active fiber is not pumped. In the gain-shifted fiber amplifiers the inversion parameter is kept low, therefore long fiber is needed to achieve significant gain.

The dopant concentration and numerical aperture of the thulium-doped fiber play an important role for the efficient exchange of the pump power into the signal power. The rare-earth doped fibers belong mostly to the family of the high numerical aperture (HNA) fibers. Due to the small core (diameter typically 2 to $3\,\mu$m) and large numerical aperture ($>$0.2) the pump power propagates in the limited region close to the fiber axis leading to high power density. The pumping efficiency can be increased, when the dopant ions are concentrated in the small space around the fiber axis with concentration preventing lifetime quenching. Unfortunately, this leads to increase in the optimal fiber length needed to achieve maximum gain.

As discussed above, there are many parameters which have an influence on the gain of the amplifier. These cited here are the most obvious and can be easily optimized to fit the amplifier design requirements.

2.4.2 Noise figure and its management in the optical fiber amplifier

The noise properties are the second basic group of parameters characterizing the optical fiber amplifiers. Particularly in the long haul transmission systems and undersea optical links noise of the amplifier defines the maximum distance between the repeaters and finally the total length of the transmission line. In every amplifier the signal and spontaneous emission are amplified along the fiber. As a result, on the output the amplified signal overlaps with the amplified spontaneous emission causing deterioration in the signal to noise ratio. This process occurs in every amplifier and therefore the small noise figure is one of the key parameters of the in-line amplifier.

The major noise source is the ASE present in the amplification spectrum with the noise density proportional to the gain [60]. The detected optical signal leaving the amplifier consists therefore the amplified signal and noise caused by amplified spontaneous emission. Since the detection is a non linear process the detected intensity I is proportional to the squared total electrical field and is given by:

$$I \propto (\overrightarrow{E_{sig}} + \overrightarrow{E_{sp}})^2 = \frac{e}{h\nu}\left(E_{sig}^2 + E_{sp}^2 + E_{sig}E_{sp}^* + E_{sig}^*E_{sp}\right) \; , \tag{2.8}$$

where * denotes the complex conjugate. The first term (E_{sig}^2) corresponds to the amplified signal. All others describe noise and they can be interpreted as follows:

- E_{sp}^2 represents the product of the spontaneous emission field with itself and therefore is called *spontaneous-spontaneous* beat noise term,

- $E_{sig}E_{sp}^* + E_{sig}^*E_{sp}$ denotes the noise beat between the signal and the spontaneous emission.

As result, the receiver detects not only usable signal but also harmonics caused by the noise beat. Fortunately, some of the parasitic harmonics occur for the frequencies aside of the detector bandwidth.

The total amplifier noise N_{tot} consists of five components and is described as:

$$N_{tot} = N_{shot} + N_{sig\text{-}sp} + N_{sp\text{-}sp} + N_{th} + N_{mpi} \ , \tag{2.9}$$

where N_{shot} is the mutual signal and spontaneous emission shot noise, $N_{sig\text{-}sp}$ is the beat noise between the signal and the spontaneous emission, $N_{sp\text{-}sp}$ is the beat noise of the spontaneous emission, N_{th} is the thermal noise of the receiver and N_{mpi} is the multi-path interference noise [60]. The last noise component is caused by the reflections due to the optical inhomogeneity of the transmission line, which can be formed inside of the amplifier setup or out of it [61, 62]. These reflections can be successfully suppressed by using optical isolators. According to [60], the individual noise terms can be formalized as:

$$N_{shot} = 2B_e(GI_s + I_{sp})eB_o \ , \tag{2.10}$$

$$N_{sig\text{-}sp} = 2GI_sI_{sp}\frac{B_e}{B_o} \ , \tag{2.11}$$

$$N_{sp\text{-}sp} = \frac{1}{2}I_{sp}^2\frac{B_e(2B_o - B_e)}{B_o^2} \ , \tag{2.12}$$

$$N_{th} = I_{th}^2 \ , \tag{2.13}$$

The parameters used in equations (2.10) to (2.13) are as follows: B_e is the bandwidth of the electrical filter used in the electrical receiver circuit, B_o the optical bandwidth of the filter present in optical spectrum analyzer, G the amplifier gain, I_s the photocurrent generated by the signal photons, I_{sp} the photocurrent generated by the spontaneous emission, I_{th}^2 the variance of the thermal noise current, and finally e is the elementary electron charge.

Looking closer at the previous equations one can conclude that one of the most significant components of the total noise is the beat noise between the signal and spontaneous emission $N_{sig\text{-}sp}$. Another one is the shot signal and spontaneous emission noise N_{shot}. Both of them

vary with the amplifier gain and can not be eliminated whereas other noise components can be suppressed by using optical or electrical filters with optimized bandwidth.

The parameter which quantifies the noise properties of the rare-earth doped fiber amplifier is the **noise figure** defined as:

$$NF^{dB} = 10 \log \frac{SNR_{in}}{SNR_{out}} \; , \tag{2.14}$$

where SNR_{in} and SNR_{out} are the signal to noise ratio on the input and on the output port of the amplifier, respectively. This ratio becomes worse due to the stochastic interaction between the dopant ion and the pumping photons. Assuming a receiver with an ideal detector characterized by quantum efficiency close to unity and the fact that the noise is determined by $N_{sig\text{-}sp}$ it was shown [60] that for three level systems with significant gain, the noise figure can be approximated by the equation:

$$NF = 2n_{sp}\frac{G-1}{G} \; , \tag{2.15}$$

where n_{sp} is the population inversion factor defined as:

$$n_{sp} = \frac{N_{upp}}{N_{upp} - \frac{\sigma_a(\lambda)}{\sigma_e(\lambda)} N_{low}} \; . \tag{2.16}$$

The parameters σ_a and σ_e in the previous equation denote the absorption and emission cross-sections, N_{upp} and N_{low} are the population of the upper and lower amplification level respectively. The equation leads to the conclusion that in the case of the total population inversion the noise figure approach the quantum noise limit, which is $3\,\mathrm{dB}$.

Noise reduction is one of the key issues of the TDFA. The lowest reported noise figure in TDFA was $3.5\,\mathrm{dB}$ and it was reported for single-color pumping scheme at $1064\,\mathrm{nm}$ [47].

There are several optical, optoelectronic or electric methods used for the noise figure measurements [60, 62]. In the most common optical techniques an optical spectrum analyzer is used to measure the amplified spontaneous emission and the noise figure is calculated as:

$$NF = \frac{1}{G} + \frac{2\rho_{ASE}}{Gh\nu} \; , \tag{2.17}$$

where G is the amplifier's gain, ρ_{ASE} is the spectral density of the amplified spontaneous emission, h is the Planck's constant, and ν is the optical frequency.

The accurate separation of the laser source spontaneous emission (SSE) and amplified spontaneous emission plays an important role in noise figure measurements in the wavelength division multiplexing (WDM) systems. The SSE is very similar to ASE, but it is produced

by the internal optical gain of the laser transmitter. It was shown that $-50\,\text{dBm/nm}$ SSE at the signal wavelength overvalue the noise figure of about $50\,\%$ for the amplifier with the mean ASE level of $-18\,\text{dBm/nm}$ [62].

A number of refinements of the optical method have been developed for accurate noise figure characterization. They include source subtraction, time domain extinction, polarization extinction, reduced source or signal substitution, but since the noise figure measurements reported in this work were performed using optical spectrum analyzer the simple optical measurement method was applied. More advanced noise figure estimation techniques were discussed in details in [62].

In conclusion, the low noise figure is very desirable feature of TDFAs, especially when the transmission line consists of more than one amplifier. Low *NF* is of special importance for the power booster and the optical repeaters, since noise accumulates along the optical link, which worsens the signal-to-noise ratio observed on the receiver end. As consequence the power booster and in-line amplifiers are co-directionally pumped because higher noise figures are expected for backward pumped amplifiers.

2.4.3   Power conversion efficiency and quantum efficiency

The **power conversion efficiency** (*PCE*) is a parameter used to characterize the performance of the amplifier for high signal powers as it is the case in power boosters. This amplifiers employ high power pump diodes, whose lifetime strongly depends on the operation current. Therefore this type of amplifiers have to be designed to deliver high output power for the pump power which is as small as possible. The pump-signal conversion process is easy to quantify as:

$$PCE = \frac{\Delta P_s}{\Delta P_p} = \frac{P_s^{out} - P_s^{in}}{P_p^{in} - P_p^{out}} \, , \tag{2.18}$$

where P_s^{out}, P_s^{in}, P_p^{in} and P_p^{out} are the power of the output and input signal and pump, respectively.

This parameter, similar to gain, can be defined for the complete amplifier setup including the losses caused by every part of the setup (fiber couplers, isolator, etc.) or it can be referred to the rare-earth doped fiber only. In the first case, the input and output values of the pump and signal power are used for the calculation; in the second - the values present at the input and output of the active fiber. The *PCE* calculated according the second definition of input and output conditions is higher than that calculated for the complete amplifier setup.

The pump efficiency can be also expressed as a **quantum efficiency** (*QE*) according to the equation:

$$QE = \frac{\Delta P_s \lambda_s}{\sum_i \Delta P_{pi} \lambda_{pi}} \, , \tag{2.19}$$

where λ_{pi} is the wavelength and P_{pi} the power of the ith pump diode. The physical interpretation of the QE is the growth of the number of signal photons using a number of pumping photons. Both, PCE and QE achieve significant values for high signal powers; for low power the amplified signal is lower than the total ASE power and therefore only small part of the output power comes from the usable signal. By increasing the signal power this ratio changes to signal's benefit. It was reported that the PCE and QE can be improved in the fiber amplifier when high NA rare-earth doped fiber are used [63].

The power conversion efficiency depends strongly on the pump scheme of the thulium-doped fiber amplifier. For the single-color, 1064 nm up-conversion pumping scheme the maximal reported PCE was 17.5 % [47]. Much higher values beyond 50 % were achieved by employing highly efficient double-color pumping scheme using Ti:Saphire radiation at 780 nm and Raman fiber laser operating at 1400 nm [49]. One can expect further PCE enhancement by applying a novel pumping scheme consisting of 790 nm laser diode and simultaneously operating laser at about 1900 nm, which is used to depopulate the first excited energy level.

The next three chapters deal with key issues important for the design of the thulium-doped fiber amplifiers. The spectroscopic properties as well as the fiber couplers and the low-loss connection technique determine the performance of the amplifier and therefore they are discussed in separate chapters.

3   Spectroscopic properties of thulium in fluoride glasses

The performance of a rare-earth doped fiber amplifier depends on several parameters. One can divide them into three groups. The first one collects the geometrical parameters of the active fiber (core radius, length). The refractive index, numerical aperture, and attenuation are representatives of optical parameters of the active fiber. The third group consists of the spectroscopic properties of the dopant ions in the host glass. Since the second and third group influence each other, the geometrical parameters stay independent and do not interfere with any other group. The performance of the optical fiber amplifier depends strongly on the absorption and emission properties of the dopant in the host glass system. On the other hand the lifetimes of the individual energy levels determine the efficiency of the transitions starting from that level. Last but not least, the data gained from spectroscopic experiments are used for the amplifier simulations described in chapter 6. For all these reasons the spectroscopic investigations are important for the design of the fiber amplifier and help to predict its performance.

Thulium is one of the lanthanides and due to the electronic configuration its spectroscopic properties are relatively host-glass independent [58]. In the atomic structure of the lanthanides the orbital shells 5s, 5p and 6s, resembling nobel gas configuration, are fully populated with the electrons. However, the lower lying 4f shell is only partially populated and the number of 4f electrons determines the optical properties of the individual lanthanide. Since the not completely filled 4f shell is surrounded by the fully populated 5s, 5p and 6s shells the interactions with host glass are minimal, which results in sharp absorption and emission lines. This makes the rare-earth doped glasses very attractive for fiber amplifier and laser applications.

The energy states of the rare-earth ions are assigned using the LS description proposed by Russell-Saunders [64]. According to it, three quantum numbers S, L and $J = S + L$, where J is the total angular momentum, are used to describe every energy state. This leads to the following notation:

$$^{2S+1}L_J,$$

and the quantum number L is substituted by a letter according to following rule:

$$L \Rightarrow S, P, D, F, G, H, I \text{ for } L = 0, 1, 2, 3, 4, 5, 6.$$

Since the energy states in lanthanides are in general mixed LS states, the dominating LS-component is used for the choice of the L and S number of the state label. Unfortunately, there is also another labelling system, which does not take care of the spin-orbit coupling in the rare-earths. In most cases it leads to the same labels of the energy levels. However,

the $^3H_4$ and $^3F_4$ states in thulium are in these systems exchanged. In order to avoid the misunderstandings we will use the first labelling convention which is also shown in figure 3.1.
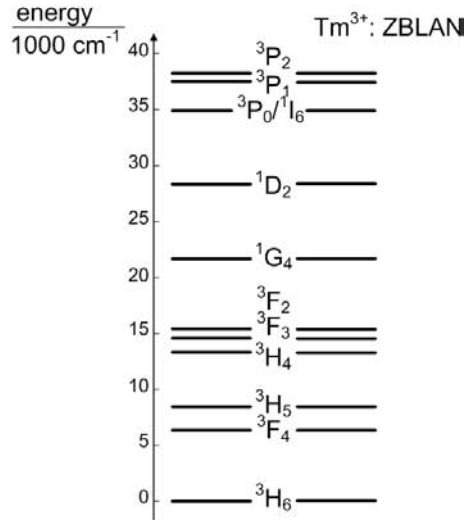
Figure 3.1: Energy levels of triply ionized thulium ion

The most stable form of thulium element is its triple ionized ion (Tm^{3+}). Its electron configuration is $|Xe|4f^{12}$ and the measured absorption and emission spectra are the result of electron transitions between allowed states inside 4f shell. Due to shielding of fully populated 5s and 5p shells the transitions are strong and narrow. Therefore thulium ions behave in principle like free ions and their energy level structure is only slightly affected by the neighbor atoms. Nevertheless, the limited broadening of the absorption lines can be observed due to Stark level splitting. This process is the result of splitting the electronic spectral lines due to the local electric field caused by neighboring atoms. The splitting of the energy levels by an electric field first requires that the field polarizes the atom and then interact with the resulting electric dipole moment. The splitting caused by Stark effect is relatively small (about 10 to $100\,cm^{-1}$) and depends on the energy level and the energy distance between the resulting sub levels. The total width of the splitting is about $200\,cm^{-1}$.

Some of the spectroscopic parameters such as radiative transmission rates (A_{ij}), branching ratios (β) or oscillator strengths (f_{ed}), which are very important for the amplifier simulations are difficult to measure. On the other hand, they can be calculated using the energy level fit described in details in [58]. This technique along with the Judd-Ofelt theory [65, 66], delivers the missing parameters. According to the theory one can calculate the oscillator strengths f_{ed} for all transitions inside the ground configuration of a rare earth ion based on just three

fit parameters Ω_2, Ω_4 and Ω_6, according to the equation:

$$f_{ed} = \frac{8\pi^2 m_e \nu \chi_{ed}}{3h(2J_i + 1)} \sum_{\lambda=2,4,6} \Omega_\lambda \left| \langle i \| \mathbf{U}^{(\lambda)} \| f \rangle \right|^2 , \tag{3.1}$$

where m_e is the electron mass, ν is the frequency of the transition, h is Planck's constant and J_i is the quantum number of the total angular momentum of the initial state. The dielectric correction factor χ_{ed} is $n(n^2 + 2)^2/9$ for spontaneous emissions and $(n^2 + 2)^2/9n$ for absorptions and stimulated emissions and n is the refractive index of the host material. The second factor in the sum besides the Judd-Ofelt parameter is the squared reduced matrix element of the unit tensor operator $U^{(\lambda)}$ of rank λ between the initial state i and the final state f. The whole procedure, which has to be applied to calculate the oscillator strengths for thulium in ZBLAN and IBZP is described in [67].

The advantage of the Judd-Ofelt theory lies in the fact that once the the Judd-Ofelt parameters are known, the oscillator strengths of any transitions can be calculated. Furthermore from the oscillator strengths one can calculate the transition rates for spontaneous radiative transitions using the following equation:

$$A_{ij} = \frac{2\pi \nu^2 e^2}{\varepsilon_0 m_e c^3} f_{ij} , \tag{3.2}$$

where ε_0 is the dielectric constant and c is the speed of light in vacuum. The radiative lifetime of state i is given by:

$$\tau_{i,rad} = \frac{1}{\sum_j A_{ij}} \tag{3.3}$$

and the branching ratio for the transition $i \to j$ is:

$$\beta_{ij} = \frac{\tau_i}{A_{ij}} . \tag{3.4}$$

All spectroscopic measurements presented here were performed in room temperature for two glass compositions (ZBLAN and IBZP) developed and investigated in our institute. They are representatives of low phonon energy glasses and their names are acronyms built from the first letters of their main components. The first investigations on ZBLAN glass matrix were reported already in 1975 [68]. Since then, different glass compositions have been developed [69–72] and the properties of different rare-earth ions have been explored with respect to the use of the fluoride glasses as host glasses for different fiber amplifiers or lasers. The IBZP is a representative of another LPE glass family (based on indium fluoride) and development of that glass type started in 1983 [73, 74], and up to today different stable compositions were reported [75, 76].

The dimensions of glass probes used for measurements are collected in table 3.1 along with the dopant concentrations p. The basic composition of the glasses in mol% was as follows:

ZBLAN: $53\text{ZrF}_4 - 20\text{BaF}_2 - 3.875\text{LaF}_3 - 3\text{AlF}_3 - (20-x)\text{NaF} - 0.125\text{InF}_3 - x\text{PbF}_2$,
IBZP: $28\text{InF}_3 - 18\text{BaF}_2 - 20\text{ZnF}_2 - 4\text{SrF}_2 - 6\text{PbF}_2 - 5\text{YF}_3 - 7\text{AlF}_3 - 2\text{LiF} - 10\text{NaF}$.

Table 3.1: Dimensions and thulium concentrations of the glass probes used for spectroscopic experiments. The dimensions are mean values of three measurements and their uncertainty is $\pm\, 0.10\,\text{mm}$.

sample	p mol%	A mm	B mm	C mm	sample	p mol%	A mm	B mm	C mm
pure ZBLAN					pure IBZP				
Z0	-	8.31	15.33	19.97	I0	-	8.67	14.94	18.05
Tm^{3+} : ZBLAN					Tm^{3+} : IBZP				
Z1	2.992	9.88	13.33	22.23	I1	2.998	8.73	15.85	n.p.
Z2	1.980	8.85	13.43	17.73	I2	2.000	8.80	13.70	15.48
Z3	1.074	8.08	11.98	12.83	I3	1.001	8.38	15.80	n.p.
Z4	0.603	9.18	14.55	17.15	I4	1.001	8.63	11.33	16.58
Z5	0.300	8.70	15.35	17.25	I5	0.511	8.34	17.85	n.p.
Z6	0.200	8.85	13.15	16.83	I6	0.317	8.35	15.25	n.p.
Z7	0.107	8.45	14.70	17.80	I7	0.200	9.45	10.23	17.88
Z8	0.010	8.84	13.21	16.26	I8	0.101	8.38	12.20	16.03
					I9	0.010	8.14	11.53	15.57

For the thulium doping, LaF_3 was exchanged with TmF_3 in the case of ZBLAN. In IBZP glass YF_3 was replaced by TmF_3. For the fiber applications, glass with larger refractive index is needed. This might be achieved by partial substituting NaF with PbF_2 in the case of ZBLAN glass and changing the ratio of $\text{BaF}_2 - \text{SrF}_2 - \text{NaF} - \text{PbF}_2$ in the case of IBZP glass.

The pure ZBLAN and IBZP were used to determine the basic absorption of the glass composition and its transmission window. The purity of the raw materials was higher than 99.99 %. Batches of 20 g were melted in platinum crucibles under dry nitrogen atmosphere ($\text{H}_2\text{O} < 1\,\text{ppm}$) 30 min at 800 °C and 30 min at 900 °C for fining. After casting the melt was filled into a brass mold which was preheated to 260 °C. The glass sample was then cooled down slowly to room temperature. The polished bulk glasses were homogeneous and without bubbles. The samples were stable under ambient atmosphere and the room temperature and did not show any visible alteration of the surface.

For modelling of thulium-doped fiber amplifiers a number of transitions are of special

interest. They all can be divided into three groups as shown in figure 3.2.
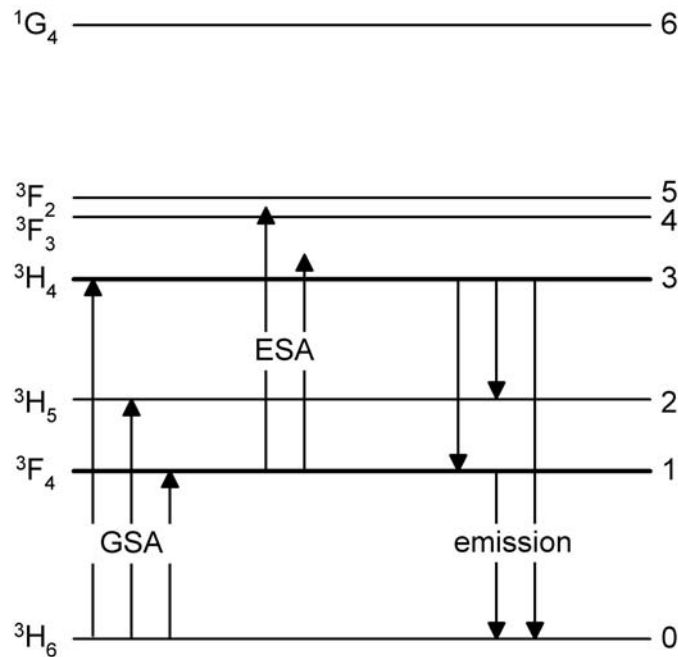
Figure 3.2: Important optical transitions in the energy level diagram of thulium ion

The energy levels are labelled in two ways: first with the full label resulting from the quantum physics as it is shown on the left side, but for the simplicity they are also signed with numbers starting with 0 and ending with 6, as one can see on the right side. Such dual-notation is sometimes more convenient and it will be use in the further description. The transitions labelled as **GSA** in figure 3.2 resemble ground state absorptions and are especially important for pumping process. The results of ground state absorption measurements are discussed in section 3.2. The second group of the transitions called **ESA** collects excited state absorptions starting from the first excited level. They play an important role for choosing second pump wavelength for the fiber amplifier. On the other hand, ESA centered at approx. 1420 nm has an influence on signal wavelengths and therefore is always important. The **emission** transitions from any excited level are relevant for signal amplification but also for building up the laser oscillations e.g. at approx. 1900 nm, which are used in the novel pumping scheme for the amplifier described in chapters 6.3.3 and 7.4.2. The results of emission measurements and ESA-spectroscopy are described in details in sections 3.4 and 3.3 respectively. Finally the results of lifetime measurement for the lower and upper amplification level are reported in section 3.5, and the problem of lifetime quenching is discussed in section 3.5.2. But before we begin with the absorption spectroscopy let us concentrate on one of the basic spectroscopic

measurement, which is the determination of the refractive index.

3.1   Refractive index measurement for ZBLAN and IBZP glass samples

The refractive index spectra were measured in the wavelength region from 250 to 1600 nm. The measurements were performed for ZBLAN and IBZP glass samples containing 2.5 and 16 mol% of PbF_2 respectively. Since the lead amount in fibers used for amplifier investigations was 4 mol%, the refractive index of a probe with composition corresponding to the core glass was also measured. For the calibration of the measurement the refractive index of standard silica glass (BK7) was measured and the results were compared with calculation basing on the dispersion parameters given in the glass specification. The calibrated spectra for ZBLAN and IBZP glasses are shown in figure 3.3.
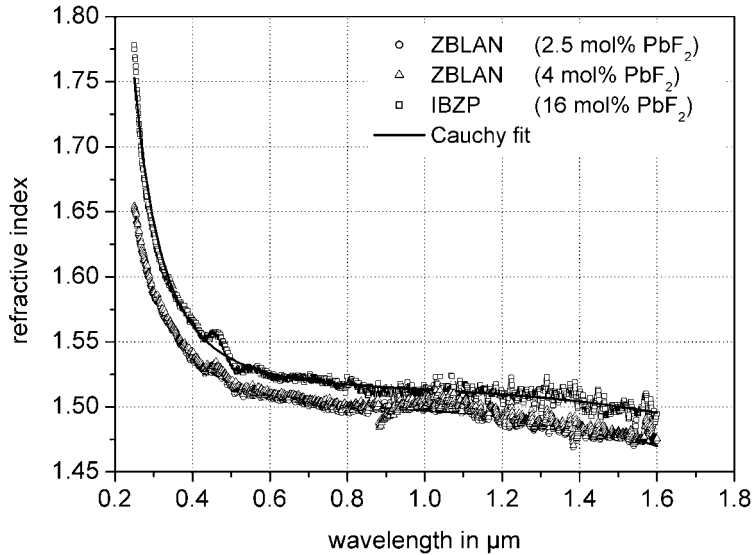
Figure 3.3: Measured refractive indices of ZBLAN and IBZP glasses

The measurement data were fitted using the Cauchy formula

$$n(\lambda) = A\lambda^{-4} + B\lambda^{-2} + C + D\lambda^2 + E\lambda^4 \;, \tag{3.5}$$

and the calculated parameters A - E are collected in table 3.2 for IBZP as well as for ZBLAN sample consisting 2.5 mol% of PbF_2. For comparison the parameters for slightly different

ZBLAN glass reported in [77] were also given.

Table 3.2: Parameters for Cauchy approximation of the refractive index measurements

parameter	ZBLAN	IBZP	ZBLANIPb[a]
A in μm^4	$(2.30 \pm 0.10) \cdot 10^{-4}$	$(6.70 \pm 0.20) \cdot 10^{-4}$	$-3.05390 \cdot 10^{-5}$
B in μm^2	$(6.78 \pm 0.10) \cdot 10^{-3}$	$(4.74 \pm 0.34) \cdot 10^{-3}$	$3.33275 \cdot 10^{-3}$
C	1.4847 ± 0.0011	1.5057 ± 0.0014	1.49599
D in μm^{-2}	$(1.34 \pm 0.12) \cdot 10^{-2}$	$(6.52 \pm 1.69) \cdot 10^{-3}$	$-1.31147 \cdot 10^{-3}$
E in μm^{-4}	$-(7.91 \pm 0.40) \cdot 10^{-3}$	$-(4.42 \pm 0.53) \cdot 10^{-3}$	$-2.57889 \cdot 10^{-6}$
reference	here	here	[78]

Notes:
[a] glass composition: $52ZrF_4 - 20BaF_2 - 5LaF_3 - 4AlF_3 - 15NaF - 3InF_3 - 1PbF_3$

Since the the Cauchy formula fits the measurements very well it is also used for the prediction of the refractive indices beyond 1600 nm. However, the measurements for the wavelengths above 900 nm scatter strongly due to the low reflection power in IR region emitted from the white light source and weak sensitivity of the detector. It can influences the Cauchy fit, however the measured refractive indices are in a good agreement with the control measurements performed for the glass samples using Abbe refractometer. The control measurements were performed at the wavelength of 589.3 nm corresponding to the D-line of natrium. The measured refractive index for ZBLAN is 1.5078 and 1.5242 for IBZP, which agree with 1.5086 and 1.5264 measured using the ellipsometer for ZBLAN and IBZP samples respectively. The accuracy of measurements was measured to be better than $\pm$ 0.0005. The minor difference was found between both ZBLAN probes and the refractive index at 589.3 nm for ZBLAN containing more lead was 1.5101. Some discrepancies between fit parameters achieved by the author and reported in [78] can result from slightly different glass compositions of samples used by L. Wetenkamp, which contained only 1 mol% of PbF_3. Increasing the lead concentration to 2.5 mol% one can arise the refractive index and vertically shift its spectrum towards higher n values, which was also observed here.

Since the measurement setup described in [78] allowed the refractive index estimation starting from 500 nm, some important data are missing comparing to the measurements presented in this work. Nevertheless, measurement performed here and the results of the Cauchy fit were used for the further spectroscopic calculations.

3.2 Ground State Absorption (GSA)

Since absorption processes in thulium are very important for modelling of the TDFA they were measured and recalculated to cross-sections commonly used in amplifier simulations. To

complete the data set all absorptions up to the ultraviolet were identified. This makes possible to compare both glass systems as potential host glasses for the thulium-doped fiber amplifier.

3.2.1   Measurement setup and procedure

The absorption transitions in thulium cover the wavelength range from deep ultraviolet to far infrared. Not all of them are strong enough to be measured at room temperature (like e. $^3H_4 \rightarrow {}^3F_3$ at $5.3\,\mu$m or $^3H_4 \rightarrow {}^3F_2$ at approx. $4.2\,\mu$m). Some of them also exceed the transmission window of the glass matrix (like all transitions terminating in the $^1S_0$ level), but such a broad wavelength range can not be measured using one detector only. Therefore two different absorption spectrometers were used during the experiments presented in this work. One of them was UV-VIS-IR monochromator based spectrometer (Cary 5, Varian) working in the wavelength range from 175 to 3300 nm. In principle, using this spectrometer it is possible to measure the absorption also above 1000 nm, but this region can be covered also by Fourier transform (FT) spectrometer, which delivers the measurement much faster than in the case of monochromator based spectrometer, where the minimal measurement time is limited by the driving time of the monochromator. In spite of low dynamic range, the FT spectrometer became a standard in infrared wavelength region, where the spectral intensity of light sources and the ability to detect the radiation are very limited. Therefore the measurements in the wavelength region of 175 to 1000 nm were performed with Cary 5 spectrometer and the absorption wavelengths of 630 to 8000 nm were covered by the FT-IR spectrometer (IFS 25, Bruker) featured with the Si- and HgCdTe-detector. For the measurements up to 1000 nm the Si-detector was applied, and above that wavelength we used the HgCdTe-based detector.

The absorption measurement, independent of used spectrometer, occurs in two steps. During the first step the reference spectrum $I_{ref}(k)$ combining spectral characteristics of light source, monochromator, and optical components is measured. In the second step the spectrum with the glass sample $I(k)$ is recorded. The transmission of the sample can be calculated by comparing both spectra according to the equation:

$$T(k) = \frac{I(k)}{I_{ref}(k)} \ , \tag{3.6}$$

or in the form of absorbance:

$$A(k) = -\log \frac{I_{ref}(k)}{I(k)} \ . \tag{3.7}$$

The spectroscopic measurements are typically presented in graphs, in which the "X-axis" is given in wavenumbers k corresponding to the energy and scaled in cm^{-1}. We decided to use this convention also in this work, but since the wavelength unit used in this work is nanometer, the measured values can be easily recalculated using the following relation:

$$\lambda \text{ in nm} = \frac{10^7}{k \text{ in } cm^{-1}} \; . \tag{3.8}$$

Nevertheless, all measurement results collected in tables are given in wavenumbers as well as nanometers to make their interpretation easier.

3.2.2 Measurement of the intrinsic losses for ZBLAN and IBZP glasses

The transmission bandwidth of the glass matrix is one of the basic spectroscopic measurements, which supports information about the characteristic attenuation of the glass and its UV and IR absorption edges. It is obvious, that a decrease in the phonon energy, what is the case in IBZP comparing to ZBLAN, causes a red shift in the IR absorption edge.

The basic attenuation curve of any glass sample follows the simplified equation [56]:

$$\alpha_{base} = A \exp\left(\frac{a}{\lambda}\right) + \frac{B}{\lambda^4} + C \exp\left(-\frac{c}{\lambda}\right) \tag{3.9}$$

where A, a, B, C, and c are the material parameters and λ is the wavelength. The first term in the equation corresponds to the absorption caused by electron transitions from the valence band to the conduction band, which occurs for highly energetic excitations (in UV wavelength region). The second term describes the attenuation due to the Rayleigh scattering, and it is present in the whole transparency band. The third term formalizes the absorption due to matrix vibration in the glass probe. Since IBZP is supposed to have lower phonon energy, one can expect that this glass is transparent for the longer wavelengths. The results of the transmission window measurement were shown in figure 3.4.

The intrinsic absorption spectra were measured for pure ZBLAN and IBZP samples, with the dimensions given in table 3.1. The middle part of the spectra described actually by Rayleigh equation shows the attenuation slightly higher than expected. Its value for ZBLAN is about $0.005 \, \text{dB}$ for $5000 \, \text{cm}^{-1}$ [58]. The measured value was about 10 times larger and was caused by remaining losses in the glass sample (scattering on the microdefects or impurities).

As expected, the IR range for IBZP glass is shifted towards longer wavelengths (smaller wavenumbers), but simultaneously the UV edge shifted to slightly longer wavelength. The difference in spectra for the shorter wavelengths seems to be larger, which is only caused by the axis scaling. The transmission windows for both glasses defined as region with a transmission higher than $50 \, \%$ (or absorption smaller than $3 \, \text{dB}$) are collected in table 3.3. For comparison, the transmission edges of the SiO_2 fiber are also given [79].

The bright transmission window of the heavy-metal fluoride glasses opens new possibilities for rare-earth based lasers [80, 81] or fiber amplifiers for the wavelengths above third telecommunication window [82]. The low intrinsic loss for the fibers made of these glasses
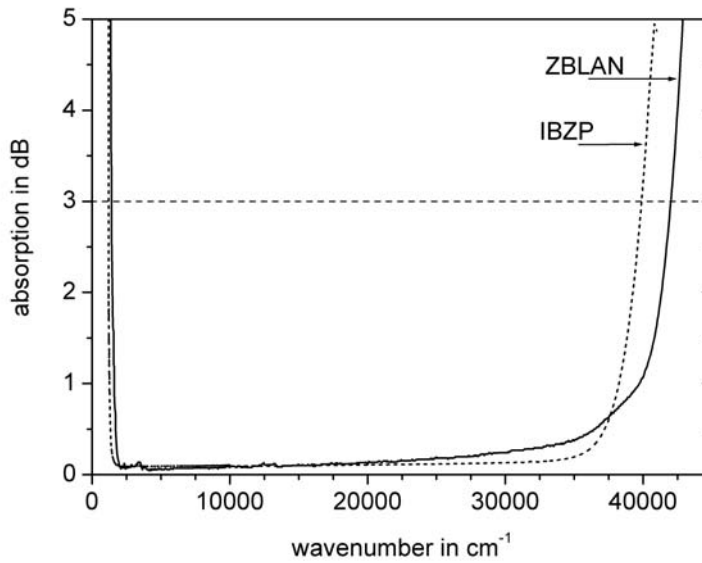
Figure 3.4: Transmission window for ZBLAN and IBZP glass probes

Table 3.3: Measured absorption edges of ZBLAN and IBZP glasses

glass	UV edge in cm^{-1}/nm	IR edge in cm^{-1}/nm
ZBLAN	41841/239	1311/7630
IBZP	39682/252	1201/8330
SiO_2	55555/180	4000/2500

was previously expected to be as small as 0.001 dB/km at around 2500 nm [77]. The practice shows, that such a low attenuation can not be reached because of the low temperatures needed to manufacturing the fibers, which does not assure rejection of the rest impurities in the glass melt. Typical attenuation of the ZBLAN fibers is much higher and losses as low as 0.05 dB/m at 1400 nm were reported for thulium-doped fibers [82].

3.2.3   Analysis of measured spectra

The absorption measurement on the thulium-doped glass samples delivers raw attenuation spectra containing also losses caused by Fresnel reflections from the sample surfaces. Therefore it is common that some intensity offset occurs and the spectral lines do not begin and

end with an intensity close to zero, which makes baseline correction necessary. However, it is important to note that, the base line correction has to be performed after splitting the whole measures spectrum into particular absorption lines. The absorption measurement of Tm^{3+}:ZBLAN glass and its baseline correction are shown in figure 3.5.
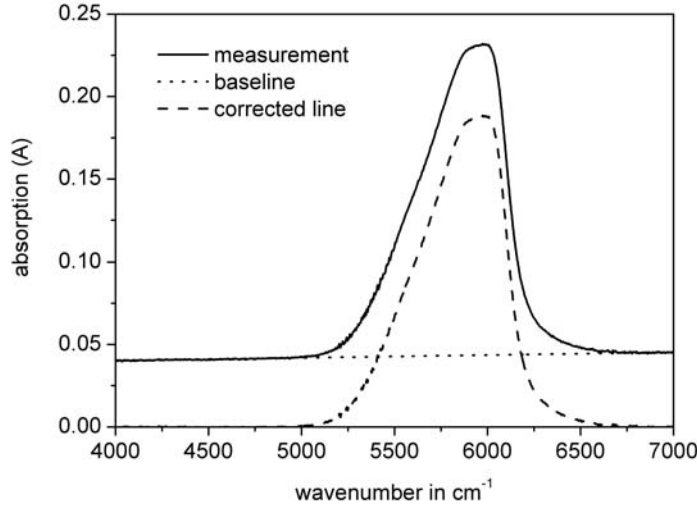
Figure 3.5: Baseline correction for $^3F_4$ line in thulium-doped ZBLAN glass sample (Z4)

As a next step, the corrected spectra were recalculated into cross-sections, using the following equation:

$$\sigma_{GSA}(k) = \frac{A(k)}{lp\gamma} \ , \tag{3.10}$$

where l, p, and γ are the length of the light path in the glass sample, its dopant concentration in mol% and the material specific conversion factor, respectively. The dopant concentration p is the amount of thulium in mol (N_d) in the total amount of glass ingredients and it is given by:

$$p = \frac{N_d}{\sum N_i} \ . \tag{3.11}$$

The conversion factor enables dopant conversion from its molar concentration into the ion density n_I and it is formalized as:

$$\gamma = \frac{\varrho N_A}{M} \; , \tag{3.12}$$

where ϱ is the mass density, N_A is the Avogadro's constant and M is the molar mass of the glass composition.

The mass density of fluoride based glass was found for ZBLAN to be $4.33\,\mathrm{g/cm^{-3}}$ which leads to the conversion factor equal to $1.84 \cdot 10^{22}\,\mathrm{cm^{-3}}$. The mass density used in this work for further calculation is in good agreement with the literature: $4.31\,\mathrm{g/cm^{-3}}$ in ZBLAN [83] or $4.414\,\mathrm{g/cm^{-3}}$ in ZBLANP [84]. The mass density for IBZP was found to be $5.2\,\mathrm{g/cm^{-3}}$ and the conversion factor $2.27 \cdot 10^{22}\,\mathrm{cm^{-3}}$. This value is also in good agreement with values published in literature. The glass density for the similar glass composition (IZnSBC) was reported to be $5.1\,\mathrm{g/cm^{-3}}$ [85]. The values of 4.94 to $5.0\,\mathrm{g/cm^{-3}}$ were reported in [86] for several indium based fluoride based compositions.

The absorption measurements were carried out for all glass samples at least three times by taking every sample out of the spectrometer and inserting it again. This helped to avoid accidental errors caused by local impurities or crystals in the bulk glass, which can adulterate the measurement. It was also observed that the calculated absorption cross-sections did not show significant dependence on the thulium concentration. The results of the measurement in form of cross-section are shown for both glasses in figure 3.6. For their better comparison, the peak values $\overline{\sigma}_{GSA}$ along with their accuracy $\Delta\sigma_{GSA}$, peak wavelength λ_p and appropriate wavenumber k were collected in table 3.4 and table 3.5 for ZBLAN and IBZP glasses respectively.

The spectra shown in figure 3.6 represent the average absorption cross-sections resulting for all measurements performed for different samples (up to 8 samples and 3 measurements for each probe), and their accuracy was calculated as a standard error of the mean value (SEM) defined as:

$$\Delta\sigma_{GSA} = \sqrt{\frac{1}{a(a-1)} \sum_{i=1}^{a} a(\sigma_{GSA_i} - \overline{\sigma}_{GSA})} \; , \tag{3.13}$$

where a is the number of measurements and $a = 24$, σ_{GSA_i} is the peak value of the cross-section for the ith measurement and $\overline{\sigma}_{GSA}$ is the mean value for all GSA measurements.

For all detected transitions oscillator strengths were calculated according to the equation:

$$f = \frac{4\varepsilon_0 m_e c^2}{e^2} \int \sigma_{GSA}(k) \; dk \; , \tag{3.14}$$

where ε_0, m_e, c, and e are the dielectric constant, mass of the electron, velocity of light in vacuum, and the single electron's charge, respectively. Before the calculation of the oscillator strengths the lines were separated using a multiple Gaussian fit, in the cases where the
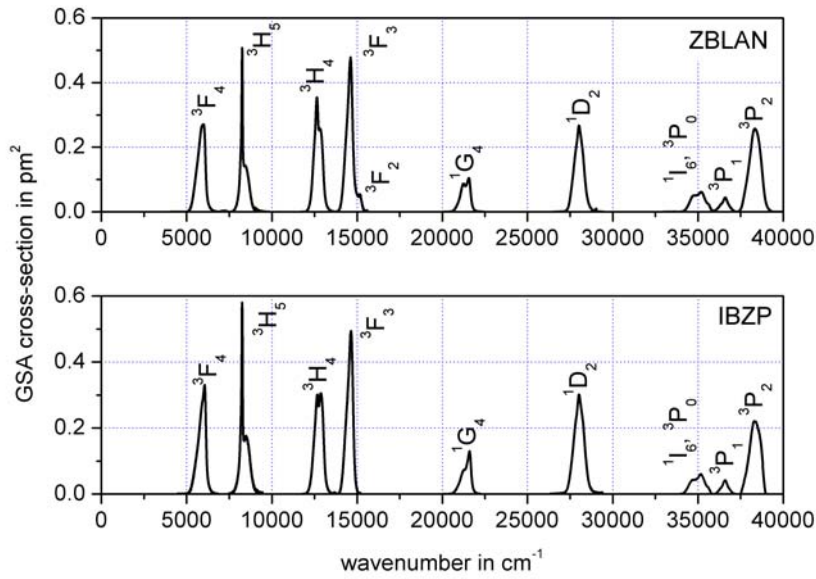
Figure 3.6: Averaged absorption cross-sections for thulium-doped ZBLAN and IBZP glass samples

lines were not separable only one f was calculated. In the table 3.6 all calculated oscillator strengths are collected along with their errors calculated as standard error of the mean value.

All absorption lines of thulium were measured except of $^3F_2$ transition in IBZP, which is relatively weak and disappears in the rest absorption caused by much stronger and brighter $^3H_6 \rightarrow ^3F_3$ transition. Also the absorption terminating in the $^1S_0$ level was not observed, but the expected peak wavelength of it was about 133 nm (or 75000 cm^{-1}), which is below the UV-absorption edge for both glass types. The energy levels calculations reported in [58] shown that the levels $^1I_6$ and $^3P_0$ are not separable and the two-peak absorption line can be not related to the energy difference of these two levels. For that reason these two levels as recognized as a one.

The relative uncertainties for the measurement values are almost in every case below 10 %, only in some cases (like for $^1D_2$ level in ZBLAN) they increase significantly, which can be explained through the differences in measurement accuracy for single measurements performed for different probes. The higher discrepancies in measurements for $^3P_2$ line in IBZP might be easily referred to lower transmission of glass and the neighborhood of the UV - absorption edge. The remaining differences are caused by microscopic defects in the samples (microcrystals, microbubbles or local differences in refractive index) coming from the manufacturing process (melting, casting and polishing).

Table 3.4: Measured ground state absorption cross-section peaks for thulium in ZBLAN glass

level	k_p in cm^{-1}	λ_p in nm	$\overline{\sigma}_{GSA} \pm \Delta\sigma_{GSA}$ in pm^2	rel. in %
$^3F_4$	5945.9	1681.80	0.269 ± 0.001	0.37
$^3H_5$	8256.2	1211.21	0.486 ± 0.007	1.44
$^3H_4$	12638.9	791.21	0.362 ± 0.009	2.49
	12834.3	779.16	0.263 ± 0.008	3.39
$^3F_3$	14605.4	684.68	0.457 ± 0.033	7.22
$^3F_2$	15170.4	659.18	0.051 ± 0.001	1.96
$^1G_4$	21242.7	470.75	0.087 ± 0.004	4.60
	21558.5	463.85	0.105 ± 0.010	9.52
$^1D_2$	28017.5	356.92	0.270 ± 0.030	11.11
$^1I_6, {}^3P_0$	34806.8	287.30	0.051 ± 0.001	1.96
	35186.5	284.20	0.062 ± 0.002	3.22
$^3P_1$	36603.2	273.20	0.044 ± 0.003	6.82
$^3P_2$	38333.3	260.87	0.257 ± 0.004	1.55

Notes:
rel. - relative uncertainty

The results of the measurements are in a good agreement with the theory. We proved, that the positions of the absorption line show only minor host dependency. However, the cross-section values are different for ZBLAN and IBZP and the measured values for transitions in IBZP are larger for almost all transitions. This phenomenon can be explained by the fact that all transitions inside the 4f shell are parity forbidden and can occur only due to the interactions with the glass matrix. Also the lineshape of some absorption lines (e.g. $^1G_4$ and $^3H_4$) is different in both glasses, which is caused by different Stark splitting of the energy level.

3.2.4   Comparison with the literature

Since the measurement presented in this work were performed for two glass types, which were developed and optimized for applications in the IR wavelength region containing fiber amplifier and fiber laser, it is essential to compare our results with other publications. For that reason measured GSA cross-sections and oscillator strengths are compared with the results of the published spectroscopic experiments.

The comparison of GSA cross-sections is given in table 3.7 and the measured oscillator strengths in different glass hosts are collected in table 3.8. The measured GSA cross-sections are in a good agreement with the values published in the literature and the differences between

Table 3.5: Measured ground state absorption cross-section peaks for thulium in IZBP glass

level	k_p in cm^{-1}	λ_p in nm	$\overline{\sigma}_{GSA} \pm \Delta\sigma_{GSA}$ in pm^2	rel. in %
$^3F_4$	6050.8	1652.68	0.329 ± 0.010	3.04
$^3H_5$	8253.5	1211.60	0.578 ± 0.021	3.63
$^3H_4$	12669.1	789.32	0.309 ± 0.010	3.23
	12872.9	776.82	0.310 ± 0.010	3.39
$^3F_3$	14633.4	683.37	0.513 ± 0.049	9.55
$^3F_2$	not identified			
$^1G_4$	21292.4	469.65	0.071 ± 0.001	1.40
	21595.9	463.05	0.127 ± 0.002	1.57
$^1D_2$	28017.1	356.92	0.301 ± 0.003	0.99
$^1I_6, {}^3P_0$	34746.4	287.80	0.047 ± 0.001	2.12
	35167.9	284.35	0.066 ± 0.001	1.51
$^3P_1$	36596.5	273.25	0.044 ± 0.001	2.27
$^3P_2$	38328.9	260.90	0.219 ± 0.020	9.13

Notes:
rel. - relative uncertainty

Table 3.6: Measured oscillator strengths for thulium lines in ZBLAN and IZBP glasses

level	$f_{ZBLAN} \pm \Delta f$ 10^{-8}	rel. in %	$f_{IBZP} \pm \Delta f$ 10^{-8}	rel. in %
$^3F_4$	186.94 ± 1.08	0.58	191.23 ± 2.13	1.13
$^3H_5$	154.56 ± 2.94	1.90	178.52 ± 3.14	1.76
$^3H_4$	208.14 ± 3.56	1.71	215.31 ± 2.99	1.39
$^3F_3 + {}^3F_2$	272.34 ± 5.36	1.96	259.60 ± 2.94	1.13
$^1G_4$	74.32 ± 6.61	8.89	84.97 ± 7.44	8.75
$^1D_2$	195.83 ± 9.58	4.89	241.01 ± 8.78	3.64
$^1I_6 + {}^3P_0$	68.08 ± 6.73	9.88	62.47 ± 4.12	6.59
$^3P_1$	26.11 ± 1.58	6.05	22.1 ± 1.48	6.69
$^3P_2$	248.78 ± 11.25	4.52	208.32 ± 10.14	4.87

Notes:
rel. - relative uncertainty

the values reported here and in other references is lower than 10 % which is common for such a measurements.

The measurements show, that the GSA pump wavelengths for TDFA does not need to be chosen very precisely, because of the relatively broad transition line. Although the lines are

Table 3.7: Comparison of ground state absorption cross-section peaks for different host materials. Values are given in pm^2.

level	ZBLAN	ZBLAN	ZBLAN[a]	IBZP	tellurite[b]	SiO$_2$
$^3F_4$	0.269	0.287	0.232 / 0.258	0.329	0.253 - 0.277	0.437
$^3H_5$	0.486	0.530	0.360 / 0.367	0.578	0.415 - 0.473	0.456
$^3H_4$	0.362	0.344	0.330 / 0.360	0.309	0.380 - 0.403	0.850
	0.263	-	0.240 / 0.247	0.310	-	-
$^3F_3$	0.457	0.515	0.495 / 0.517	0.513	0.415 - 0.461	0.318
$^3F_2$	0.051	0.060	0.057 / 0.060	n.i.	0.034 - 0.046	-
$^1G_4$	0.087	0.087	0.075 / 0.075	0.071	0.023 - 0.034	-
	0.105	0.105	0.090 / 0.060	0.127	0.092 - 0.161	-
$^1D_2$	0.270	0.270	0.225 / 0.337	0.301	-	-
$^1I_6$	0.051	0.051	- / -	0.047	-	-
$^3P_0$	0.062	0.062	- / -	0.066	-	-
$^3P_1$	0.044	0.044	- / -	0.044	-	-
$^3P_2$	0.257	0.257	- / -	0.219	-	-
ref.	here	[58]	[87]	here	[88]	[89]

Notes:
n.i. - not identified,
"-" not measured or not calculated,
[a] first value is measured, second calculated
[b] glass compositions: $60TeO_2 - 40ZnCl_2$, $75TeO_2 - 20ZnO - 5Na_2O$, $75TeO_2 - 10ZnO - 10PbO - 5Nb_2O_3$

centered by 791 nm and 789 nm for ZBLAN and IBZP respectively, their full width at half maximum (FWHM) is about 30 nm. Similarly, the absorption into the $^3F_4$ level, centered at 1681 nm for ZBLAN and at 1652 nm for IBZP, is broad enough to expect an efficient depleting of the first excited state when the fiber laser at approx. 1900 nm is employed as in the pumping scheme described in chapters 6.3.3 and 7.4.2.

As reported in [90], transition into $^3F_{2,3}$ levels centered by approx. 690 nm in both glasses can be also used for pumping thulium-doped fiber amplifier and together with radiation at 1400 nm delivers approx. 30 dB gain at 850 nm for 56 mW pump power at 690 nm and 257 mW at 1400 nm.

Since the absolute values of GSA cross-section are published rarely it is more convenient to compare oscillator strengths of the particular absorption lines in the different host glasses. As shown in table 3.8, the values measured by the author corresponds to that given in references, especially in the case of ZBLAN glass. The discrepancies between measurements presented here and reported in the literature are larger in the case of indium based glasses, which could be caused by the differences in their composition. Compared to ZBLAN, indium fluoride

based glasses show larger oscillator strengths, which was already obvious when GSA cross-sections were compared. The summary contains also oscillator strengths of two non-fluoride glasses. For glass called here SACPY, the measured oscillator strengths shows only minor dissimilarity, which is not the case for chalcogenide GGLS glass, where the oscillator strengths are much larger than in any other glass composition presented here. This suggests that this glass can even be a better host for the TDFA.

Table 3.8: Comparison of measured oscillator strengths for GSA cross-section peaks in different host glasses. Values are given in 10^{-8}.

level	ZBLAN	ZBLAN	IBZP	IZBS[a]	IZBS[b]	BIZYT[c]	SACPY[d]	GGLS[e]
$^3F_4$	186.94	187	191.23	165	165	161	233	751
$^3H_5$	154.56	156	178.52	144	164	-	146	423
$^3H_4$	208.14	201	215.31	261	191	185	293	865
$^3F_3 + ^3F_2$	272.34	275	259.60	359	317	289	358	952
$^1G_4$	74.32	75	84.97	123	69	64	109	-
$^1D_2$	195.83	195	241.01	278	231	195	-	-
$^1I_6 + ^3P_0$	68.08	68.5	62.47	-	-	80	-	-
$^3P_1$	26.11	26	22.10	-	-	30	-	-
$^3P_2$	248.78	246	208.32	-	-	196	-	-
ref.	here	[58]	here	[91]	[92]	[93]	[94]	[95]

Notes:
"-" - not measured,
[a] glass composition: $(40 - x)InF_3 - 20ZnF_2 - 16BaF_2 - 20SrF_2 - 2GdF_3 - 2NaF - xTmF_3$,
[b] glass composition: $36InF_3 - 16BaF_2 - 20ZnF_2 - 20SrF_2 - 6GaF_3 - 2NaF$,
[c] glass composition: $30BaF_2 - 30InF_3 - 20ZnF_2 - (10 - x)YF_3 - 10ThF_4 - xTmF_3$,
[d] glass composition: $30SiO_2 - 15Al_2O_3 - 29CdF_2 - 22PbF_2 - (4 - x)YF_3 - xTmF_3$,
[e] glass composition: $Ga_2S_3 - GeS_2 - La_2S_3$

3.3   Excited State Absorption (ESA)

In the previous sections the GSA measurements were discussed in details, but for modelling of TDFA also the absorption starting from the first excited state plays a fundamental role. It is used for a secondary pump, which allows to achieve population inversion between $^3F_4$ and $^3H_4$ levels, which is not possible when using only GSA around 790 nm. One of the relevant excited state absorption lines is the transition $^3F_4 \rightarrow ^3F_{2,3}$ with its peak at approx. 1050 nm, another one is that centered at approx. 1420 nm corresponding to the $^3F_4 \rightarrow ^3H_4$ transition.

3.3.1   "*Pump-and-probe*" measurement method

The standard technique for ESA measurements is the so-called *"pump-and-probe"* method, setup of which is given in figure 3.7.
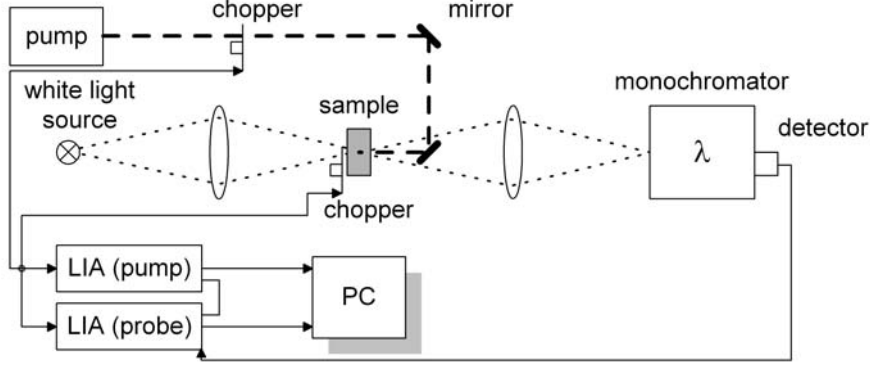
Figure 3.7: Setup of the standard "pump-and-probe" method

It consists of the pump path (in figure shown as dashed line) and probe path, for which the radiation is obtained using the white light source. The pump radiation has to be chopped in order to change the excitation of the thulium ions in the glass sample. As next the mirrors and optics are used to focus the radiation on the sample to be measured. The probe beam of the white light source is also chopped to trigger the lock-in amplifier (LIA) and further imaged on the entrance slit of the monochromator. It is worth noting that both paths should enter the glass sample perpendicularly and they have to be focused in one point. In the setup shown in figure 3.7 the probe path travels from left to the right whereas the pump radiation in the middle of the sample coming from its top-side. One of the lock-in amplifiers is synchronized with the frequency f_p and measures the intensity of the transmitted probe beam I; the second LIA amplifies the difference between measured intensities for the pumped and unpumped case (ΔI). Due to decreasing rare-earth ions population in the ground state, which occurs when the sample is pumped, the transmission I increases compared to the unpumped case. The population of the excited sates can lead to increase in the probe intensity for the wavelength regions with stimulated emission (SE) and/or to its decreasing for wavelengths where excited state absorption is not negligible. The measured $\Delta I/I$ ratio is proportional to the cross-sections

$$\frac{\Delta I}{I} \propto \sigma_{GSA} + \sum_i n_i(\sigma_{SE,i} - \sigma_{ESA,i}) \ , \tag{3.15}$$

where n_i is the relative population of level i. The absorption cross-section σ_{GSA} is first used to calibrate the measured $\Delta I/I$ spectrum and then subtracted from the measurement. The

remaining part of the spectrum consists of lines corresponding to the stimulated emissions and excited-state absorption, but in order to calculate the absolute cross-sections, the population of all relevant levels is required. Because of drawback of this measurement method (necessity to precise adjustment pump and probe paths to assure their overlap) it is difficult to preform quantitative measurements. The power density in the glass sample is difficult to estimate and the population of the excited levels can not be estimated precisely, which is the main disadvantage of this method. This problem can be avoided, when the measurements are performed in fibers, as reported in [96] or described the following.

3.3.2 Modified measurement method

Since for the TDFA modelling the absorptions from first excited state are significant a "pump-and-probe" technique may be used with a high-power laser at around 1900 nm, which populates only the first excited state. It was reported that such a laser is able to deliver up to 2.7 W continuous wave [97], but it is not commercially available and much too complicated to realize just for the ESA measurements. As mentioned in a previous section, standard measurement method has to be done for bulk glass and it delivers limited information about ESA. It does not allow to recalculate the measurement data into cross-sections commonly used for amplifier simulation. Therefore the measurements presented here were performed for fiber samples, what gives the possibility to calculate the population of $^3H_6$ and $^3F_4$ levels, which are needed to transform the measurement data into ESA cross-sections [98].

The experiments described in this work were performed using the setup presented in figure 3.8, which uses a standard fiber attenuation measurement system (S25, York) and parts from the TDFA setup in form of a short piece of the active fiber, a pump coupler and a pigtailed pump diode at 805 nm.

The measurement system consists of a white light source, the radiation of which is chopped with a constant frequency and launched into the test device (DUT) [98]. The same frequency is applied to the lock-in amplifier (LIA) used for the detection of the radiation leaving the characterized structure. The test device contains a piece of TDF, two HNA interface fibers and a pump coupler at one side to couple the pump radiation from a pigtailed single mode laser diode into the thulium-doped fiber. In order to suppress cladding modes, cladding mode filters were used at the input and output port of the S25. A long-pass filter in front of the detector suppressed the pump power reflected from the glue-splice.

For the experiments done here, samples containing self-made fibers based on zirconium fluoride were used. The fiber's core composition was:

$$53ZrF_4 - 16BaF_2 - 3.375LaF_3 - 3AlF_3 - 20NaF - 4PbF_2 - 0.125InF_3 - 0.5TmF_3$$
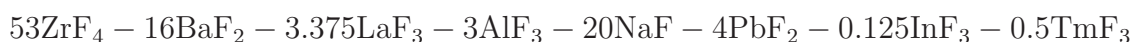
and for the cladding a HZBLAN glass with the composition

$$43HfF_4 - 10ZrF_4 - 18.875BaF_2 - 3.5LaF_3 - 2.5AlF_3 - 22NaF - 0.125InF_3$$
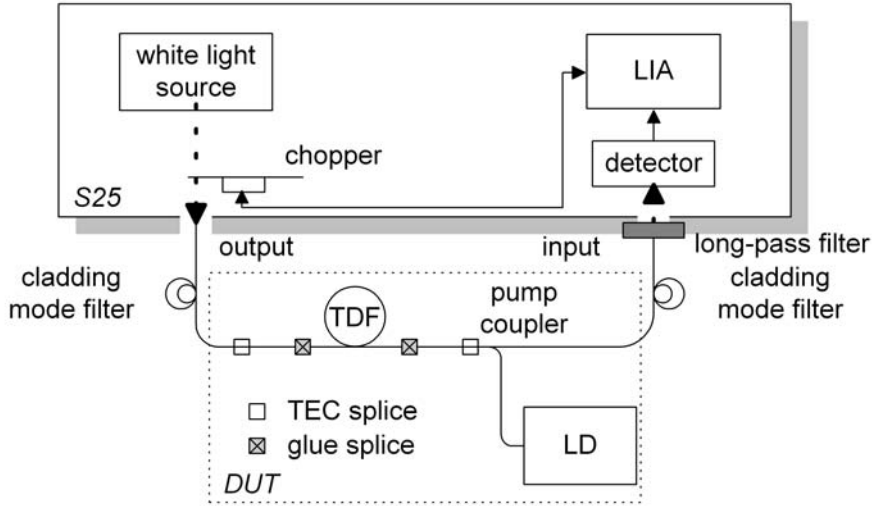
Figure 3.8: Setup of the modified "pump-and-probe" method used for ESA measurements

was used. The fiber had a core diameter of $3\,\mu$m and a numerical aperture of 0.25. For the experiment, three test devices containing thulium-doped fibers with lengths of 1.5, 1.7 and 3 cm were used. Since the fiber optic part of the setup consisted of standard silica fiber (SMF-28, Corning), optimized silica fibers with high numerical aperture (HNA fibers) was used to minimize the mode field diameter mismatch between fluoride and silica fibers. The connection between SMF-28 and HNA fibers was realized as a thermally-diffused expanded core (TEC splice) - see detailed description in chapter 5.2. Silica and fluoride fibers were joined using glue-splices.

The measurement procedure consists of three steps: as first the background spectrum without thulium-doped fiber and HNA fibers, but with WDM coupler (P_A) was measured. Afterwards two spectra with TDF were recorded, one unpumped (P_B) and one with the pump diode switched on (P_C). As an example, the measured spectra for 3 cm long fiber were shown in figure 3.9.

Comparing P_B and P_C spectra one can clearly distinguish changes in the absorption in three bands: first centered at around 1050 nm, which corresponds to ${}^3F_4 \rightarrow {}^3F_{3,2}$ excited-state absorption, second at 1210 nm, which represents ${}^3H_4 \rightarrow {}^3H_5$ ground state absorption and third at approx. 1420 nm which is contributed to ESA from ${}^3F_4$ to ${}^3H_4$ level.

Similarly to the cut-back measurement method, used to find the fiber attenuation, it is very important that all measurements A-C for each sample were carried out without modifying the incoupling conditions, which means that the fiber at the output of the S25 must never be touched. The short lengths of the thulium-doped fiber were chosen in order to observe GSA
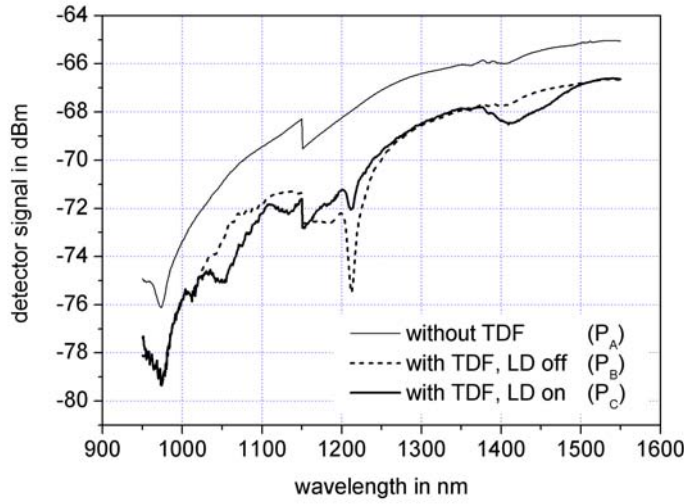
Figure 3.9: Attenuation spectra for 3 cm long TDF used for ESA cross-section calculations

and ESA simultaneously. For longer fibers, the ground state absorption at approx. 1210 nm, which was used for gathering the information about the population of the $^3F_4$ level and scaling the ESA spectra, became too large to be measured.

3.3.3 Analysis of the measured spectra

The experiment has some similarities with the cut-back method used to determine the attenuation of the fiber. Therefore its evaluation occurs in the same way. Three main types of attenuation are present in the test device.

(a) **The transmission spectrum of the pump coupler**, which is wavelength dependent, but it is contained in all three measurements and it cancels out when the quotients

$$\beta_1 = P_B/P_A \tag{3.16}$$

and

$$\beta_2 = P_C/P_A \tag{3.17}$$

are calculated.

(b) **The losses of the fluoride fiber, TECs and glue-splices**, are contained only in P_B and P_C. These losses can only be roughly estimated to be in the order of 3 dB in total, but anyway it seems to be reasonable to treat them as being constant or only slightly

varying factors in the wavelength range of each ESA line, which cause only shift of the baseline.

(c) **The thulium absorption in the TDF**, which is defined as:

$$\alpha_B = \log P_A/P_B - \alpha_{base} \ , \tag{3.18}$$

and

$$\alpha_C = \log P_A/P_C - \alpha_{base} \ . \tag{3.19}$$

The cross-section of the ground state absorption derived from measurement performed for unpumped TDF is given by:

$$\sigma_{GSA} = \frac{\alpha_B}{c_I l} \ , \tag{3.20}$$

where c_I is the thulium ion density and l is the length of the thulium-doped fiber. In the case of the measurement with the laser diode switched on, the cross-sections of the ground state and the excited state absorption are:

$$\sigma_{GSA} = \frac{\alpha_C}{n_0 c_I l} \ , \tag{3.21}$$

$$\sigma_{ESA} = \frac{\alpha_C}{n_1 c_I l} \ , \tag{3.22}$$

where n_0 and n_1 are the relative population numbers of the ground and the first excited state, respectively. The population of the ground state in thulium was obtained from the comparison of the attenuation measurements with and without pump radiation at the GSA line around 1210 nm. It is given by:

$$n_0 = \frac{\alpha_C \ @ \ 1210\,\mathrm{nm}}{\alpha_B \ @ \ 1210\,\mathrm{nm}} = 0.28 \pm 0.05 \ , \tag{3.23}$$

and its graphical representation is shown in figure 3.10.

This equation is valid for the laser materials doped with rare-earth ions, for which the absorption does not depend on the pump conditions, which is not the case in semiconductors. The active medium here consists of a group of independent and localized rare-earth ions and the absorption probability of an individual ion is always the same, regardless whether the other ions are in excited states or not.

The population of the first excited level is more difficult to calculate, nevertheless it was calculated by solving the set of equilibrium rate equations for the lowest 4 energy levels of Tm^{3+}. Since the fibers were short and the pump absorption was very low (approx. 2.5 %),
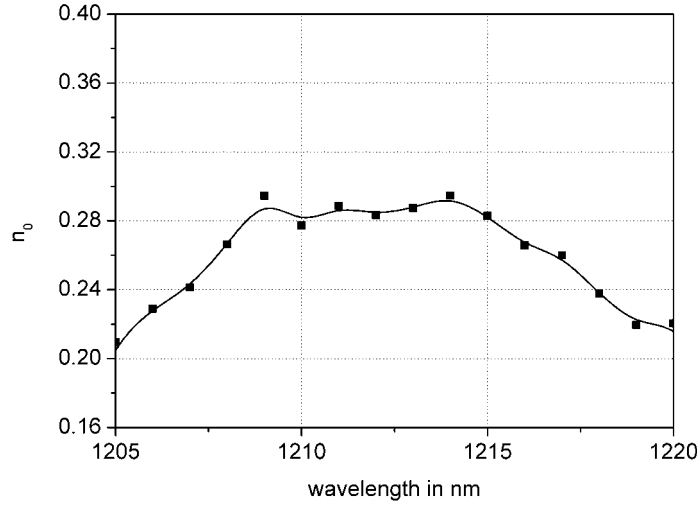
Figure 3.10: Population of the ground state gained from the comparison of the GSA in pumped and non-pumped state

this allowed to treat the whole length of fiber as one segment and use just one system of rate equations for its full description in the steady state:

$$W_p n_0 - \left(\frac{1}{\tau_3} + W_{32} + X_{30} \right) n_3 = \frac{dn_3}{dt} = 0 \; , \qquad (3.24)$$

$$\left(\frac{\beta_{32}}{\tau_3} + W_{32} \right) n_3 - \left(\frac{1}{\tau_2} + W_{21} \right) n_2 = \frac{dn_2}{dt} = 0 \; , \qquad (3.25)$$

$$\frac{\beta_{31}}{\tau_3} n_3 + \left(\frac{\beta_{21}}{\tau_2} + W_{21} \right) n_2 - \left(\frac{1}{\tau_1} + W_{10} + X_{10} \right) n_1 = \frac{dn_1}{dt} = 0 \; , \qquad (3.26)$$

$$n_0 + n_1 + n_2 + n_3 = 1 \; , \qquad (3.27)$$

where W_p is the pump rate, n_i is the relative population number of energy level i, τ_i is the radiative lifetime of level i, W_{ij} is a non-radiative multi-phonon emission rate, and β_{ij} is the branching ratio for the radiative spontaneous transition from level i to j. The quenching effect in highly-doped glasses leads to losses X_{ij} mainly to the ground state $j = 0$. The population of the lower amplification level ($^3\mathrm{F}_4$) can be found by solving equations (3.24) to (3.27). The solution is:

$$n_1 = C_1(1 - n_0) \; , \qquad (3.28)$$

with

$$C_1 = \frac{1}{1 + \frac{(1/\tau_2 + W_{21} + \beta_{32}/\tau_3 + W_{31})(1/\tau_1 + W_{10} + X_{10})}{\beta_{31}/\tau_3(1/\tau_2 + W_{21}) + (\beta_{32}/\tau_3 + W_{32})(\beta_{21}/\tau_2 + W_{21})}} \ . \tag{3.29}$$

Equation (3.28) is valid not only for the first, but also for every excited state, each with a different constant C_i. Since $1 - n_0$ is the fraction for all excited states, the equation means that the distribution of the population numbers across the excited states, relative to the total population number of all excited states, does not depend on the pump power. It is fixed by the branching ratios and lifetimes of the energy levels, as long as stimulated emission or excited state absorption processes do not affect the population numbers significantly. Not all of the parameters needed for solving the equation (3.29) can be measured, especially the multi-phonon losses are difficult to obtain. To get at least estimated values, one can use the equation:

$$W_{ij} = C \exp{-\alpha \Delta k_{ij}} \ , \tag{3.30}$$

with the constant C equals to $1.99 \cdot 10^5 \, \mathrm{s}^{-1}$ and α as big as $2.11 \cdot 10^{-3} \, \mathrm{cm}$ [77] and the level distance Δk_{ij}. The accuracy of such a calculation is poor, but it turns out, that the rates W_{10} and W_{32} are very small and W_{21} cancels out almost completely in equation (3.29). The branching ratios are calculated based on energy level and Judd-Ofelt calculations [58]. Most important are the radiative lifetimes and the quenching losses which have been measured in glasses with different dopant concentrations (see section 3.5). All parameters needed to calculate the constant C_1 are listed in table 3.9.

Using these parameters to solve equation (3.29) leads to a constant C_1 equal to 0.58 and the relative population number n_1 of 0.42. The resulting ESA cross-section spectrum for the 3 cm fiber is shown in figure 3.11.

The peak values for ${}^3\mathrm{F}_4 \rightarrow {}^3\mathrm{F}_{3,2}$ and ${}^3\mathrm{F}_4 \rightarrow {}^3\mathrm{H}_4$ were found to be centered at 1056 nm and 1422 nm, respectively, in agreement with calculated wavelengths of the ESA transitions [58]. The bandwidths of the transitions were estimated as 41 nm and 80 nm, which makes the choice of the second pump wavelength less critical. For the efficient pumping the laser diode wavelength's tolerance is therefore about $\pm$ 10 nm.

The spectra for all samples measured in this experiment agreed with each other with about $\pm \, 0.05 \, \mathrm{pm}^2$ accuracy. The uncertainty originating from the parameters collected in table 3.9, however, can be expected to be much larger.

3.3.4   Comparison with the literature

Among a couple of publications which contain ESA parameters of thulium in zirconium-fluoride based glasses only some of them [87, 96, 99] show quantitative spectra which may be

Table 3.9: Parameters needed to estimate the C_1 constant and solve the rate equations

parameter	value	type	reference
Δk_{10}	$5862\,\mathrm{cm}^{-1}$	measured	[58]
Δk_{21}	$2026\,\mathrm{cm}^{-1}$	measured	[58]
Δk_{32}	$4010\,\mathrm{cm}^{-1}$	measured	[58]
W_{10}	$0\,\mathrm{s}^{-1}$	estimated	here
W_{21}	$2769\,\mathrm{s}^-1$	estimated	here
W_{32}	$42\,\mathrm{s}^{-1}$	estimated	here
$1/\tau_1$	$94.3\,\mathrm{s}^{-1}$	measured	[67]
$1/\tau_2$	$177\,\mathrm{s}^{-1}$	calculated	[58]
$1/\tau_3$	$781.3\,\mathrm{s}^{-1}$	measured	[67]
X_{10}	$5.8\,\mathrm{s}^{-1}$	measured	[67]
X_{30}	$168.9\,\mathrm{s}^{-1}$	measured	[67]
β_{32}	0.033	calculated	[58]
β_{31}	0.097	calculated	[58]
β_{21}	0.018	calculated	[58]
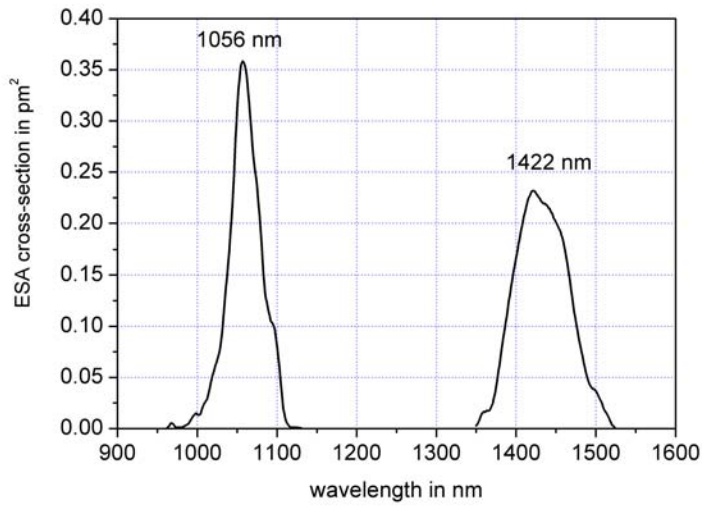
Figure 3.11: Excited-state absorption spectra for $3\,\mathrm{cm}$ long TDF

compared to the results shown here.

Similar to the ground state absorption, oscillator strengths were calculated according to equation (3.14), but since spectra were measured in wavelength domain, the oscillator strengths were calculated by:

$$f = \frac{4\varepsilon_0 m_e c^2}{e^2 \lambda_0^2} \int \sigma_{ESA}(\lambda) \, d\lambda \, , \tag{3.31}$$

with the peak wavelength λ_0. Table 3.10 summarizes the mean peak values, together with the oscillator strengths and literature values for comparison.

Table 3.10: Peak cross-sections and oscillator strengths of the excited state absorption lines

ESA transition	$\sigma_{ESA} \pm \Delta\sigma_{ESA}$ in pm^2	f in 10^{-8}	comment	reference
	0.358 ± 0.05	172	ZBLAN/m.	here
$^3F_4 \rightarrow {}^3F_{2,3}$	0.22	132[a]	ZBLAN/c.	[87]
	n.a	197.1	ZBLAN/c.	[58]
	0.2	105.1[a]	ZBLAN/m.	[96]
(approx. 1050 nm)	0.4	208.9[a]	SiO$_2$/m.	[89]
	0.230 ± 0.05	112	ZBLAN/m.	here
$^3F_4 \rightarrow {}^3H_4$	0.17	94[a]	ZBLAN/c.	[87]
	0.145	81[a]	ZBLAN/m.	[96]
	0.181	90.3	ZBLAN/m.	[99]
(approx. 1420 nm)	n.a	101.5	ZBLAN/c.	[58]

Notes:
[a] recalculated integrals from published spectra,
n.a. - not available,
m. - measurement,
c. - calculation

The measured cross-sections are in a good agreement with the values published in the literature, with respect to the measurement and calculation accuracy. The references give only measured or calculated values but do not clarify their accuracy. Since the calculations base on the Judd-Ofelt theory including simplifying assumptions [65, 66], large differences compared to measured values are not surprising. However, all deviations stay generally below 25 %, which is usual for such comparisons between measurements and calculations [58]. Much larger discrepancies between ours results and that published in [96] are rather difficult to explain only due to the measurement errors. However the experimental procedure used by S. Guy assumes, that after 10 ms, when the pump radiation is blocked by chopper the population of $^3H_4$ level completely decrease (due to its lifetime of approx. 1 ms) while the population of $^3F_4$ level stays almost constant. This assumption is in principle correct, but on this way one

loses the information about the real population of both important energy levels, which can lead to an inaccurate calibration of the ESA cross-sections.

3.4   Emission

For the amplifier modelling several emission lines are of great importance. They start from levels ${}^3H_4$, ${}^3H_5$ and ${}^3F_4$ and influence the amplifier performance. However, to predict the amplification bandwidth the transition ${}^3H_4 \rightarrow {}^3F_4$ plays an principle role.

Since the absorption and emission processes in the laser medium are linked by the equations (2.4) and (2.5), the absorption cross-section can be used to calculate appropriate emission cross-section using the McCumber theory. It assumes that the position and occupation probability of each Stark level is described by Boltzmann statistics [100] and leads to following equation:

$$\sigma_{21}(\nu) = \sigma_{12}(\nu)e^{(h\nu - \overline{\Delta E})/k_B T} \ , \tag{3.32}$$

where $\overline{\Delta E}$ is the energy needed to excite the ion from the Stark level 1 to level 2, k_B is Boltzmann's constant, and T the temperature. In practice, the emission lines can be measured easily, which is not always the case for the absorption (especially ESA). Therefore for its estimation the McCumber theory is used, but since the excited-state absorptions, which are relevant for the amplifier performance can be measured there is no necessary to calculate them. Moreover, as discussed in [58], the results of McCumber calculations do not fully agree with the measurement, the calculated values are often under- or over-estimated. This is also the case in thulium as it is shown in figure 3.12. Due to the large discrepancies between measurement and calculation we decide to use measurement data, which are comparable with the literature.

3.4.1   Measurement setup and procedure

The setup used for measurements of the fluorescence spectra, described in details in [58], is shown in figure 3.13. The pump beam with a power of $400\,\mathrm{mW}$ emitted by the laser diode operating at 800 nm was focused on the center of the glass sample by using the lens set L_p. The fluorescence beam was focused on the entrance slit of the monochromator (PTI) by the lens set L_1. Because of the fact, that fluorescence radiation propagates bi-directionally, the part of it, which is propagating in opposite direction was reflected with the spherical mirror. Before entering the monochromator, the beam was chopped to synchronize the lock-in amplifier (LIA). On the other side a long-pass filter has been used to eliminate the high diffraction orders of the monochromator grating. A second lens set L_2, (inverse to L_1), was used to image the exit slit of the monochromator onto the combined liquid nitrogen cooled Si/InSb detector. The detected signal was then amplified by transimpedance amplifier and finally measured with lock-in amplifier. The silica detector was used to measure the fluorescence
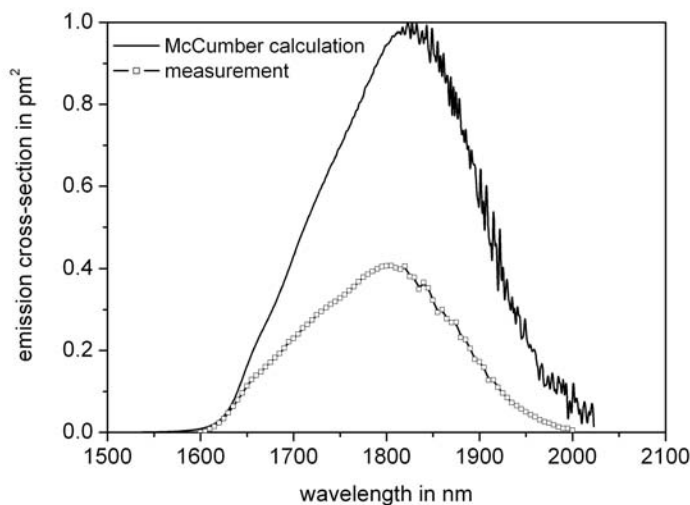
Figure 3.12: Comparison between measured and calculated emission cross section for transition $^3F_4 \rightarrow ^3H_6$
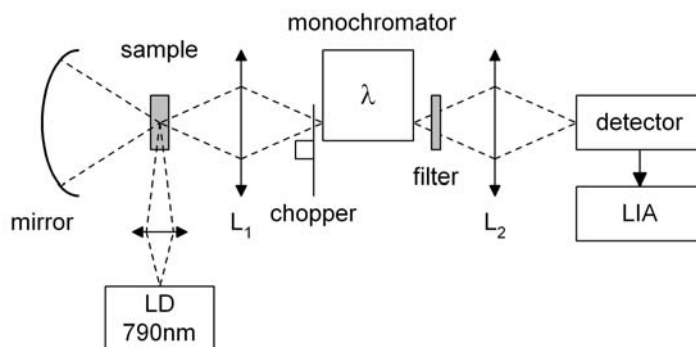
Figure 3.13: Setup of the emission spectrometer

lines up to $1\,\mu$m, above this wavelength, InSb detector was used. During the measurements two different gratings were used with respect to their operating region defined by their Blaze wavelength. This parameter defines the wavelength in a given refractive order for which the diffracted beam reaches its maximum intensity, which means the highest sensitivity of the grating. The gratings used for the measurements have the effective Blaze wavelengths of $1.1\,\mu$m and $2.6\,\mu$m, which made possible to cover the whole interesting measurement range.

For each ZBLAN and IBZP glass sample at least three fluorescence spectra were measured

in order to minimize the uncertainties caused by measurement errors. The fluorescence spectra were measured at the room temperature.

3.4.2   Analysis of measured spectra

In the first step the baseline of the fluorescence spectra was determined similar to the absorption transitions. Comparing them to absorption measurements, where the baseline correction was very important, here only an external light source can cause some measurement errors. Therefore all the measurements were performed in dark room with the integration time of lock-in amplifier in the region of 3 - 10 seconds. The measurement took several minutes to some hours, but the noise level recorded together with the measurement was kept low. Since the emission lines are far from each other, they did not overlap, which made the baseline correction even more simple. Some difficulties were found to measure the $^3H_4 \rightarrow {}^3H_6$ transition centered at approx. 800 nm, which is very close to the pump wavelength. In order to separate strong pump and weaker fluorescence peak the pump diode was cooled down to 5 °C which shifted its wavelength to 787 nm. After that, the pump peak was fitted with the gaussian curve and subtracted from the whole measured spectrum. Cooling down of the pump diode caused also decrease in the emitted fluorescence, but its shape, which is used for further calculation, stayed constant.

The emission cross-section spectra were calculated using the measured fluorescence spectra and the modified Fuchtbauer-Ladenburg equation [101]:

$$\sigma_{EM} = \frac{1}{8\pi c k_p^2 n^2} A_{21} g_{21}(k) \ , \tag{3.33}$$

where $g_{21}(k)$ is the measured fluorescence lineshape, which is normalized using the following equation:

$$\int g_{21}(k)dk = 1 \ , \tag{3.34}$$

k_p is the wavenumber of the absorption peak, c the speed of light in vacuum, and n the refractive index of the glass, which was measured for ZBLAN as well as for IBZP glasses as described in section 3.1. A_{21} is the radiative spontaneous emission rate based on the results of the energy level and Judd-Ofelt calculations [58, 67]. Four radiative transitions have been measured with the IBZP and five with the ZBLAN glass samples. The results are shown in figure 3.14 and collected in table 3.11.

The values in the table are given together with their accuracy, which similarly to the GSA and ESA cross-sections were calculated as standard error of the mean value, but since the deviations are very small they were not shown in figure 3.14.
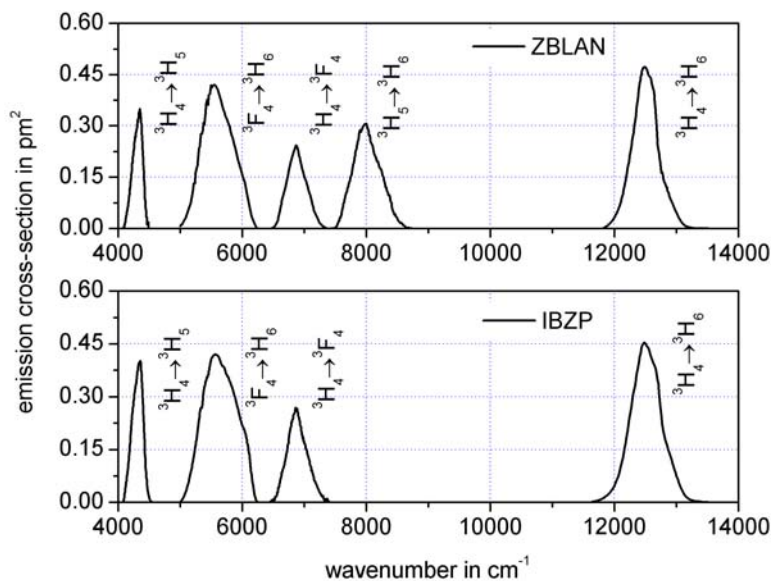
Figure 3.14: Emission cross-sections for ZBLAN and IBZP glasses

The analysis of the emission cross-sections shows that both glass types have comparable properties. It is easy to see that the emission maxima are almost the same for both hosts. Nevertheless, it was impossible to detect the relatively weak $^3H_5\rightarrow{}^3H_6$ transition in IBZP, although this transition was clearly observed in ZBLAN and the calculations performed in [67] show that the emission rate for this transition is slightly larger in IBZP than in ZBLAN.

The emission cross-section of the $^3H_4\rightarrow{}^3F_4$ transition, which is about 17 % larger in the indium fluoride glass is of interest when using it as host glass for TDFA. However, the competitive $^3H_4\rightarrow{}^3H_5$ transition, which starts from the same energy level is also stronger by nearly the same factor, since the calculated branching ratios of these transitions are very similar for both glasses.

3.4.3   Comparison with the literature

As emission cross-sections shown in literature are mostly given in arbitrary units, a comparison of results is often not possible. However, some values of the emission cross-section for the $^3H_4\rightarrow{}^3F_4$ transitions in different host glasses are collected in table 3.12 together with the results obtained by the author.

Table 3.11: Measured emission cross-sections for thulium in ZBLAN and IBZP

transition	ZBLAN			IBZP		
	k_p in cm^{-1}	λ_p in nm	$\overline{\sigma}_{EM} \pm \Delta\sigma_{EM}$ in pm^2	k_p in cm^{-1}	λ_p in nm	$\overline{\sigma}_{EM} \pm \Delta\sigma_{EM}$ in pm^2
$^3H_4 \rightarrow {}^3H_5$	4346.88	2300.50	0.346 ± 0.014	4356.92	2295.20	0.396 ± 0.007
$^3F_4 \rightarrow {}^3H_6$	5567.23	1796.25	0.404 ± 0.015	5569.56	1795.50	0.413 ± 0.003
$^3H_4 \rightarrow {}^3F_4$	6871.44	1455.30	0.238 ± 0.008	6868.81	1455.85	0.282 ± 0.009
$^3H_5 \rightarrow {}^3H_6$	7992.33	1251.20	0.300 ± 0.006	not measured		
$^3H_4 \rightarrow {}^3H_6$	12483.60	801.05	0.458± 0.031	12473.51	801.70	0.450 ± 0.002

Table 3.12: Emission peak cross-sections for thulium $^3H_4 \rightarrow {}^3F_4$ transition line in different host glasses

glass	λ_p in nm	σ_{EM} in pm^2	ref.
ZBLAN	1455.30	0.238± 0.008	here
ZBLAN	1455.5	0.233 ± 0.004	[58]
ZBLAN	1452	0.230	[102]
IBZP	1455.85	0.282 ± 0.009	here
TNZ[a]	1458	0.450	[102]
SiO$_2$	1440	0.166	[103]
SiSb[b]	1463	0.362	[104]
GeGaCa[c]	1471	0.242	[104]
TZN[d]	1476	0.310	[104]
BPG[e]	1483	0.274	[104]

Glass compositions:
[a] $80TeO_2 - 10Na_2O - 9ZnO$,
[b] $76SiO_2 - 20Sb_2O_3$,
[c] $70GeO_2 - 14Ga_2O_3 - 8CaO$,
[d] $70TeO_2 - 20ZnO - 10Na_2O$,
[e] $20Bi_2O_3 - 60PbO - 20Ga_2O_3$,

The values in the table differs by about 4 % for ZBLAN glass samples and the peak wavelength of the considered fluorescence line keeps almost constant. Nevertheless, a significant shift towards longer wavelengths in the fluorescence maxima for different oxide glasses can be seen, which is somehow surprising in respect of the fact, that the emission properties of rare-earth ions do not depend much on the host material. However, the wavelength shift of almost 43 nm seems to be significant regarding the approaches to shift the amplification region of the thulium-doped fiber amplifier towards longer wavelengths. Unfortunately, all the glass compositions given in [104] show higher phonon energies and their better properties comparing to fluoride glasses can not be effectively used for the amplifier. The tellurite glasses

described in [102, 104] show better fluorescence properties and due to their low phonon energy ($\sim 750\,\mathrm{cm}^{-1}$) can compete with fluoride glasses, but the high refractive index hinder their joining to the silica glass as it was described in the chapter 5.1.

3.5   Lifetime measurements

Due to the fact, that for every excited energy level radiative transitions, multiphonon relaxations and energy transfer occur simultaneously, the total lifetime is given by:

$$\tau = \frac{1}{A_{rad} + W_{mp} + W_{et}} \; , \tag{3.35}$$

where A_{rad} and W_{mp} are the radiative relaxation and multiphonon transition rates respectively. The W_{et} represents the energy transfer processes. For low dopant concentrations the energy transfer rates in the first assumption are low and constant. On the other hand, the large energy gaps between the energy levels result in negligible multiphonon relaxations rates. Therefore the measured lifetime of the level is in fact the radiative lifetime τ_{rad}. The multiphonon relaxation is a temperature dependent process, which is weaker in fluoride glasses than in silica due to the low phonon energies. Energy transfer plays only an important role in case of glasses which are highly-doped with thulium ions (as it is described in chapter 3.5.2). In the following chapters measurement setup and the results of lifetime measurement are given and compared with the literature.

3.5.1   Measurement setup and procedure

The lifetime measurements of thulium-doped ZBLAN and IBZP glasses were performed using the modified setup used for emission spectroscopy. The modified setup is shown in figure 3.15.
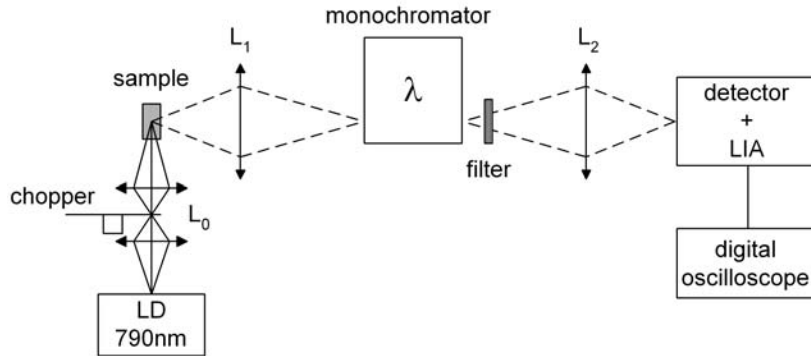
Figure 3.15: Setup used for lifetime measurements

The main difference compared to the previously used setup is in the position of the chopper. It has been moved to the front of the sample to modulate the pump signal and therefore the excitation. The pump absorption populates the $^3H_4$ level and indirectly, by the fast radiative transitions at 2300 and 1470 nm, also the $^3H_5$ and $^3F_4$ levels. For the measurement it is of general importance to take care of the chopper frequency and the spot size of the pumping beam in the place, where it is chopped. In order to minimize the uncertainty caused by the time needed to cut the pump beam, the lens set L_0 was introduced into the setup. During the measurement, the decay curves of the fluorescence were measured at least 3 times for each glass probe and stored using a digital oscilloscope. The multiple measurement procedure, as applied also for absorption and emission measurements, minimizes the probability of an systematic error and was used to obtain the average decay curves for each sample. As a next step, an exponential fit was applied to the measurement curves to obtain the value of the lifetime.

A typical decay curves for levels $^3H_4$ and $^3F_4$ level obtained by measuring the emitted radiation at maximum of $^3H_4{\rightarrow}^3F_4$ and $^3F_4{\rightarrow}^3H_6$ emission lines respectively are shown in figure 3.16. The results of the exponential fit are also given.
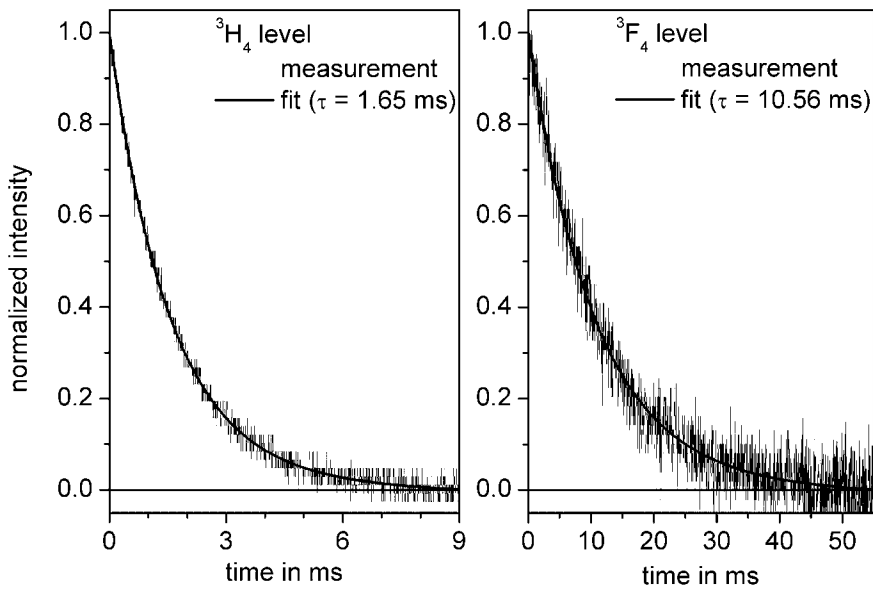
Figure 3.16: Decay curves for levels $^3H_4$ (left, sample I6) and $^3F_4$ (right, sample Z3)

The measurement results include noise, which is much higher for the weak emission from

the $^3F_4$ level centered at approx. 1800 nm as it is shown in previous figure. Nevertheless, the measurement and its fit agree very well. In order to assure the proper fit condition one should be able to observe the total decline of the measurement curve, from which the maximum chopper frequency can be determined. For the chopper blades used in this measurement it was found that the maximal frequency, which allows to record the signal decline over the quadruple of the measured lifetimes was about 55 and 11 Hz for transitions from $^3H_4$ and $^3F_4$ level respectively.

To investigate the energy transfer processes in fluoride glasses the lifetime measurements were performed for glasses with different thulium concentrations. It is obvious, that energy transfer becomes significant with increasing dopant concentration, and this phenomenon is discussed in more details in the following section.

3.5.2   Concentration quenching

The energy transfer processes, which are negligible in glasses with low rare-earth ion concentration become more important above a certain dopant ion density. The interactions between two dopant ions were thoroughly investigated for highly-doped amplifier or laser media [60, 105]. It was found, that they are caused by dipole-dipole coupling and two main types of energy transfer processes can be distinguished. One of them is resonant energy transfer between ions of the same dopant and another one is cross-relaxation between different dopants, which is used for example for pumping of erbium-ytterbium-doped amplifiers [106]. Since the glass samples investigated here were singly doped with thulium ions, only the first process can be observed and its main consequence is concentration quenching. Increasing the dopant concentration leads to clustering, which was observed for silica glasses doped with rare-earth ions [60], and the critical dopant concentration was found to be energy level dependent. For erbium-doped fiber amplifiers this critical concentration is larger than 1000 ppm [60]. Above this value the distance between dopant ions is lower than its critical value, which is achieved when the condition

$$W_{et} = A_{rad} + W_{mp} \tag{3.36}$$

is satisfied.

The critical dopant concentration in fluoride based glasses is expected to be higher than for silica glass, where rare-earth ions are introduced into the glass matrix and they fill its empty spaces. In the case of fluoride glasses, rare-earths are part of the glass composition due to the substitution of LaF_3 by TmF_3. However, when the dopant concentration is high enough, which means that the ions are close to each other, the energy transfer occurs and it is very efficient. Since the cross-relaxation plays an important role in TDFA pumped at 1056nm, this problem was systematically investigated and the results are reported in section 7.2.

Thulium concentration in the investigated glass samples varied from 0.01 to $3\,\text{mol}\%$. Afterwards, the lifetimes measured for the two transitions $^3\text{H}_4{\rightarrow}^3\text{F}_4$ and $^3\text{F}_4{\rightarrow}^3\text{H}_6$ have been fitted using the function

$$\tau_i = \frac{1}{a + bc_{Tm}} \ , \tag{3.37}$$

where τ_i is the lifetime of the ith energy level, a and b are fit parameters, and c_{Tm} is the TmF_3 fraction [107].

The measurement results are shown in figures 3.17 and 3.18 and summarized in table 3.13. Also in this case the measurement data are given with their accuracy calculated as standard error of the mean value.
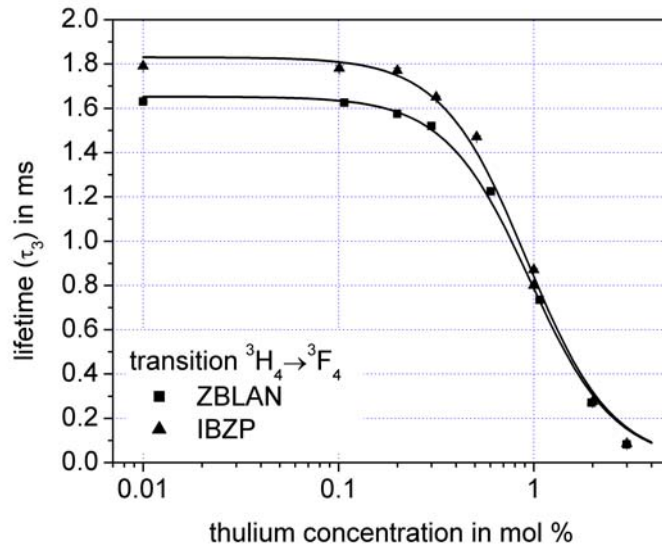
Figure 3.17: Lifetime of the $^3\text{H}_4$ level as a function of the thulium concentration in ZBLAN and IBZP glasses

The measured lifetimes in both glasses show similar characteristics. As expected, the measured lifetime, which is the result of the radiative, non-radiative and energy transfer processes, is larger in IBZP compared to ZBLAN, due to the difference in the multiphonon energies of both glass types. The difference in the lifetimes for the $^3\text{H}_4$ is relatively small (up to $10\,\%$), but the lifetimes of the $^3\text{F}_4$ level differ from each other by about $20\,\%$. The influence of the energy transfer can be observed for higher concentrations, which is clearly seen in figures 3.17 and 3.18 in form of decay of the measurement curve. Because of the high thulium concentra-
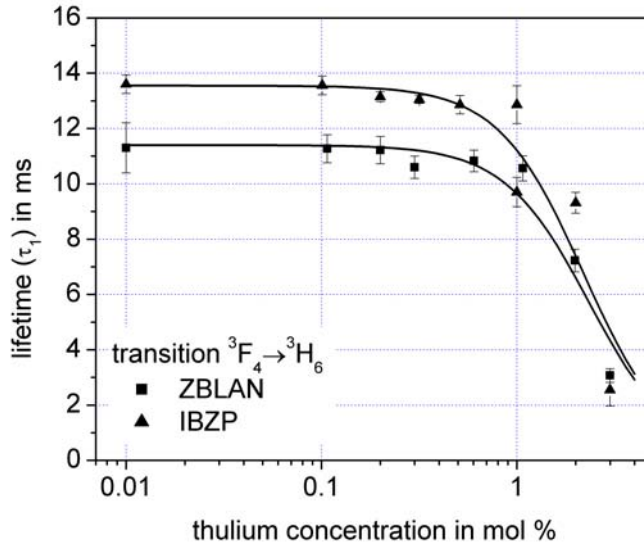
Figure 3.18: Lifetime of the $^3F_4$ level as a function of the thulium concentration in ZBLAN and IBZP glasses

tion, the dipole-dipole interactions depending on the distance between the dopant ions in the host glass become significant which leads to a shortening of the lifetimes. The critical dopant concentration, defined as 10 % reduction of the lifetime, was found to be approx. 0.3 mol% and 0.7 mol% for the $^3H_4$ and $^3F_4$ level respectively.

Since the signal of the $^3F_4 \rightarrow ^3H_6$ transition was much weaker than $^3H_4 \rightarrow ^3F_4$, it was more difficult to measure it, which is the reason of the large deviations in the measurements. It is also not clear why the lifetime τ_1 for two IBZP samples containing 1.001 mol% Tm^{3+} differed so significantly. We concluded that the thulium concentration calculated from the initial weights of the fluorides contained unknown uncertainties due to variations in the glass melting process, which led to different thulium concentration in the sample than expected.

3.5.3　Comparison with the literature

The total lifetime of the energy levels is one of the parameters, characterizing the host-dopant system. For a low dopant concentration it is determined by the radiative lifetime. However, for higher concentrations the energy transfer processes and multiphonon relaxation strongly influence the total lifetime leading to its shortening. Therefore the comparison between the measured lifetimes and that reported in the literature has to be done for similar Tm^{3+} concentrations.

Table 3.13: Measured lifetimes of Tm^{3+} in ZBLAN and IBZP glasses

	ZBLAN				IBZP		
#	c_{Tm} in mol%	$\tau_3 \pm \Delta\tau_3$ in ms	$\tau_1 \pm \Delta\tau_1$ in ms	#	c_{Tm} in mol%	$\tau_3 \pm \Delta\tau_3$ in ms	$\tau_1 \pm \Delta\tau_1$ in ms
Z1	2.992	0.082 ± 0.005	3.07 ± 0.25	I1	2.998	0.085 ± 0.003	2.55 ± 0.58
Z2	1.980	0.270 ± 0.003	7.23 ± 0.41	I2	2.000	0.275 ± 0.003	9.32 ± 0.38
Z3	1.074	0.735 ± 0.009	10.56 ± 0.46	I3	1.001	0.870 ± 0.006	12.86 ± 0.53
Z4	0.603	1.225 ± 0.009	10.83 ± 0.39	I4	1.001	0.800 ± 0.006	9.70 ± 0.68
Z5	0.300	1.520 ± 0.001	10.60 ± 0.40	I5	0.511	1.470 ± 0.006	12.86 ± 0.33
Z6	0.200	1.575 ± 0.003	11.22 ± 0.49	I6	0.317	1.650 ± 0.006	13.05 ± 0.15
Z7	0.107	1.625 ± 0.003	11.27 ± 0.50	I7	0.200	1.770 ± 0.012	13.15 ± 0.18
Z8	0.010	1.630 ± 0.003	11.30 ± 0.91	I8	0.101	1.780 ± 0.012	13.56 ± 0.33
				I9	0.010	1.790 ± 0.012	13.60 ± 0.33

In table 3.14 several literature values for both lifetimes τ_1 and τ_3 were compared. As a reference also calculated lifetimes are given. The comparison shows, that the measured values are in a good agreement with the literature. The differences in τ_3 for **fluoride** based glasses doped with 0.1 mol% thulium are less than 17 % whereas the values of τ_1 for the same thulium concentration differs of about 12 %. However, the lifetime τ_1 in IBZS glass is reported to be much lower than other measurement values. The discrepancy of more than 60 % can not be explained by the different glass composition only, and the authors in [76] mention the structural defects or unintentionally introduced impurities as the possible reason. Also the lifetimes in the glasses doped with 0.2 mol% of thulium agree with the literature with the discrepancies less than 23 %. For the comparison, the lifetimes in silica and tellurite based glasses are found to be much lower, and therefore their application as host glasses for TDFA seems to be less effective. Analyzing the last part of the table 3.14 it easy to conclude that the total lifetime of the weakly doped glasses, as expected, is dominated by the radiative lifetime.

3.6 Comparison of ZBLAN and IBZP as a host-glass for the TDFA

The main aim of the spectroscopic measurements described in this chapter was to gain the lifetimes of the relevant energy levels as well as the absorption and emission cross-section spectra, whose have to be used further for the TDFA simulations. The measurements were performed for two glass types, and the important question was, whether the IBZP glass is more suitable host for the thulium-doped fiber amplifier.

The most efficient TDFAs today use a GSA pump at 790 nm and an ESA pump from the

Table 3.14: Comparison of published lifetimes of Tm^{3+} in different glass hosts

glass	c_{Tm} in mol%	$\tau_3 \pm \Delta\tau_3$ in ms	$\tau_1 \pm \Delta\tau_1$ in ms	reference
ZBLAN	0.1	1.625 ± 0.003	11.27 ± 0.50	here
IBZP	0.1	1.780 ± 0.012	13.56 ± 0.33	here
BIZYT[a]	0.1	1.8	12.7	[75]
IBZS[b]	0.1	1.7	4.40	[76]
IZSB[c]	0.1	1.9	n.m.	[108]
TZC[d]	0.1	0.43	3.20	[88]
ZBLAN	0.603	1.225 ± 0.009	10.83 ± 0.39	here
IBZP	0.511	1.470 ± 0.006	12.86 ± 0.33	here
ZCBLA[e]	0.5	1.25	8.4	[109]
IBZS[b]	0.5	1.33	n.m.	[76]
TZC[d]	0.5	~ 0.40	~ 3.00	[88]
ZBLAN	cal.	1.51	11.22	[110]
ZBLAN	cal.	1.36	7.35	[58]
BZYT[f]	cal.	1.52	9.25	[111]
BIZYT[g]	cal.	1.50	9.20	[93]
SiO_2	cal.	0.69	4.56	[110]

Notes:

n.m - not measured,

cal. - calculated radiative lifetimes,

Glass compositions:

[a] $30BaF_2 - 30InF_2 - 20ZnF_3(10 - x)YF_3 - 10ThF_4 - xTmF_3$,

[b] $(36 - x)InF_3 - 16BaF_2 - 20ZnF_2 - 20SrF_2 - 6GaF_3 - 2NaF - xTmF_3$,

[c] $(40 - x)InF_3 - 20ZnF_2 - 20SrF_2 - 20BaF_2 - xTmF_3$,

[d] $60TeO_2 - 40ZnCl_2$,

[e] $32ZnF_2 - 28CdF_2 - 20BaF_2 - 11LiF - 5AlF_3 - 4LaF_3$,

[f] $19BaF_2 - 27ZnF_2 - 26YbF_3 - 27ThF_4 - xTmF_3$,

[g] $30BaF_2 - 30InF_3 - 20ZnF_2 - (10 - x)YF_3 - 10ThF_4 - xTmF_3$

first excited state of either 1050 or 1400 nm. As it was shown in tables 3.6, 3.5 and 3.4, on one hand the oscillator strength of the GSA transition to level $^3H_4$ is about 5 % larger in IBZP compared to ZBLAN, but on the other hand due to the different Stark splitting, the peak height on the other hand is about 15 % smaller.

Regarding the ESA pump transitions, the oscillator strength of the 1050 nm transition $^3F_4 \rightarrow {}^3F_2$ was found to be about 10 % smaller in the indium fluoride based glass and the 1400 nm transition $^3F_4 \rightarrow {}^3H_4$ is about 10 % larger.

The emission cross-section of the $^3H_4 \rightarrow {}^3F_4$ transition used for amplification in S-band, was measured to be about 17 % larger in the indium fluoride glass compared to ZBLAN. However, the competitive $^3H_4 \rightarrow {}^3H_5$ transition and contributed with its emission at 2300 nm is also stronger by nearly the same factor, which does not show any significant advantage of the IBZP glass.

Summarizing all these observations, it is not expected, that IBZP glass is a much better host glass for thulium-doped fiber amplifiers than the usual ZBLAN glass, and therefore the further work will concentrate on TDFAs based on ZBLAN fibers.

4 Fiber couplers for TDFA

As described in chapter 2, the energy level diagram of thulium shows a lot of relevant transitions, which are of interest regarding its performance. In the amplifier setup the ground and excited state absorptions at 790, 1050 or 1420 nm play very important role for an optical pumping while the signal amplification occurs for wavelengths in the region of 1460 nm. For effective pumping process it is necessary to couple both, signal and pump radiation in one fiber with a high coupling ratio (CR) and low losses. In fiberoptic systems like TDFA this can be realized by application of fiber couplers.

There are different methods to manufacture fiber couplers, such as etching [112], employing lenses [113], using two core fibers [114] or finally polishing [115, 116], but the most common manufacturing method is fusing or tapering. The coupler is formed by fusing two single-mode fibers with a flame microburner [117] or microheater [118]. The advantage of using microheater is that the manufacturing process can be controlled easily whereas manufacturing coupler using microburner is less time-consuming. The couplers produced with a microheater are typically longer, which is inconvenient for telecommunication systems employing a number of different coupler-based devices like e.g. add/drop multiplexers. The coupler manufacturing device, which was used during this work, is one featured with microheater and the coupler production procedure is as follows: two uncoated fibers are placed on two linear translation stages assuring intimate contact between them. The stages move in opposite directions after heating the fibers close to the temperature when they start to soften (approx. 1570 °C for typical SiO_2 fiber). The movement must be controlled very precisely and the typical pulling speed varies typically from more than $50\,\mu$m/s on the beginning of the process up to less than $5\,\mu$m/s when the coupler is almost done. The applied tension leads to elongation of the fused region with a consequence of decreasing its cross-section. In this way up-taper and down-taper are formed at both ends of coupling zone. Because of the symmetry during the manufacturing process both tapers are identical and therefore this type of couplers is also called bidirectional biconical coupler. Nevertheless for the convenience, as long as it is not extra emphasized, the ports on the left hand side of the coupling zone will be treated as input ports and respectively the right hand side ports as outputs of the coupler. The basic setup used for the manufacturing of the fiber coupler is shown in figure 4.1.

During the manufacturing process, the power of the outgoing optical radiation is continuously measured with detectors and both the coupling ratio and excess losses are calculated. These values are recorded as a function of time, which corresponds to the length of the coupling zone. The manufacturing process ends when the expected coupler parameters are
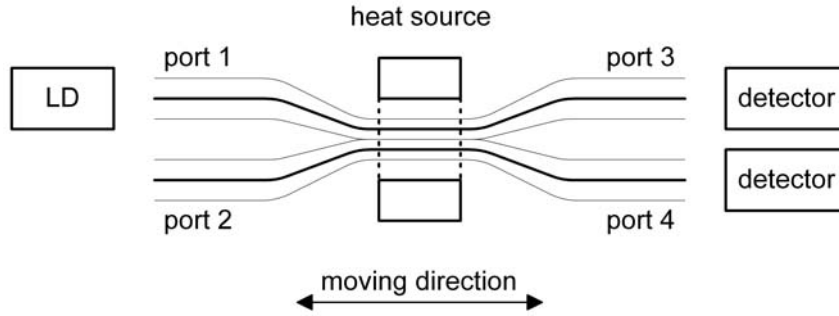
Figure 4.1: Setup for manufacturing a biconical optical fiber couplers

achieved. These are already mentioned coupling ratio *CR*, which is defined as

$$CR_n = \frac{P_n}{P_n + P_m} \; , \tag{4.1}$$

where P_n and P_m are the powers measured respectively at output n and m. The second parameter determining manufacturing of the coupler is the target number T defined as number of points when the power in both output fibers is equal. Because of the fact that the heater moves slowly back after the manufacturing process is over, the final and target *CR* differ slightly. The temperature profile and pulling speeds with time intervals are used as parameters of the manufacturing process as well. A typical temperature profile for a very long coupler is shown in figure 4.2.

It can be divided into several steps with the different target temperatures and pulling speeds. During the first 200 seconds, the microheater is warming up from 1200 °C of stand-by temperature up to 1590 °C, which is above the softening temperature of silica fibers. During this time no force is applied, and the fibers fuse along the uncoated region. After that the force is applied for more than 90 seconds causing significant elongation of coupling zone. During next steps the temperature and pulling speed decrease to 1300 °C and 5 μm/s respectively. For most cases there is no need to draw a coupler over very long time; the target parameters are typically achieved up to the end of forth region.

Since both fibers forming the fiber coupler are in contact along the certain region, its length has the influence on the coupler's performance. On one hand it determines the thermal and mechanical stability of the coupler, from the other hand it correlates with the coupler's bandwidth. Generally, short pulling length corresponds to broadband coupler and in the case of long pulling length one can expect spectrally narrow couplers. The pulling length is one of the parameters, which are important for the simulations of the fiber couplers. It corresponds to coupling length, but it is important to note that, both values are *not* equivalent. The coupling length is some non-linear function of the pulling length. Due to the fact, that the
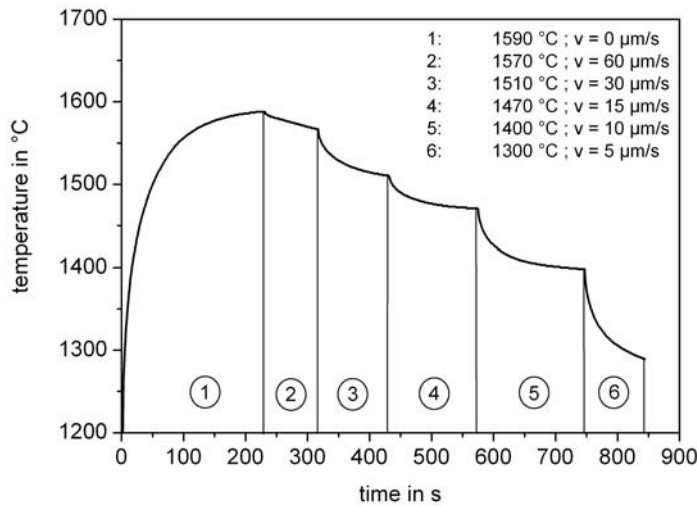
Figure 4.2: Temperature and speed profile for the fiber coupler based on standard SMF-28 fiber

microheater melt the fibers slowly, they stick to each other over long distance, for which also the geometry of the fiber changes. It is obvious, that the core diameter of the fiber, which is pulled decrease exponentially. As a result, the power coupled between both fibers becomes significant. Unfortunately, the time or position, from which this process starts depends also on non-deterministic parameters like space between both fibers or the local fluctuation of the fiber diameter. Therefore, the pulling or coupling length has only limited importance and should not be used to compare two couplers, but since the elongation length is measured by coupler manufacturing device we will use it for description of the particular coupler.

Typical pulling lengths for simple coupler is in the order of 15 to 20 mm, and fits 60 mm long glass substrate which is used to protect the coupler. For special couplers like 3λ-wavelength division multiplexers (WDM) or couplers which are designed for wavelengths, which are very close to each other, the length of the coupling region is longer (up to 23 mm) what makes the coupler thermally and mechanically more sensitive.

In the last manufacturing step the coupler is packaged to minimize the influence of the working environment (temperature, humidity, dust). The finished coupler is then fixed on the glass substrate in a form of a rod with a slit. Afterwards, the structure is protected using a stainless steel pipe, which is closed from both sides with a glue. For this purpose UV-curable adhesive was used, because of its short curing time (approx. 2 minutes), less stress during curing, and easy handling. The viscosity requirements of the glue differs comparing to adhesives surveyed for glue-splices (compare chapter 5.3.2). In this case the high-viscosity glue

is favorable, because it does not flow into the pipe, which may cause adverse aging processes, instability of the coupling ratio or the increase of the excess losses.

Before using the couplers they were characterized according to the procedure described in chapter 4.4. Some couplers change their parameters directly after manufacturing process, which can be caused by tensions appearing during manufacturing and/or packaging process, therefore it is advisable to characterize them after few days resting.

4.1   Coupled-mode theory

There are many publications describing modelling of the couplers [119–122]. They all base on coupled-mode theory, but due to different simplifying assumptions their complexity is different. For the coupler simulation the mathematical description of the processes in coupler are of big importance, although the analysis of fiber coupler starts with the description of the taper and tapering process. As presented in figure 4.3, the taper structure consists of two taper-transition regions and the waist, which is optically well guiding structure supporting its own modes.
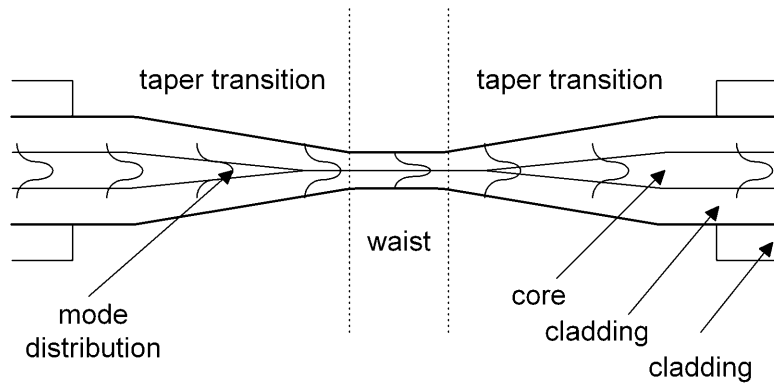
Figure 4.3: Modell of optical fiber taper

Due to fiber elongation and change of its cross-section in the waist region there is no more core/cladding structure which guides the radiation, but the light propagates over the whole width of waist and the total internal reflection occurs at the interface between glass (former cladding) and air [123]. This is caused by conversion of the core mode into cladding mode in the waist region. Further, when the core diameter increases this process is reversed and the fundamental mode is recaptured by the enlarging core. The taper transition region is very critical and determines the propagation of the incoming radiation. The most important issue for the taper is the adiabatic criterion, which depends on taper transition profile. The taper is *adiabatic* if its angle is small enough to ensure negligible loss caused by the power conversion between the propagating modes. Assuming the input radiation to be in lowest order mode

(HE_{11}), which is able to propagate in such a guiding structure [124, 125] the mode adiabatic criterion can be written as:

$$\left| \frac{dr}{dz} \right| \leqslant \frac{r}{z_b} \; , \tag{4.2}$$

where r is the core fiber radius, and z_b is the beat length between the two lowest modes. The beat length depends on the propagating constants (β) of the HE_{11} and next possible mode (HE_{12}) and is defined as:

$$z_b = \frac{2\pi}{\beta_1 - \beta_2} \; . \tag{4.3}$$

In other words, if the angle of the taper is smaller than the ratio between the fiber core radius and the beat-length then the local losses caused by the mode conversion can be neglected. As reported in [126, 127], for non-adiabatic taper, which does not satisfy the condition given in previous equations, the power of the fundamental mode will be transferred into higher modes with the same azimuthal symmetry. As a result the power propagating in high order modes will *not be reconverted* into fundamental mode in second tapering region causing high losses. This shows how important is the shape of the taper and as conclusion it is to point that the puling speed during the taper production has to be low and it is advantageously to use heat source, which is significantly wider then the diameter of the fiber. Both of these conditions are fulfilled by our coupler manufacturing device. The width of the microheater is 22 mm and the pulling speed as low as some μm/s can be use to elongate the fibers.

Because of the fact, that the taper is no more well-defined core/cladding guiding structure it behaves in principle like glass/air structure. The total internal reflection occurs on the surface between glass and air and the single-mode operation is no more assured.

Combining two tapered fibers like in fiber coupler, makes the analysis more complicated. From one side, the geometry of the guiding structure is different from that of the fiber. On the other side, the decreasing of the fiber core diameter below the wavelength of the radiation causes that the regions called before "core" and "cladding" become one guiding structure. From this time the electro-magnetic field propagates in the glass/air guiding structure, where the multimode (or more precisely - supermode) operation occurs.

Considering that the radiation, which enter the coupler is in the fundamental mode, it can be seen as the superposition of odd and even modes. Power exchange between two fibers occurs as a beating between the modes in the waist region [128], which are called supermodes. They behave similar to modes propagating in the taper and they can be described by applying the coupled-mode theory. The detailed analysis of biconical fused fiber couplers basing on the coupling-mode theory is given in [116, 123]. The performance of the coupler depends on the coupling length. At the beginning of the coupler manufacturing process the radiation introduced into one fiber does not couple into the other fiber. In this case the phase difference is very small, smaller than $\frac{\pi}{2}$, for which the power splits equally to both output fibers. Such a coupler is called also "3dB coupler". Further increasing of the phase difference leads to coupling

more power into port 4. The maximal coupling is achieved, when the phase difference is π. In this case the odd and even modes interfere constructively in the second fiber and destructively in the first one. The power coupling process is reverse, it means further increasing of the coupling length leads to the recapturing of the radiation into first fiber. This means, that the coupling process depends on the phase difference, which is difficult to measure, but it can be estimated when the fiber parameters and the coupling length are known. In the general case the output powers of the fiber coupler are given by:

$$
\begin{aligned}
P_3 &= P_1 \cos^2(\kappa z) \ , \\
P_4 &= P_1 \sin^2(\kappa z) \ ,
\end{aligned}
\tag{4.4}
$$

where κ is the simplified coupling constant and z is the z-coordinate corresponding to the coupling length. As reported in [123], κ can be understand as the spatial function of the propagation constants of the odd and even lowest order modes β_o and β_e, and it is given by:

$$
\kappa(z) = \frac{\beta_o(z) + \beta_e(z)}{2} \ .
\tag{4.5}
$$

The propagation constants β_o and β_e depends on the refractive index n of the guiding structure and the propagation angle Θ_x, and they satisfy the equation:

$$
\beta = \frac{2\pi}{\lambda} \, n \sin \Theta_x \ .
\tag{4.6}
$$

In fact, the coupling parameter κ is defined much more complex and is difficult to calculate. Nevertheless, it can be found by the numerical solving of the coupling equations.

4.2   Simulations of the biconical fused coupler

The modelling of fused fiber coupler is not a trivial challenge. As a standard technique for analysis of such a optical components, a Beam-Propagation Method (BPM) [129, 130] is applied. In this method fiber is replaced with a system of lenses and the electro-magnetic field between lenses matches the solutions of the Helmholz equation in homogenous medium. Since it is partial-integral equation, it has to be solved numerically using a calculation methods like finite elements (FE-BPM) or finite differences (FD-BPM). Although they are very accurate, the aim of this work regarding fiber couplers was implementing some model, which easily describes coupler's behavior and leads information about its basic parameters.

In the praxis, during the coupler's manufacturing a radiation source is needed in order to measure the coupling ratio on-line. The source used for the manufacturing has to correspond with the later wavelength, for which the coupler is optimized. But when two or three wavelengths are coupled using a single fiber coupler, the information about coupling ratios for all of them is of general importance. According to our requirements, modified model of biconical fiber coupler presented by V. J. Tekippe [131] was used. The model bases on investigations of

J. Bures [119] and A. Antkiewicz [120] and is used to estimate the power cross-coupled into port 4 (see fig. 4.1). According to the model, the power at port 4 is given by:

$$P_4(z) = F^2 \sin^2\left(\frac{C}{F} z\right) , \qquad (4.7)$$

where F^2 corresponds to the input power P_1 and is called the maximum coupled power, C is the coupling coefficient and z is the axial coordinate.

The model presented here uses some simplifying assumptions. Some of them are obvious and they result from the coupled-mode theory. Another are model-specific, but it seems to be important to collect all of them in one place. According to the coupled mode theory:

- the coupling occurs only after essential reduce in the cross-section of coupled fibers,

- the light propagates in former cladding and air serves as medium assuring total internal reflections,

- significant coupling occurs only over the width of the heater,

Additional assumptions introduced in the applied model:

- fibers forming the coupler are just in contact,

- the reduced fiber core diameter is given by $d = d_0 \exp{-\frac{L}{w}}$, where L is the coupler elongation length and w is the micromicroheater's width

- refractive index of glass forming waist structure is $n = 1.46$.

The coupling constant C in equation (4.7) in general case is the spectral function of the fiber core [120] and is given by the equation:

$$C(\lambda, d) \sim \frac{4}{d} \sqrt{\frac{\Delta}{\pi D}} \frac{2.405}{V^{5/2} \exp(V(D-2))} , \qquad (4.8)$$

where Δ is the relative difference of the refractive indices for core and cladding glass, D is the degree of fusion for fibers forming the coupler, and V is the normalized frequency. They are formalized as:

$$\Delta = \frac{n_{core}^2 - n_{clad}^2}{2n_{core}^2} , \qquad (4.9)$$

$$V = \frac{\pi d n_{core}}{\lambda} \sqrt{2\Delta} . \qquad (4.10)$$

Basing on the simplified assumptions and assuming fibers to be in "just-in-touch" ($D = 2$) the equation (4.8) reduces to:

$$C(\lambda, d) = 84 \, \frac{\lambda^{5/2}}{d^{7/2}} \; . \tag{4.11}$$

The maximum power F^2 from equation (4.7) can be expressed as:

$$F^2(\lambda, d) = \frac{1}{1 + \left(\frac{234 \, d^3}{\lambda^3}\right) \left(\frac{\Delta d}{d}\right)^2} \; . \tag{4.12}$$

In equations (4.8) - (4.12) the parameter d is the fiber core diameter modified during the tapering process, λ is the operating wavelength, Δd is the difference in initial diameters between both fibers, n_{core} is the refractive index of the core glass, and n_{clad} is refractive index of cladding glass. When the same fibers are used to form the fiber coupler ($\Delta d = 0$) the equation (4.12) simplifies to $F^2 = 1$.

With the model based on the equations given above the spectral behavior and coupling ratio as a function of length of the coupling zone can be easily investigated with two parameters such as fiber core diameter and microheater width. It is clear that the accuracy of the model is poor, but it is enough to predict the coupler's performance for the wavelengths, for which the radiation source is not present.

4.3   Coupler model's verification

Before the simple coupler model can be used as a helpful tool to design different types of couplers it has to be compared with the measurement. For that reason different test structures in form of very long couplers were manufactured using sources emitting radiation at different wavelength. The results of comparison between simulation and measurement are shown in figure 4.4. The measurement curve is the averaged characteristic for 5 test structures manufactured for different powers at 1470 nm using standard SMF-28 fiber. The parameters used for simulation are shown in table 4.1.

As expected, measurement and simulation fit quite well, but not fully. The measurement characteristic can be reproduced by the simulation with quite good accuracy, nevertheless the discrepancy is not surprising since the model base on many simplifying assumptions. It is also worth to remember, that the coupling length's concept used in the model is very inaccurate and difficult to measure. On the other hand, it has less meaning for the practical use, since the coupling process is interrupted after achieving the target value of the coupling ratio and not the particular coupling length.

For the coupler manufacturing it is very important what happens with local minima and maxima of coupling ratio for measured and simulated characteristics. As shown in figure 4.4
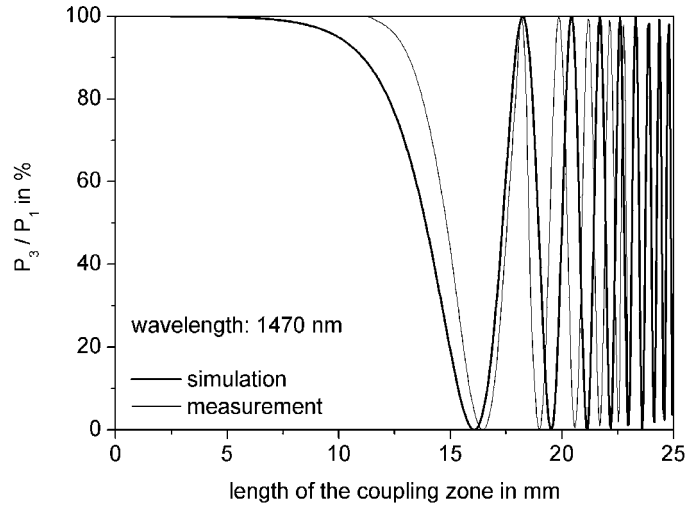
Figure 4.4: Simple coupler model - comparison between simulation and measurement

Table 4.1: Parameters used for verification of fibre coupler model

parameter	value
fiber core diameter d	8 μm
difference in core diameters Δd	0
heater width	22 mm

they are in good agreement and therefore the simulations can be used for designing not only simple power coupler (like 3dB coupler), but also $2\lambda-$ or 3λ-WDM couplers especially in the case when source for one of wavelengths, for which coupler was design is not available (like in example shown in figure 4.5).

For the advanced pumping scheme 3λ-WDM couplers combining pump, signal and laser radiation are needed. Unfortunately, analyzing figure 4.5, it is clear that it is almost impossible to manufacture this type of the coupler with the ideal coupling ratios. Nevertheless, the favorable tradeoff can be achieved for point B. But regarding experience concerning coupler manufacturing, long coupling length leads to higher thermal sensitivity of the coupler and difficulties during packaging process. Therefore it will be advantageous to produce coupler with shorter coupling zone. On the other hand the manufacturing process interrupted in point A leads to very unfavorable coupling ratios for all three wavelengths.
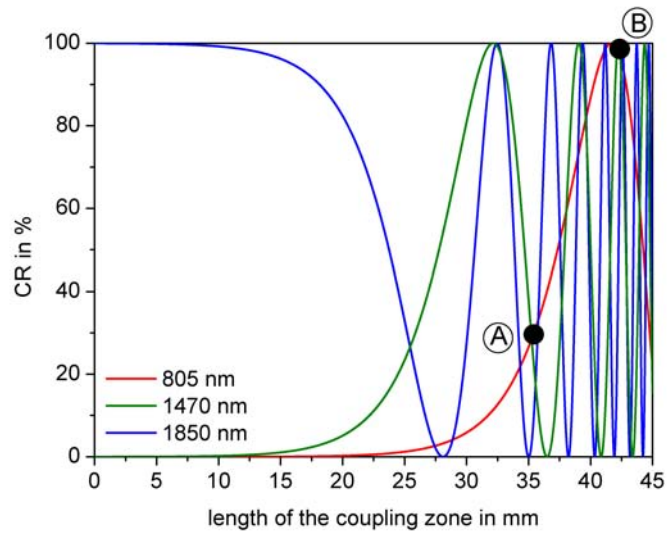
Figure 4.5: Simulation of 3λ-WDM: 800+1470nm\1900nm

In the next chapter designing of special couplers for thulium-doped fiber amplifier and its characterization procedure will be reported with special focus on coupling ratio and excess losses.

4.4   Special couplers for TDFA

There are many companies manufacturing standard fiber coupler for typical applications as WDM couplers for erbium-doped fiber amplifier or power dividers operating mostly in C- and L-band. For applications in the S- and S$^+$-band the commercial interest is lower and therefore available devices working aside of typical wavelength regions are expensive and very seldom. Furthermore, for the experiments couplers with different coupling ratios are needed, which justifies manufacturing couplers by ourselves.

Some problems can be found, when radiations with very distant wavelengths have to be coupled together, which is often the case in TDFA. The couplers, which are necessary can generally be divided into two main groups; 2λ− and 3λ−WDMs. The first group couples single pump and signal radiation into one output fiber. Another group of couplers is used to couple more than two radiation sources operating at different wavelengths, as it is needed for advanced TDFAs. The most important parameters of any type of the coupler are coupling

ratio CR and excess losses α_e^{dB}, which are defined as:

$$\alpha_e^{dB} = 10 \log \left(\frac{P_3 + P_4}{P_1} \right) ,\qquad\qquad (4.13)$$

where P_i is the power on i^{th} port according to figure 4.1. Although the CR and α_e^{dB} are measured during manufacturing process, sometimes it is also important to measure them spectrally, which is especially important in case of long fiber couplers, where CR changes rapidly with the wavelength. The name convention used for labelling the couplers presented here is as follow: $2\lambda-\text{WDM:}\lambda_1\backslash\lambda_2$ or $3\lambda-\text{WDM:}\lambda_1 + \lambda_2\backslash\lambda_3$ where the "\" sign is used to separate both input wavelengths of the coupler. The wavelengths are given in nanometers and for labelling of the signal wavelengths "1470" is used. Additionally, every coupler has a serial number, given in parentheses, which differentiates it in the group.

4.4.1   Examples of $2\lambda-$WDM couplers

In this group three types of couplers were manufactured. Coupling ratios and excess losses for some of them are collected in table 4.2. The number of couplers manufactured for each group was much higher, but the couplers with the best achieved parameters are collected in the table. They were characterized using well known cut-back method, which is used for measuring attenuation of the fiber. In the table excess losses α_e^{dB} were assigned as α.

Table 4.2: Parameters of some $2\lambda-$WDM couplers

coupler type	CR_{λ_1}	CR_{λ_2}	α_{λ_1}	α_{λ_2}
$2\lambda-$WDM: 805\1470 (6)	3.2	92.8	0.2	0.1
$2\lambda-$WDM: 805\1470 (8)	8.2	89.9	0.2	0.1
$2\lambda-$WDM: 805\1470 (9)	9.1	90.3	0.1	0.1
$2\lambda-$WDM: 1055\1470 (1)	9.1	88.4	0.5	0.1
$2\lambda-$WDM: 1055\1470 (2)	1.4	94.8	0.4	0.1
$2\lambda-$WDM: 1055\1470 (4)	2.7	95.6	0.1	0.1
$2\lambda-$WDM: 1416\1470 (3)	12.2	98.2	0.1	0.1
$2\lambda-$WDM: 1416\1470 (4)	8.7	97.9	0.1	0.1
$2\lambda-$WDM: 1416\1470 (5)	8.5	75.5	0.3	0.1

The WDM couplers are characterized by the fully wavelength selection. It means that the expected coupling ratios for coupled wavelength should differ significantly and in the ideal case the CR for one wavelength is expected to be 100 % and 0 % for the second wavelength. Unfortunately, such a conditions are difficult to satisfy for short coupling lengths assuring good thermal stability of the coupler. Therefore some tradeoff has to be met to produce usable coupler. Since the pump power is limited one has to take care of using it efficiently.

On the other hand, low coupling ratio for the signal wavelength for which the amplifier is optimized does not have a sense. Therefore we decided to optimize the couplers for the signal wavelengths.

It is easy to see that excess losses for pump wavelengths (805 and 1055 nm) are higher than for signal wavelengths. This difference can be explained due to multi-mode nature of the standard single-mode fiber (SMF-28) used for the coupler manufacturing. In the ideal case, a fiber which is *single-mode* and *guiding* for both wavelengths should be used, which is difficult for commercially available fibers. Another possibility is to use two different fibers, which are single mode for pump or signal wavelength, but because of minimal differences in glass composition the problems with coupler manufacturing can increase rapidly. On the other hand the advantage gained by using special fiber for coupler manufacturing is easily lost because of high attenuations on the connection between SMF-28 and special fiber as described in chapter 5. The multi-mode behavior of SMF-28 below cut-off wavelength (at approx. 1230 nm) is easy to identify in figure 4.6.
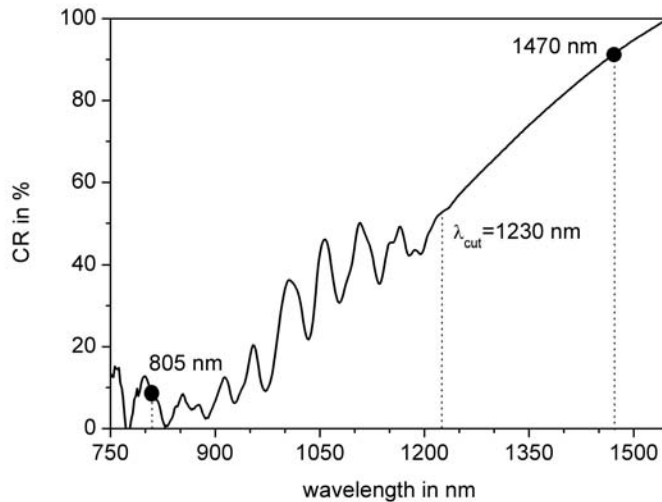
Figure 4.6: Coupling ratio spectrum for 2λ-WDM: 805\1470 (6)

Many ripples makes the routine spectral measurements of coupling ratios for couplers made from SMF-28 uninteresting for the wavelengths below 1230 nm. Nevertheless, the spread main wavelengths for pumping diodes at approx. 800 nm and 1050 nm is limited to several nanometers and the proper CR can be directly measured using the diode, which will be finally used in the amplifier setup.

4.4.2   Examples of 3λ−WDM couplers

For most TDFA setups three wavelengths have to be coupled with low losses, which makes optimization of theses couplers very difficult. On one hand, the coupling ratio and excess losses should be kept low for signal wavelength because of the efficient amplifier operation, on the other hand, pump powers, which are sometimes insufficient, have to be coupled with low loss. Nevertheless, in most cases the couplers were manufactured and optimized for signal wavelengths. Some examples of 3λ−WDM couplers are shown in table 4.3.

Table 4.3: Parameters of some 3λ−WDM couplers

coupler type	CR_{λ_1}	CR_{λ_2}	CR_{λ_3}	α_{λ_1}	α_{λ_2}	α_{λ_3}
3λ−WDM: 1055+1470\805 (6)	97.5	97.0	8.9	0.4	0.3	0.3
3λ−WDM: 1055+1470\805 (7)	95.9	87.8	1.8	0.3	0.5	0.3
3λ−WDM: 1055+1470\805 (9)	96.0	90.1	2.7	0.4	0.1	0.3
3λ−WDM: 805+1470\1850 (12)	93.9	71.9	8.7	0.2	0.3	0.9
3λ−WDM: 805+1470\1850 (13b)	94.9	95.3	5.8	0.2	0.1	0.7
3λ−WDM: 805+1470\1850 (16)	96.1	97.3	1.8	0.2	0.1	0.8

Measured coupling ratios and excess losses for 3λ−WDM couplers are very close to the expected ideal values, but for the coupler manufacturing process the 3λ−WDM: 805+1470\1850 couplers are much more interesting. The value "1850" represents the amplified spontaneous emission (ASE) caused by transition $^3F_4 \rightarrow ^3H_6$ in Tm^{3+} and centered at approx. 1800 nm. When the laser conditions are satisfied superluminescence or laser oscillation operation can be observed as it was discussed in further chapters. The laser wavelength is slightly larger than the maximum of the ASE. Therefore the information about spectral behavior of coupler for the 1800 nm ASE is very important. For that reason a simple ASE source was constructed consisting of 45 cm of thulium-doped fiber pumped with a 805 nm laser. Its setup is shown in figure 4.7.
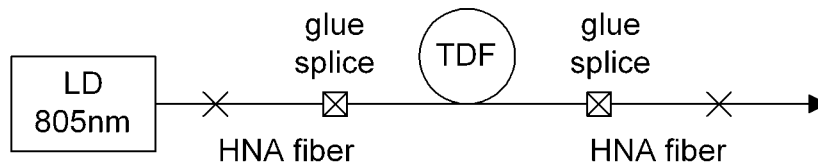
Figure 4.7: Setup of ASE-source used for coupler characterization

With a 10 μW maximal output power of ASE centered at 1800 nm it was possible to char-

acterize couplers. The measurements were performed using emission spectrometer described in chapter 3.4.1 and the outgoing radiation was measured using indium InSb detector cooled with liquid nitrogen. The coupling ratio in the signal wavelength range was determined using fiber attenuation measurement system (S25, York). Results of these measurements are shown in figure 4.8.
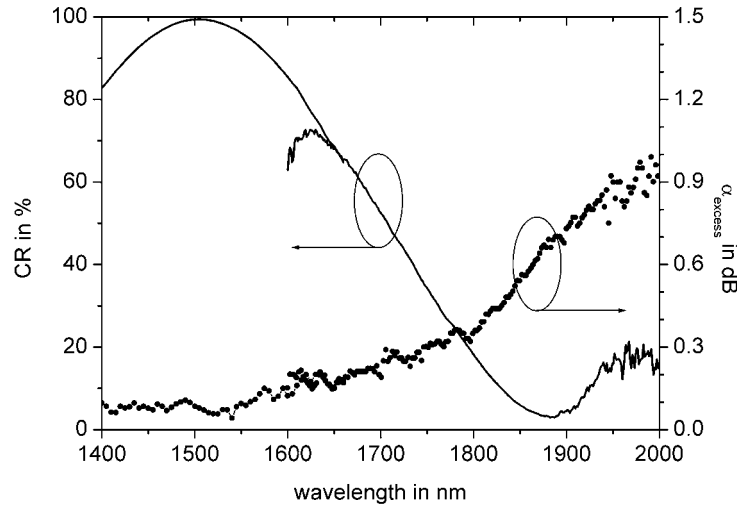
Figure 4.8: Coupling ratio of $3\lambda-$WDM: 805+1470\1850 (13b) measured using S25 (wavelength region 1400 to 1650 nm) and emission spectrometer with ASE source (wavelength region 1600 to 2000 nm)

The coupling ratio spectrum resembles sinus function, which is not surprising. The ripples at the beginning and at the end of the region covered by ASE source result from very low outgoing powers measured for that wavelengths, but this wavelength region was also covered by the measurement performed with the S25. The overlapping part of the measurements (from 1600 to 1650 nm) shows very well agreement.

One can expect that excess losses are not wavelength dependent. Of course, for the regions where fiber works in multi-mode regime, the losses (and also excess losses) increase because of non-gaussian field distribution. Since the fibers have to be uncoated, the rest of the coating or scratches on the outer surface of fiber cause additional losses, which are basically wavelength independent. Nevertheless, when the impurities exceed the dimensions, which are comparable with coupled wavelengths their importance drastically increases. Also the V-number, quantifying the ability of guiding the light, becomes smaller for longer wavelengths and already for 1600 nm its value is 1.806 and for 1850 nm exceed 1.562, which is below guiding limit of 1.6. Therefore for wavelengths longer than 1700 nm the SMF-28 fiber guides worse and the excess losses of the coupler manufactured out of it increase. Nevertheless, their value

is not very critical because the $^3F_4 \rightarrow {}^3H_6$ transition is relatively strong.

5 Fiber connection techniques

The question of connecting different types of fibers plays an important role for realizing thulium-doped fiber amplifier, especially when the diode-pumped setup should be realized. The limited maximum output power from laser diode forces the development of efficient methods to connect the laser diode with the rest of the fiber-optical setup. Laser diodes, used for realizing TDFA setups, were supplied with a pigtail made of special type of the fiber assuring single-mode guiding of the radiation. Since the used fibers have different parameters as core diameter d and numerical aperture NA, the attenuation caused by mode field diameter mismatch is significant. As next, thulium-doped fibers (TDF) are typically high numerical aperture fibers (HNF) to provide high power density in core (see chapter 2). But the most critical point is to effectively join any type of silica fiber and fluoride based TDF. The differences caused by thermal and mechanical parameters as well as dissimilar glass types (predominantly ionic ZBLAN and covalent SiO_2) make the thermal splicing impossible. As will be discussed later, the glue splicing seems to be mostly suitable. Figure 5.1 shows simple TDFA setup with clearly marked fiber connection points.
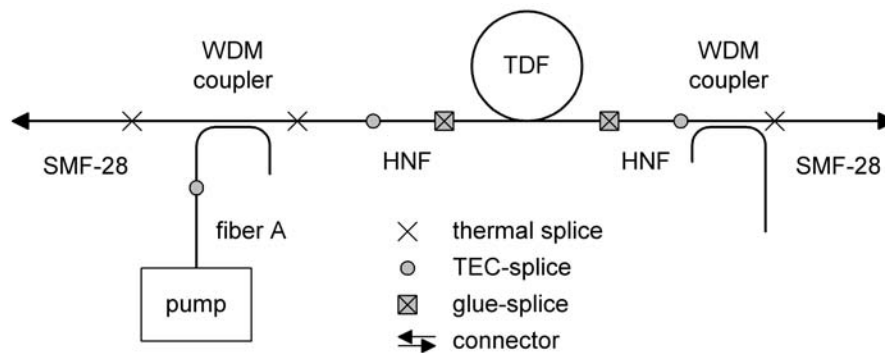
Figure 5.1: Diagram of simple thulium-doped fiber amplifier

There are four connection types existing in typical TDFA setup. One of them are connectors, which are present only on the input and output of the amplifier. They are difficult to avoid because of necessity to couple the input signal into the setup and to guide the amplified radiation to measurement devices as optical spectrum analyzer, which quantify the performance of the amplifier. To minimize the reflections FC/APC connectors type were chosen. The endface angle of approx. 8° assures negligible reflections and makes them indecisive for the amplifier performance. With 0.3 dB typical losses their influence on the attenuation budget of amplifier is also marginal. As long as the simple thermal connections were made

automatically with a fusion splice device (Fujikura, FSM 40S) and their attenuation is much lower than 0.1 dB, they can also be omitted in further descriptions of the fiber joining methods. Much more critical is connecting two fibers with different geometrical parameters or fibers having different thermal properties. The most suitable connection methods will be discussed in the following chapters.

5.1   Thermal fiber connecting methods

There are several methods to connect fibers heated up above their melting (softening) temperature. They differ in the method of supplying the energy needed to warm up the fibers. Since the methods are universal, they have to assure very precise temperature control in a very broad temperature range.

Solving the problem of joining fibers with different geometrical parameters is very important for realizing all-fiber setup of any fiber amplifier. This problem is not so grave in the case of EDFAs, since they base mostly on erbium-doped *silica* fibers with similar mechanical and thermal properties like all other fibers used in the amplifier setup. The core diameter and numerical aperture of them generally differs from that of standard single mode fiber like SMF-28, but that inconvenience can be easily solved using thermally-diffused expanded core (TEC) technique. The problem increases when tellurite [132, 133] or fluoride based fibers [134] are used as host-glass for rare-earth dopant. Due to the refractive index of approx. 2.0 in tellurite-based fibers the Fresnel reflection on the connection point to silica fiber is significant. It is defined as:

$$R = \left(\frac{n_1 - n_2}{n_1 + n_2} \right)^2 \ , \tag{5.1}$$

where n_1 and n_2 are the refractive indices of two connected materials. In the case of EDFA based on tellurite fiber, $n_1 = 1.46$ and $n_2 = 2.0$ the Fresnel reflection exceeds $\approx 2.5\%$ which is relatively high. Since both fibers have different thermal properties, they can not be spliced. They are joined angularly using V-groove connection with the attenuation, which can be kept as low as 0.3 dB [133].

The mechanical and thermal properties of fluoride based fibers preclude their automatical thermal splicing as it can be done using fusion splicer. Nevertheless, several attempts were reported to thermally join this type of fibers using precisely controlled glow discharge [135, 136], wolfram wrapping [135] or application of CO_2 laser [137].

Because of the problems with achieving low temperature using glow discharge, which has to be precisely controlled, the repeatability was very poor and the losses reached values up to 6 dB [135]. Additionally the melting region of approx. $220\,\mu$m was cooled down slowly, causing building the crystals, which is critical for fluoride based glasses. Furthermore, the

discharge time and current have to be kept very low making the joining process for fibers with small fiber diameter very difficult to control. Much better results are reported in [136], where helium purge was used to homogenize the temperature between electrodes in fusion splicer. Using a multi-mode fiber with the core diameter of $40\,\mu$m, discharge current of $7\,$mA and time less than $1\,$s the losses of less than $0.1\,$dB for 11 splices were reported.

With the temperature-controllable wolfram wrapping (temperature application region of 20 to $2500\,°$C) losses of $0.2\,$dB were achieved for fibers with the core radius of $200\,\mu$m [135].

The application of CO_2 laser, which was earlier reported as a method for joining of SiO_2 fibers [138] leads to a very low average splice loss ($0.18\,$dB) in the case of joining two silica fibers with core diameter of $8\,\mu$m. Fluoride glasses show very narrow viscosity phase and a low fusion temperature and can not support heating in normal atmosphere for more than few seconds. After that time, a hydrogen layer start to build on the fiber ends leading to fiber degradation because of high hygroscopicity of the fiber. The observed losses for connecting two ZBLAN fibers with core diameter of $54\,\mu$m and numerical aperture of 0.14 were close to $0.3\,$dB. The melting zone was as small as $80\,\mu$m and it was small enough to warm-up effectively both fiber ends.

Another temperature connection technique, however not very popular, is so called "glass soldering" [139]. In that method two fibers are connected using water based soldering paste with refractive index which matches that of the fibers. For the sake of hygroscopicity of ZBLAN fibers and the necessity to warm up the soldering paste, that method is not applicable for special type of fibers like ZBLAN despite of its relatively low reported connection losses (of 0.2 to $1\,$dB).

Summarizing, due to the differences in thermal properties of SiO_2 and ZBLAN and the glass type dissimilarity the realizing of stable and reliable thermal connection is impossible. Therefore another joining technique has to be develop to omit these physical limitations.

5.2   Thermally-diffused expanded core (TEC) technique

The silica fibers forming TDFA setup differ in numerical aperture and core diameter. The requirement of low-loss connection between them seems to be relatively easy to realize by using the thermally-diffused expanded core (TEC) technique, which is well known since 90's of the last century. It helps to minimize losses caused by mismatch in mode field diameter of two different fibers and minimizes alignment losses for connection between fiber and laser diode [140, 141]. The TEC technique bases on thermal splicing method, which is meanwhile widely used for connecting any type of silica fiber. The splicing occurs after heating up both fibers above their softening temperature and shifting them towards each other very precisely. The energy needed for getting fibers warm can be delivered by laser source (e.g. CO_2 laser) or a

gas burner (propane or hydrogen). Nevertheless, in every portable splice device, the fibers are heated up with glow discharge between two electrodes [142]. The most important advantage of this technique is the high mechanical stability of the connection caused by narrow and symmetrical heating zone. This results also in very low attenuations for connecting typical fibers (typically less than 0.03 dB for connecting two SMF-28 fibers).

The special structure of TEC can be achieved in SiO_2 fibers with core co-doped with germanium. Due to the high temperature induced by the fusion splicing, the fiber is heated into a temperature over the melting (softening) point and the diffusion of germanium from core to cladding occurs. This leads to local changes in refractive index of the cladding, which in fact leads to expanding of the core region as reported in [143, 144]. Alternatively to germanium doped core, for forming TEC one can use also fluorine doped cladding [145]. Because of the higher diffusion velocity of fluorine, the time needed to achieve core expansion is in this case much shorter.

For thulium-doped fiber amplifier losses caused by different MFDs are of big importance and the aim to minimize them forced author to develop special splicing program. By increasing the heating temperature [140] or time one can drastically decrease losses caused by MFD mismatch. These losses can be calculated according to the following equation:

$$\alpha_{MFD} = \left(\frac{2 \cdot MFD_1 \cdot MFD_2}{MFD_1^2 + MFD_2^2}\right)^2 \ , \tag{5.2}$$

where MFD_i is the mode field diameter of ith fiber. It can be calculated for any fiber using equation (8) from [146]:

$$MFD = d_{core}\left(0.65 + \frac{1.619}{V^{1.5}} + \frac{2.879}{V^6}\right) \ , \tag{5.3}$$

where V is the guiding constant defined as

$$V = \frac{\pi d NA}{\lambda} \ . \tag{5.4}$$

The core diameter and numerical aperture in previous equation are denoted as d and NA respectively. Due to the fact, that the optical losses are commonly specified in decibel, we use special notation to distinguish losses defined as linear ratio and losses in dB. According to this notation the the logarithmic calculated losses α_{MFD}^{dB} are defined as:

$$\alpha_{MFD}^{dB} = 10 \log \alpha_{MFD} \ . \tag{5.5}$$

Since the TDFA setup consists mostly of standard single mode fiber manufactured by Corning (SMF-28), for the loss estimation only connection with pump diodes and HNA fiber are of

Table 5.1: Parameters of fibers used in TDFA setup

fiber name	d in μm	NA	label in fig 5.1
SMF-28	8.0	0.12	SMF-28
UHNA1	2.9	0.26	HNA fiber
HP780	4.0	0.13	fiber A (805 nm pump)
HI1060	5.5	0.14	fiber A (1055 nm pump)

importance. The measured geometrical fiber parameters are collected in table 5.1 and their description corresponds to figure 5.1.

The pump modules used for TDFA were delivered with fiber pigtail and the fibers used for the pigtails were chosen to be singe-mode for their radiation. In figure 5.1 these fibers were labelled as "fiber A". For laser diodes at approx. 1055 nm the pigtail was made of HI1060 and 800 nm diodes were delivered with approx. 1 meter of HP780 fiber. The core diameter and NA were calculated from the mode-field diameter measurement performed using fiber characterization device from York (S25). Since the device measures MFD spectrally, one can directly calculate α_{MFD}^{dB} without estimating the physical parameters of the fibers. On the other hand, they are basic properties of each fiber and are partially used also for amplifier simulation therefore it is appropriate to collect them at this point. The attenuation caused by MFD mismatch for the connection between HP780 or HI1060 and silica fiber are collected in table 5.2 along with the referred wavelengths.

Table 5.2: Losses for direct connection between some fibers used in TDFA setup

fiber connection	α_{MFD}^{dB}	λ in nm
SMF-28 and HI1060	0.25	1055
SMF-28 and HP780	0.48	805

Although the connection losses caused by mode field diameter mismatch are low, they were additionally decreased to 0.3 dB for SMF-28 and HP780 connection using the above described TEC technique. Since achieving low-loss connection between HNF and SMF-28 is important for each wavelength in the amplifier setup, it is appropriate to calculate its attenuation in the whole interesting wavelength range. The result of that calculations are shown in figure 5.2.

Because of the large difference in mode field diameters, the calculated losses are very high for the short wavelengths. Moving towards longer wavelengths the losses decrease, but the V-number decreases simultaneously, which means that below the value of 1.6 the guiding properties of fiber become weaker, which is however significant only for wavelengths above 1500 nm in the case of HNF and 1900 nm for SMF-28. Also here it was possible to decrease
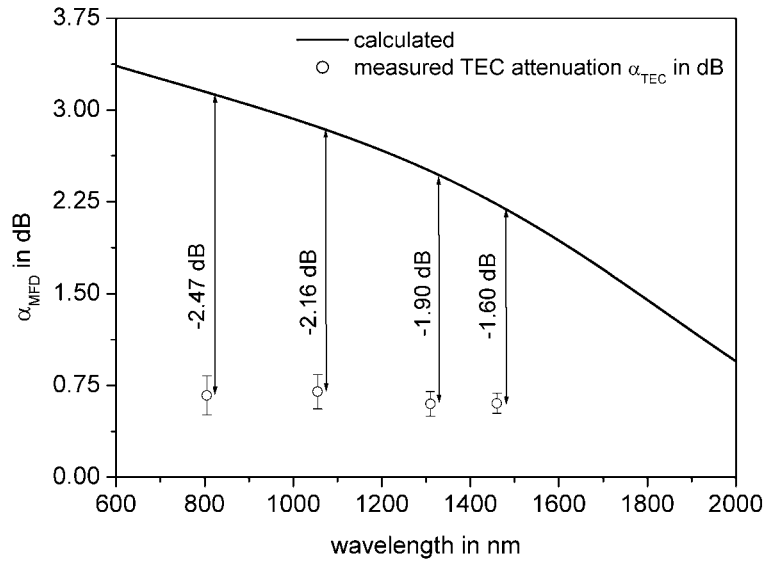
Figure 5.2: Losses caused by mode field diameter mismatch in the case of joining SMF-28 and HNF. Points show improvement achieved by using TEC splices.

the initial attenuation using the TEC-technique, the improvement is by way of example shown in figure 5.2. The attenuation of TEC splices was measured for four wavelengths: 805 nm, 1055 nm, 1310 nm and 1460 nm. The measurement results collected in table 5.3 show the mean value of the attenuation along with the standard deviation of 15 measurements for each wavelength. Significant improvement of the attenuation can be observed and the decrease of the attenuation of about 1.6 dB for 1460 nm or 2.4 dB for 805 nm is a big progress.

Table 5.3: Measured TEC losses for connection of SiO_2 and HNAF

wavelength in nm	$\alpha_{TEC}^{dB} \pm \Delta\alpha_{TEC}^{dB}$ in dB
805	0.67 ± 0.16
1055	0.70 ± 0.14
1310	0.60 ± 0.11
1460	0.61 ± 0.08

The attenuation analysis for fusion splicing of standard fiber is relatively simple, because of the fact that fibers are cut with high precision fiber cleaver (Fujikura, CT-20) assuring almost

the same cutting angle for every cut, which is unfortunately not the case when two angularly cut fibers have to be joined. Although the difference in cutting angles is of importance, fibers spliced together do not show big sensitivity on it. That is also not surprising since the fibers, which are supposed to splice, are heated up above their melting (softening) temperature and then precisely moved towards each other. The thermal treatment "rounds-up" fiber end levelling the fiber endfaces. This feature, which is missing in the case of joining silica and fluoride fibers, makes these connections more difficult.

5.3   Non-thermal fiber connecting method

In the case of fibers which can not be spliced thermally, two different connecting methods can be used. One of them is removable fiber connection, which is very convenient for centric and mechanically stable silica fibers. The typical attenuation of 0.3 dB is admittedly higher than for fusion splicing but gives more re-constructing freedom, but since the fluoride fibers, which were used for TDFA are slightly non-centric, the attenuation in such a connection point increases drastically. Alternatively glue splicing can be used as a non-thermal connection method. There are several setups which lead to stable and reliable join of two different fiber types. The fibers which suppose to be connected have to be placed in V-grooves [142, 147] or special structures [142, 148] assuring precise fiber adjustment.

By applying specially developed adhesive to fibers closed in specially constructed fiber frame [148] the mean attenuation of 0.18 dB was achieved with the loss variation of 0.15 dB. Nevertheless, the refractive index matching adhesive was present on the fiber interface, which was caused by fiber frame construction. The attenuation does not significantly increase after 1000 hours of low and high temperature tests.

For the fiber structure made of silica, HNA and angularly cut fluoride fiber, the connection loss can be as low as 1.2 dB at 1200 nm, when mode field diameter matching fibers and V-grooves are used for fiber adjustment [147]. No significant changes of attenuation during the temperature-humidity tests were reported for the test structures sealed in a specially designed package. The temperature during the tests was varied from -40 to +75 °C and the humidity was kept on constant level of 90 %.

Summarizing, different methods can be used to achieve low connection losses between different fibers. The examples described above rely on using centric and circular fibers, what makes the adjustment procedure easy. Unfortunately the V-groove techniques can not be applied to our fibers and therefore some modified method have to be used.

But before the glue splicing method will be presented let us consider which problems have to be preliminarily solved (or at least taken into account) for optimal performance of the glue-splice. In following sections thermal and mechanical features of silica and fluoride based

will be compared. Also the requirements for glue and their different types will be described.

5.3.1   Thermal and mechanical properties of SiO₂ and ZBLAN glasses

As already mentioned in chapter 2.2, due to glass matrix structure of fluoride based glasses their thermal and mechanical properties differ significantly from that of SiO₂ glasses. Ionic type bindings between heavy-metals forming ZBLAN glasses are shorter and weaker. This results in lower mechanical stability and tendency to crystalize. On the other hand, pure silica based glasses with the structure of the tetrahedron, where every atom of oxygen belongs to two of silicon, show the almost equal mixture of covalent, heteropolar and double π-type bindings [54]. Due to their high bonding energy and the structure of tetrahedrons connected on their apices, the temperatures needed to break the connection of the atoms and soften the glass matrix is much higher. For the comparison optical, thermal, and mechanical parameters of standard ZBLAN and SiO₂ fibers are collected in table 5.4.

Table 5.4: Comparison between ZBLAN and SiO₂ glasses. The composition of ZBLAN glass is: $53ZrF_4 - 20BaF_2 - 4LaF_3 - 3AlF_3 - 20NaF$

property	unit	SiO₂	ref.	ZBLAN	ref.
optical properties					
refractive index (n_D)	-	1.458	[149]	1.497	[150]
UV absorption edge (T=50 %)	nm	180^a	[79]	200^a	[150]
IR absorption edge (T=50 %)	nm	2500^a	[79]	7570^a	[150]
temp. coeff. of n_D (dn_D/dT)	1/K	$+11.9 \cdot 10^{-6}$	[149]	$-14.75 \cdot 10^{-6}$	[149]
thermal properties					
glass transition (T_g)	°C	1175	[149]	256	[150]
crystallization (T_x)	°C	-	-	349	[150]
melting point (T_m)	°C	1734	[151]	450	[150]
expansion coeff. (ζ)	ppm/K	0.55	[79]	17.2	[149]
mechanical properties					
density (ρ)	g/cm³	2.20	[149]	4.33	[149]
Knoop hardness (H)	kg/mm²	600	[149]	225	[150]
Young's modulus (E)	GPa	70.0	[149]	58.3	[149]
Poisson's ratio	-	0.17	[149]	0.31	[150]

Notes:
[a] measured for 1 mm thick glass sample

The comparison shows, that both glass types differ very strongly. The biggest advantage of fluoride-based fibers is their transparency up to the mid infrared. Additionally, similar values of refractive index for both glasses lead to weak Fresnel reflection which is smaller than

0.02 %. Difference in melting points (T_m) of both glasses is higher than 1250 °C and therefore an obstacle for using thermally fiber joining techniques. Also expansion coefficients differ significantly, which has to be taken in consideration during selection of glue used for connecting both fibers. Differences in hardness and Poisson's ratio explain the low mechanical stability of ZBLAN fibers and make their usage as long distance transmission medium impossible.

5.3.2   Requirements for the glue

The right choice of glue is one of the deciding factors for achieving stable low-loss fiber connections. One has to consider how the parts will be connected, on which substrate, and if it will be possible to automatize the glue application process. Also the working temperature has to be taken into account, especially when high optical powers cross the connection points. According to Telcordia specification GR-1221 [152], three key properties are of big importance: glass transition temperature (T_g), outgassing, and environmental test performed in the climatic chamber [153]. For adhesive glass transitions temperature is defined as the temperature at which an adhesive changes its state from glassy and hard to soft and rubbery. High glass transition temperature is not equivalent to better performance, which is the case of cyanoacrylates. The most important features of adhesives used for optical applications are collected in table 5.5. The symbols used in the table correspond to those used in table5.4.

Table 5.5: Comparison of adhesives used for optical applications

property	epoxy	acrylic	silicon	cyanoacrylate	anaerobic
n_D	1.56	1.51	n.a.	n.u.	n.u.
T_g in °C	50-150$^+$	50-100$^+$	< -40	100-130	100-130
ζ in ppm/K	250-400	90-120	250-400	90-120	90-120
shrinkage in %	below 1.5	below 2.25	0-3	5-15	5-13
curing method	heat/UV	UV/dual	UV/moist./heat	heat	oxygen
curing time	v. long	short	moderate	v. short	moderate

Notes:
n.a. - information not available,
n.u. - typically not used in light transmitting paths

The *epoxies* are widely used in optical bonding processes because they minimaly shrink upon cure. Since their curing time is longer than for other adhesives (typically 15 minutes to 2 hours). Nevertheless their high glass transition temperature makes them favorite in fiber optics assemblies. Recently introduced dual-cured (UV and/or heat) suppose to make the automatic applying of the glue possible. They are used often to join dissimilar materials as e.g glass to aluminium.

Acrylics, which are UV-curable, offer very good performance. Due to photo-initiators, which cause immediate start of curing process after applying UV-light, the glue can be cured on demand within short time (2 to 60 seconds). During the curing process photo-indicators split into free radicals. These radicals initiate the formation of polymer chains. In its cured state, the UV acrylics consist of networked polymer chains, which are relatively strong and mechanically stable. Also dually curable (UV + temperature or UV + chemical activators) acrylics are available. Other feature of those adhesives is their long time to get hard, which is advantageous for adjustment of connected parts.

Silicones ensure a robust assembly, but their mechanical properties makes them non usable for very precise, fixed connections. Their broad working temperature range makes them ideal material for sealant. The curing conditions are moderate (time: some minutes, UV, UV + moisture or heat curable), which makes them very good adhesive to connect materials exposed to very high temperature oscillations.

Cyanoacrylates (called also "super glue") can be used for quick and non-demanding connections, but their large shrinkage disqualifies them as a glue for precise fiber connections. Also *anaerobics* seemed to be non suitable for our purposes because of the high shrinkage and large stress induced during curing process occurring due to the exposition to the air.

Since our application is very special and the most important requirements for glue are quick curability, moderate viscosity, low shrinkage after curing and expansion coefficient, which is close to joined fibers - only epoxies and acrylics could be used. Several experiments with cyanoacrylate glues were also performed, but the achieved connection losses were high and they increased with the time, which premised that the stress/shrinkage in the glue points is very high. Therefore in the further investigations only adhesives collected in table 5.6 were used.

Because of the fact, that the glue was applied manually its viscosity played a very important role. When it is too low, the applied glue creep along the fibers, also toward the connecting point. It occurs very quickly, because the distance between the point where the glue is applied and the end of the connected fiber is slightly longer than 1 mm. From the other side, manual dispensing of the glue, which is highly viscose is extremely difficult and in most cases due to the high weight of the glue's drop leads to fiber misalignment. It was found, that the most suitable viscosity of the glue assuring the best trade-off between glue application comfort and its creeping feature is about 1500 cps. Another very important parameter for the glue is its strain during the curing. Preliminary experiments with cyanoacrylates, shown how important it is. Alone during dispensing the glue fluoride fiber started to bend resulting in optical misalignment. Finally, the thermal expansion coefficient of the glue has to be taken in consideration. In the ideal case the thermal expansion coefficient ζ of glue and fibers should be comparable or in the case of joining silica and fluoride fibers it is recommended to chose

Table 5.6: Glues used for the glue splicing experiments

property	TB 3030	OG 169	NOA 61	NOA 65	NOA 68	Wave hv
manufacturer	ThreeBond	Polytec	Norland Product Inc.			SDI
type	resin	epoxy	acrylics			dent. cem.
curable/time	UV/2 min.	UV/6 min.	UV/2 min.			UV/15 sec.
ζ in ppm/K	n.a.	73-156	210			v. low
T_g in °C	n.a.	96	90^a			n.a.
curing strain	high	mod.	mod.	small	mod.	high
viscosity	15000 cps	82 cps	300 cps	1200 cps	5000 cps	v.high

Notes:
^{a} maximum operating temperature according to the specification,
dent. cem. - dental cement,
mod. - moderate,
n.a. - information not available.

glue with ζ equals to mean value of that of both fibers (about 9 ppm/K). Unfortunately, the most proper glue seems to be more sensitive regarding temperature, therefore the changes in temperature can have big influence on the glue-splice's parameters. Among all glues, which were investigated NOA 65 shows small curing strain and together with the moderate viscosity seems to be the best choice for a stable and reliable glue-splice. Unfortunately, during the TDFA operation it was found that at high optical power glue-splices made using NOA 65 only alter very quickly. Therefore, as an additional protection for the connection region, some special dental cement with high viscosity and very low thermal expansion coefficient was used. The test results of fiber connections manufactured using different glues are described in details in chapter 5.4.2.

5.3.3   Application of the glue-splicing technique - setup and procedure

The setup used for glue-splicing, shown in figure 5.3, consists of a laser diode emitting at 1310 nm as a signal source, two adjustment stages, and an optical power meter.

To allow the adjustment of fibers with angled endface cleaves, the left-hand adjustment stage allows to rotate the silica fiber. The right-hand adjustment stage is controlled by piezoelectric actuators to assure precise fiber adjustment in three axes. The air gap between the fiber holders is about 4 to 6 mm. Both fibers were cut with fiber cleaver (FK 12, York), with tension of 180 g in case of the SiO_2 fibers and 80 g for ZBLAN fibers. After adjusting the fibers to maximum output power from the ZBLAN fiber, an additional short piece of silica fiber was applied parallel to the two main fibers. The ends of both fibers were connected to the stabilization fiber by a drop of adhesive (NOA 65) carefully applied to avoid any glue
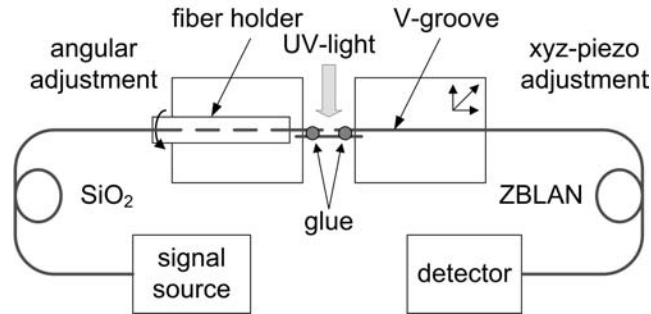
Figure 5.3: Setup of the glue-splice technique used to connect a silica (left) and a ZBLAN fiber (right)

creeping between the fiber endfaces and UV-cured immediately after application. After that, a drop of the highly viscose dental glue was applied on top of the first glue drops to increase the mechanical stability of the connection. Finally the connection zone of the fibers was fixed on a glass substrate and packaged in a stainless steel pipe using again NOA 65 adhesive.

These experiments were done for flat end and angularly cut fibers. The adjustment of the flat end fiber was much more easy because no angular adjustment was needed. Since fiber cores were slightly elliptical the proper adjustment in the case of angularly cut fibers was much more laborious and needed much more time. Manufacturing a single glue-splice for flat end fibers took about half an hour for the glue-splice itself and half an hour for packaging. In the case of angularly cut fibers, the time needed for achieving optimum adjustment was much longer (up to approx. 120 minutes).

5.3.4   Attenuation and reflection of the glue-splice

The attenuation and the reflection of the glue-splice are very important parameters characterizing every connection and making it suitable for its application in amplifier setup. In order to use pump and signal radiation efficiently, the loss of the glue-splice has to be kept minimal. The high reflection caused by air gap between fibers or their misalignment leads to laser oscillations which are common for high amplification levels. Therefore, ideal glue-splice connects two angularly cut fibers with very low loss. The reported reflections of approx. $-60\,\mathrm{dB}$ coming from angularly cut fiber (angle $12°$) assure very good performance of the amplifier [154], but such a large angles are very difficult to achieve. Cutting fiber with large angle could not be achieved with our high precision fiber cleaver, as shown in figure 5.4.

The experiment was performed for both types of fiber and the set angle was $10°$. The fibers were cut with optimized tensions,which differ slightly from that used for flat end cuts (200g for SiO_2 and 80g for ZBLAN). The angles were measured using the according facility of a fusion splice device. While the results for standard silica fiber (SMF-28) show the homogeneous distribution, the results achieved for ZBLAN show slightly bigger discrepancies
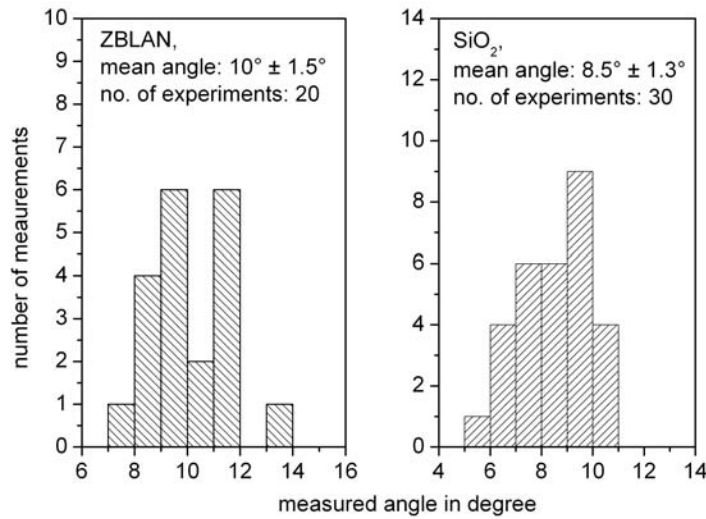
Figure 5.4: Measurements of cut angle for ZBLAN and SiO$_2$ fibers. Set angle was 10 °

and their distribution is inhomogeneous. On the other hand, the average value of the cutting angle achieved for ZBLAN fiber agreed very well with the set value, which was not the case for SMF-28. It is also worth to notice, that the quality of the fiber endface after cutting was in almost 50 % of the measured fibers not satisfying for any type of fiber. The measurements for set angle of 5 ° shown better performance of fiber cleaver (experiment was performed for 20 test cuts for each fiber type). The mean value of angle and its standard deviation were 4.9 ° and about 0.5 ° respectively, for both types of fibers. The side view of silica fiber cut with 15 ° set angle is shown in figure 5.5. The picture was captured from the fusion splice device, which was used to observe the fiber endfaces. For the comparison also the side view of the flat end fiber is shown on the right hand side of the figure. The observation surfaces are perpendicular to each other and labelled as "X" and "Y". While the right fiber shows very smooth and regular endface, the shape of the left one is not satisfying. Non-regular edge of the fiber interface indicates difficulties with connecting two fibers cut with the same angle, especially, because of the fact, that the quality (and shape) of each fiber end differs from cut to cut. The side view of the fiber helps to decide about the quality of the cut and makes possible to forecast the possibility to achieving good fiber connection, however it is not only criterion. A lot information one can gain looking into the fiber endface. Some of them were shown in figure 5.6.

The endface of the silica fiber cut without any angle (figure 5.6a) is smooth and homogene. When cleaving with some angle (here 10 °) the fiber brakes less fine, which results in scratches shown in lower part of the figure 5.6b. The same was observed for cutting ZBLAN fibers.
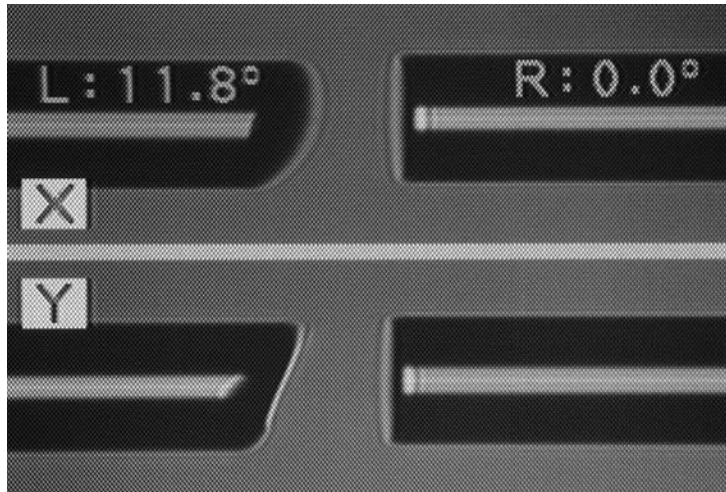
Figure 5.5: Side view of two silica fibers cut with different set angles: 10° (left) and flat end (right)
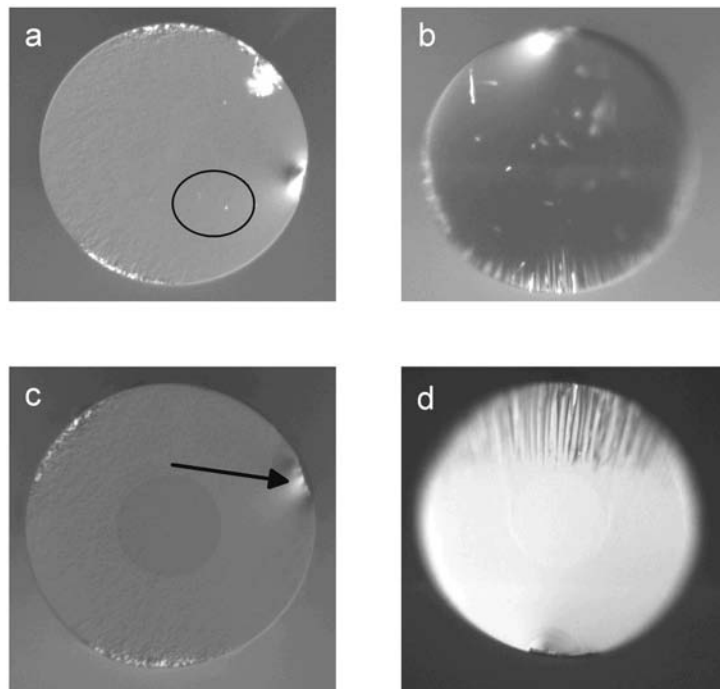
Figure 5.6: Fiber interfaces for different cut angles: (a) SiO_2 flat end, (b) SiO_2 10°, (c) ZBLAN flat end, (d) ZBLAN 10°

The endface of the flat end fiber looks very well, which is not the case for the fiber cut with the angle of 10°. On the fiber cross-sections, except of the blade's trace (arrow on the figure) one can see also rests of the glass. Due to the fact that the silica glass is brittle, after cutting it small pieces of glass form, which stay on the surface. This can cause the problems with the thermal stability of the glue-splices. Since this problem is very important issue for the TDFA it was discussed in details in section 5.4.3.

Since it is difficult to obtain usable fiber endfaces cleaving the fiber with non-zero set angle, the information about the requirements for the angle of the endface is of big importance. To estimate how critical is it the reflection dependency on the cutting angle was investigated. The setup used for this measurement is shown in figure 5.7 and the results are shown in figure 5.8.
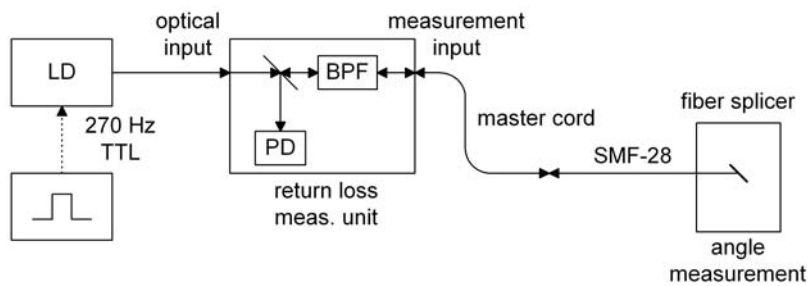
Figure 5.7: Setup for the measurement of reflection from angularly cut SiO_2 fibers

The measurement setup consists of laser diode, which is modulated by rectangular signal with frequency of 270 Hz, optical power meter featured with the return loss unit, and the fiber splice device. The measurement procedure is divided in three steps: condition setup, reference reflectance measurement, and actual measurement. It is extremely important to keep the power coming out from light source constant during the measurement. The tunable laser source, emitting the optical radiation in the wavelength region from 1390 to 1540 nm, can be modulated only when working in the constant current mode. This cause significant power changes and makes this sensitive measurement impossible. For that reason we used the semiconductor laser diode emitting at 1547 nm. The modulated radiation was connected to return loss measurement unit (AQ7310, Ando), which divides it into two paths. One of them was directly converted to electric signal, amplified and recorded as a reference. Another part of radiation was coupled to the silica pigtail via a master cord with the known reflection. The intensity of radiation reflected from the end of the fiber pigtail cut with a certain angle was compared with the radiation coming directly from the light source. The band pass filter (BPF) with a center frequency of 270 Hz in reflection measurement unit assures the detection of the

usable signal and is used to eliminate the unmodulated noise radiation. On the opposite site of the setup, the fiber splicing device was used to determine the actual angle of the fiber endface. For an easier interpretation of the results, the values measured in dB were recalculated into percents and shown together as the function of the angle in figure 5.8.
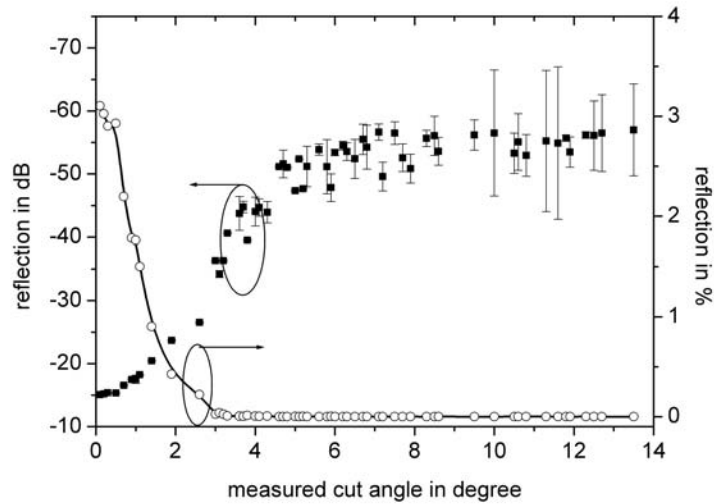
Figure 5.8: Reflection from the fiber end as a function of the measured cut angle

The investigations based on 120 fiber cuts (in total) were performed for 4 set angles of 0, 5, 10 and 15°. The tension was kept constant and its value was 200 g. After cutting with a set angle, the actual angle was measured with the fiber splicing device. It is not surprising, that the reflection values scatter only a bit for small cutting angles. High repeatability of the cuts result in very small standard deviations of the measurements, which are lower than 0.15 dB. Also the endface quality observed during the angle measurement was in most cases well, its front surface was regular and clear. By increasing the angle, it was found that the quality of the endface deteriorates and the measured angles and their reflections scattered significantly. For the fibers cut with an angle larger than 5°, the measured reflection exceeds -50 dB (less than 0.2 %). Unfortunately, due to bad surface one could not expect low-losses when two fibers cut with this angle are joined.

Therefore a lot of effort was made to achieve very good glue-splice for angularly cut fibers with the angle of approx. 8°, which is the largest possible angle assuring best tradeoff between low reflection from the fiber end and repeatability of the fiber cleaver. Nevertheless, flat end connections were preferred because of their manufacturing, which is easier. Histograms in figure 5.9 show the statistics of glue-splices realized with flat end and angularly cut fibers.
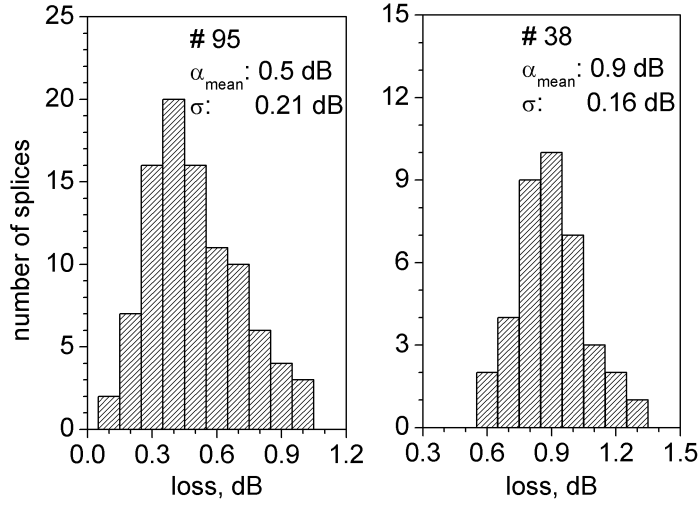
Figure 5.9: Measured loss of glue-splices for flat (left) and angularly cut fibers (right)

The mean attenuation for glue-splices made for flat end fibers was found to be about $0.5\,\mathrm{dB}$ and it was about $0.4\,\mathrm{dB}$ smaller than in case of fibers with angular fiber ends. This may be contributed to the more involved adjustment procedure and the accuracy of the angled cleaved end. The larger attenuation for connecting the angularly cut fiber is also not surprising since it can be expressed as:

$$\alpha_{total}^{dB} = \alpha_{MFD}^{dB} + \alpha_{r}^{dB} + \alpha_{l}^{dB} + \alpha_{\angle}^{dB} \ , \tag{5.6}$$

where α_{MFD}^{dB} represents losses caused by mode field diameter mismatch, α_{r}^{dB} describes losses caused by radial shift of both fibers, α_{l}^{dB} are losses cased by longitudinal shift of the connected fibers, and finally $\alpha_{\angle}^{dB}$ represents losses coming from angular misalignment. Their influence on the total attenuation of the connection is different, nevertheless, the most critical for connecting of angularly cut fibers are losses caused by differences in endface's angles. According to [154], for two similar fibers they can be estimated as:

$$\alpha_{\angle}^{dB} = \exp\left(-\frac{\sin^2 \Theta}{\tan^2 \Theta_D}\right) \ , \tag{5.7}$$

where Θ, is the mismatch angle, and Θ_D is the acceptance angle of the fiber. It depends on the refractive index n, core diameter r, and the operating wavelength λ and is defined as:

$$\Theta_D = \frac{\lambda}{\pi n r} \ . \tag{5.8}$$

According to this equation, $1°$ difference in the angles of the fiber ends leads to attenuation of approx. $0.5\,\mathrm{dB}$, what demonstrates how important is a well matching of the cut angles. Nevertheless, the average attenuation of $0.9\,\mathrm{dB}$ measured for angularly cut fibers seems to be very low and was found to be acceptable for further investigations.

5.4   Durability tests

Since glue-splices are integral part of TDFA, it is of fundamental importance to ensure their good performance over long time. The ideal connection should be low-loss and does not change its properties (attenuation, reflection) during the time. Therefore durability tests are very important and they are suitable to characterize glue-splicing method and to improve it. In the following chapters low and high power durability test will be described. In the last section we will focus on thermal issues of the glue-splices and try to present some improvement suggestions for more stable glue-splices.

5.4.1   Low power measurements

Because the long-term stability of the fiber connection is of great importance for the thulium-doped fiber amplifier, lifetime tests were performed using a couple of test devices consisting of about 1 m of ZBLAN fiber connected to pigtails of silica fiber at both sides as in the setup shown in figure 5.10.
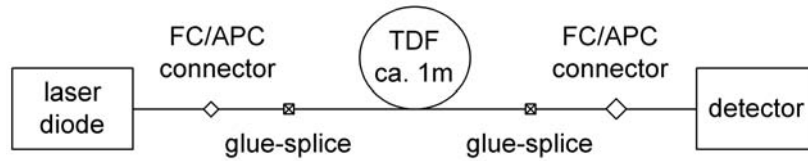
Figure 5.10: Setup for lifetime measurements of glue-splices at low optical power

The setup consists of a laser diode emitting $-4\,\mathrm{dBm}$ power at $1310\,\mathrm{nm}$, an optical power meter, and the test device placed between them. For these experiments glue-splices made with adhesive NOA 65 and standard thulium-doped fiber (core diameter of $4\,\mu\mathrm{m}$, numerical aperture is 0.16) were used. Three of seven test devices were additionally stressed by shaking them manually before each measurement. The loss of an individual glue-splice was calculated according to the following equation:

$$\alpha = \frac{P_{in} - P_{out} - L \cdot \alpha^*_{ZBLAN}}{2} \ , \tag{5.9}$$

where P_{in} and P_{out} are the input and output power, L is the fiber length and α^* is the attenuation of the ZBLAN fiber in dB/m. The splice losses of the test devices for the lifetime

test were in the range 0.40 - 0.55 dB and were found to be constant with respect to the measurement accuracy of 0.1 dB during the test period of almost 700 days in the case of the oldest devices. The results of these tests are shown in figure 5.11.
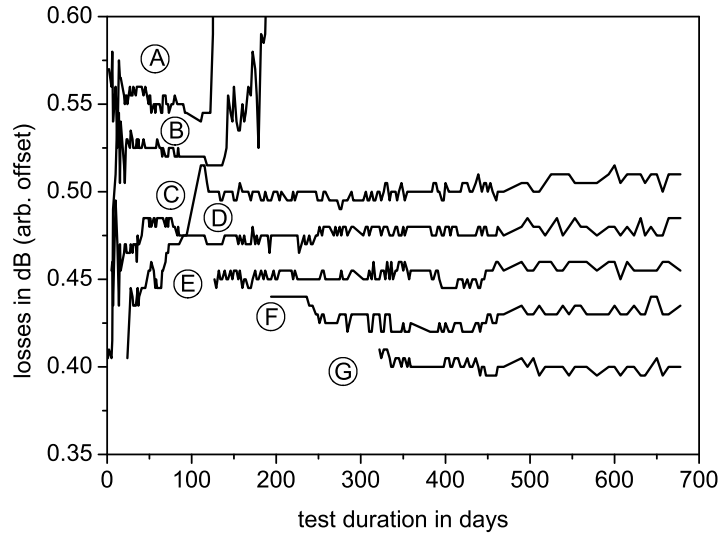
Figure 5.11: Results of lifetime measurements of glue-splices at low optical power

The value of actual loss for every connection is not critical as long as it is constant during the test period. Therefore the y-axis was arbitrarily shifted to show the loss evolution. The ripples shown on the beginning of the test may be due to non optimized measurement method and they decrease after approx. the first 50 days. The structures exposed to the mechanical stress (C, D and G in figure 5.11) did not exhibit extra losses caused by their special treatment, and their measured loss stayed constant, which may result from very carefully made glueing and packaging process. Two test structures were destroyed accidentally, but other structures survived this long-time test, and their losses are measured continuously every two weeks.

5.4.2   High power measurements

In usual applications the glue-splice must transmit high pump or signal powers, which are concentrated in the very small core of the active fiber. This leads to significant thermal effects at the interface between both fibers, which were investigated using the setup shown in figure 5.12.

The setup consists of a pump diode emitting 160 mW at 1055 nm connected to the flat cleaved glue-splice under test via a 75 % fiber coupler. The open port of the fiber coupler and
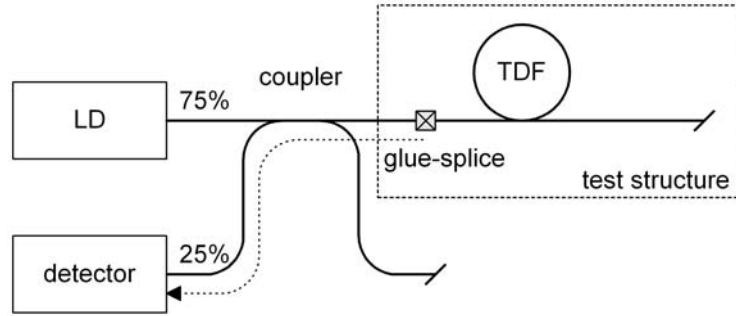
Figure 5.12: Setup for lifetime measurements of glue-splices under high optical power operation

the end of the ZBLAN fiber were cleaved angularly to suppress any reflections from the fiber ends. Because the thulium-doped ZBLAN fiber was absorbing at 1055 nm, this setup records the reflection at the glue-splice instead of the transmission. The 4 % reflection was equivalent to the reflection caused by air gap between silica and fluoride fiber what represents the failure of the test structure. In the praxis this was observed very rare, in most cases the fibers where pushed towards each other, resulting with the increasing of the detected reflected power. The thulium-doped ZBLAN fibers excited 1055 nm laser diode emit strong blue fluorescence, which intensity was used as the indicator for the condition of the structure.

For the enhancement of the lifetime of the glue-splices different glues, curing times and their combinations were investigated. The life time enhancement may be clearly seen in figure 5.13 showing the example of a measurements for four test structures.

The manufacturing parameters of the structures (glue used for connecting of the fibers and its curing time) are collected in table 5.7.

Table 5.7: Parameters of some test structures used for high power lifetime test

number	glue	curing time
#4	NOA 65	2 min.
#6	NOA 65	6 min.
#7	OG 169	6 min.
#9	NOA 65 + Wave hv	2 min. + 1 min.

It was found, that for relatively short curing times of NOA 65, which became our standard glue, the structures did not stay low-loss over the long time. After several hours of low reflection the reflected power increased constant to the point of destruction of the structure. The lifetime of the structure could be slightly improved by increasing the curing time from 2 to 6 minutes. Using OG 169, which was less viscose and therefore more difficult to apply
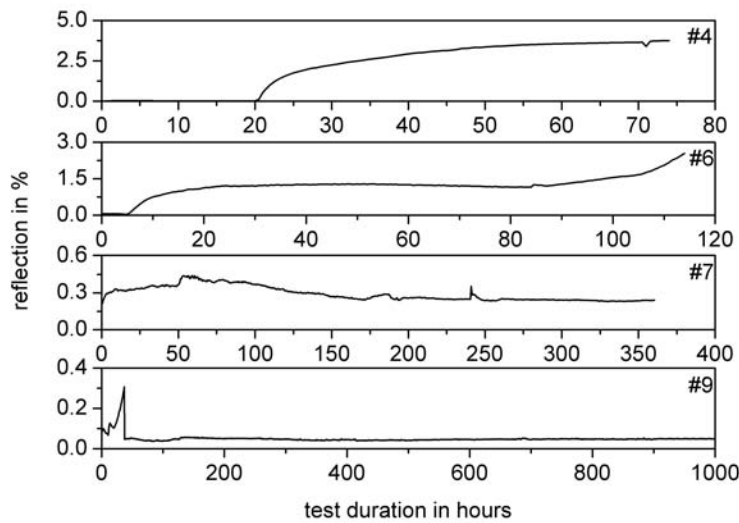
Figure 5.13: Results of lifetime measurements of glue-splices at high optical power

in controllable way, it was possible to achieve more than 350 hours of the lifetime with a low reflection. The best structure survived more than 1000 hours and after that the test was interrupted in order to perform other tests. The reflection characteristic shows that for structure #9 due to thermal effects, the reflection increased in the first 40 hours of the test, but after that it dropped down below 0.05 % and stayed constant until the test was stopped.

The photograph of a glue-splice (figure 5.14) which did not survive the high power measurement test shows that the connection interface between both fibers aged during the test period and became dark. Furthermore it seems that in this case some material, which could be some glue or glue solvent, is swelling out of the fiber interface, therefore the investigations concerning thermal properties of glue-splices became very important.

5.4.3 Thermal stability of the glue-splices

Since thermal properties of the silica and ZBLAN fiber differ significantly, the stability of the glue-splice is an important issue. Our experiments show, that the time to damage of the fiber connection depends on the power going through it. From the other side, the photos of the destroyed structures show sometimes large deformation of the fluoride fiber. This is an indicator, that the temperature at the connection place exceeds the melting point of the ZBLAN glass. This can be caused by the absorption of the incident power on the impurities present on the endface. They are rests of the glass firmed during the cut process as it was shown in figure 5.6 c. In the glue-splice they act as a absorption centers causing local warming up of the ZBLAN fiber. When the temperature exceeds T_x the crystals start to
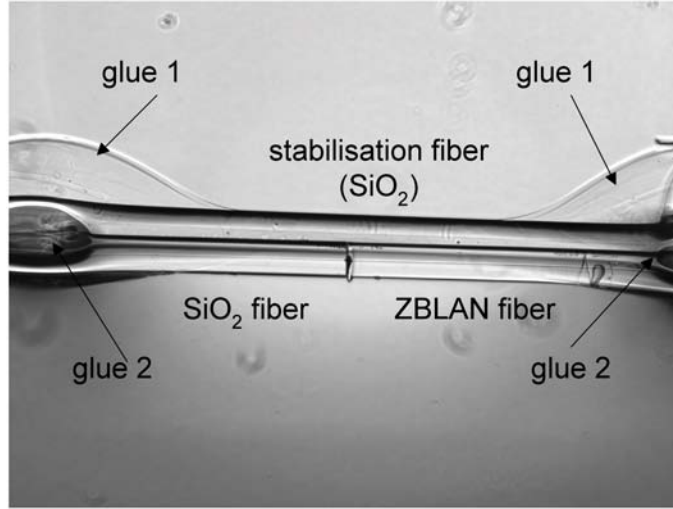
Figure 5.14: Photograph of the glue-splice after 1000 hours of high power exposure

form, which leads to even stronger power absorption and softening of the fiber. Finally, the optical radiation can not be guided through the glue-splice which is equivalent to its failure. Since the thermal expansion coefficient ζ of fluoride glass is more than 30 times larger than that of SiO_2 the thermally induced changes can be observed in fact mainly in the ZBLAN. The attenuation caused by the increasing dimensions of the fluoride fiber is equivalent to the loss caused by radial shift calculated as:

$$\alpha_r^{dB} = 10 \, \log \left(\exp^{(\frac{2s}{MFD})^2} \right) \, , \tag{5.10}$$

where s is the radial shift and MFD is the mode field diameter of the ZBLAN fiber. Assuming 250 K temperature increase, the α_r^{dB} achieves 0.0004 dB. This value is negligible for the total attenuation of the fiber connection. On the other hand, this temperature causes significant longitudinal shift of the fluoride fiber of about 9 μm. Since both SiO_2 and ZBLAN glasses are fixed to the additional piece of silica fiber, as shown in figure 5.15 without any gap between, it is important to note, that this gap has to be formed already during the manufacturing of the glue-splice. After switching on the pump power, the fluoride fiber change its dimensions, move toward the silica fiber and touch it. The initial fiber separation of approx. 9 μm cause relatively high attenuation (approx. 2.2 dB) calculated according following equation [155]:

$$\alpha_l^{dB} = 10 \, \log \left(1 - \frac{2 \, NA \, x}{3 \, d} \right) \, , \tag{5.11}$$

where x are the distance between both fibers, NA and d_{core} is the numerical aperture and the core diameter of the ZBLAN fiber respectively. On the other hand, leaving no space
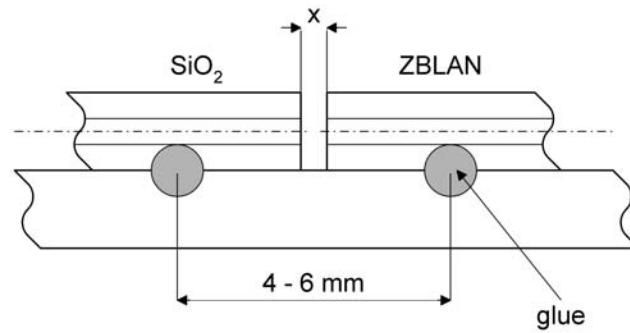
Figure 5.15: Setup for thermal analysis of the glue-splice

between fibers leads to deformation of the ZBLAN fiber and low lifetime of the glue-splice. Nevertheless, one has to note, that the automatic thermal ZBLAN fiber adjustment has to be performed very accurate, because the thermal effects lead to increasing the whole volume of the fluoride fiber. Therefore this fine changes of the fiber geometry have to be controlled very precisely.

Since the thermally stable glue-splices are very important for fiber lasers and amplifiers some suggestion can be given to improve their performance. One of them is the problem of ideally clean fiber endface, which can be achieved by applying ultrasonic bath, another concerns forming of the buffer air gap between the fibers. Both of them make the manufacturing process longer and more complicated, but in this way one can expect the enhancement in the lifetime of the glue-splices.

6 Numerical TDFA model

Since rare-earth doped fiber amplifiers became a key component of optical transmission systems, numerical simulations of the amplifier's performance started to be indispensable. The amplifier model acts as a helpful tool during the design process, it helps to understand the processes, which play a role in the amplification process and finally, it can be used to find out the optimal device parameters and predict the performance of the whole system. Several rare-earth doped fiber amplifier models were presented [156–160] mostly for erbium- or praseodymium-doped fiber amplifiers. They base on the rate and gain equations but they significantly differ in their complexity. To shorten the computing time, some models neglect the amplified spontaneous emission (ASE) or do not consider the excited state absorption (ESA) [158]. Nevertheless, the results of the simulations based on such a simplified model can not fully describe the somehow complex operation of the rare-earth fiber amplifier.

For the erbium-doped fiber amplifier (EDFA) it was shown that the best match between measurement and simulation was achieved for applying the Giles model [159, 161, 162], which provides a full spectral solution. The propagation equations are integrated back and forth along the fiber until the solution converges. It provides a high accurate solution of the rate equations, but it takes longer computing time therefore this model should be used for accurate calculations.

The model of the praseodymium-doped fiber amplifier (PDFA), presented in [160], does not take into account any simplified assumptions and includes modelling of the the nonlinear effects in the amplifier. This radially resolved model calculates not only the spectral gain but also noise figure.

The EDFA and PDFA models in the meantime are standard part of the commercially available software for analyzing optical transmission systems, which is not the case for the TDFA. Since they are not present in optical transmission links yet, there is no necessity to model them. Nevertheless, with increasing interest for long-haul high-bitrate systems, the problem of the amplifier's performance simulation will occur. Several attempts to model the TDFA were reported [103, 163, 164] and similarly like in the case of EDFA and PDFA they differ from each other in their complexity.

A very simple model of TDFA presented in [163] takes into consideration only some spectroscopic data such as pump ground state absorption centered at 1210 nm, multiple excited state absorption $^3F_4 \rightarrow ^3F_{2,3} \rightarrow ^1G_4$, signal stimulated emission by the signal wavelength, and additional emissions at 800 and 1800 nm. The spectroscopic data (absorption, emission and multi-phonon decays) are literature values. In this simplified model the amplified spontaneous emission at the signal wavelength range is not included.

A different method to predict the TDFA performance was presented by the group of A. Rieznik [164]. They developed a black-box model delivering information about the gain and ASE at any wavelength using the measurements of three spectral tilting functions and gain at two reference wavelengths. The TDFA is considered as 3-level homogeneously broadened system consisting of the levels $^3H_6$, $^3F_4$ and $^3H_4$ with a negligible population of other energy levels. The gain of the amplifier is given as the function of absorption and emission cross-section weighted with the population number of the proper energy level and the total losses of the amplifier. Measuring the gain of the amplifier for different saturating conditions (high signal power or high pump power) the tilt functions can be evaluated and further used to calculate the gain and ASE at any wavelength. This makes that model very easy and quick regarding the computation time, but does not help to understand the physical background of the amplification process. Nevertheless, it is a powerful tool for quick and easy amplifier simulations.

A more advanced TDFA model is described in [103]. It is optimized for a silica-based fiber amplifier and employs each significant ground- and excited-state absorptions as well as every strong enough emission lines involving the energy levels from the basic up to the high lying $^1G_4$ level. Due to the high non-radiative decays from the $^3F_{2,3}$ and $^3H_5$ level, their population is negligible and they are not decisive for the amplifier performance. The gain of the amplifier can be calculated by solving the spectrally and spatially resolved rate- and gain-equations. Compared to other models, the power of each forward and backward propagating wavelengths present in the amplifier setup is described as the combination of ground- and excited-state absorption as well as amplified spontaneous and stimulated emission. The propagation- and rate-equations are solved along the fiber using Runge-Kutta-Gill method of the fourth order. The model uses the spectroscopic data chosen from the literature or calculated using Judd-Ofelt theory and the comparison of the simulation results with the measurements published in the literature show only qualitative agreement. The discrepancies were attributed to some simulation parameters, which were not published in the compared reference.

It is obvious, that the performance of the amplifier only to a certain degree depends on the parameters of the passive components. They can slightly modify the gain spectrum or change the output signal power, but the amplification occurs in the active fiber, therefore the core of the model is the mathematical description of the rare-earth doped fiber. The model used by the author is based on the fiber laser model from [58]. It describes the thulium-doped fiber itself and was created as a two port amplification module, which can be used in the commercial simulation software OptiAmplifier®. The experiences with EDFA simulations performed with that software, its intuitive graphical user interface and ability to enhance the database of standard elements of the fiber transmission link were the motivation to use the OptiAmplifier® to simulate the topology of the amplifier setup, but the most complex part of the amplifier stays the thulium-doped fiber.

6.1   Simulation parameters

Before we proceed with the mathematical formulation of the model, let us first summarize all required parameters. One may divide them into five groups as shown in figure 6.1.
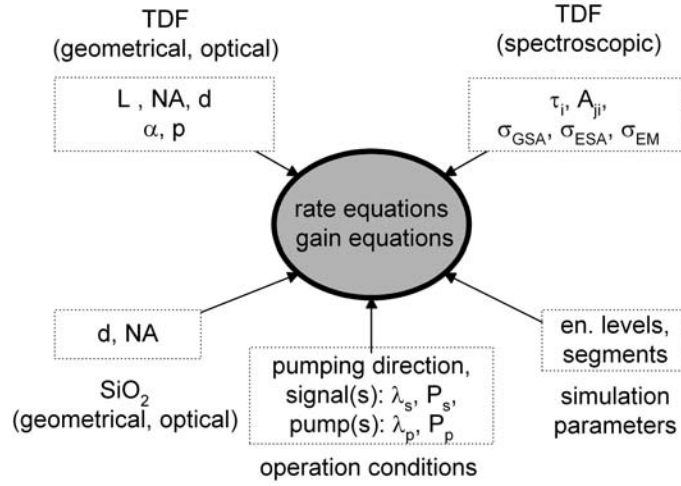
Figure 6.1: Parameters used in the TDFA model

In the first group, the geometrical and optical parameters of the active fiber are collected. They include the length L of the active fiber, its numerical aperture NA, core diameter d, attenuation α, and thulium concentration p. The complement of these parameters are spectroscopic data assigned as ground-state and excited-state absorption as well as emission cross-sections (σ_{GSA}, σ_{ESA} and σ_{EM}). The lifetimes of the proper energy levels τ_i and the emission rates A_{ji} are the last parameters in this group. In our simulation we assume the TDF module consisting of the active fiber and the SiO_2 pigtails on its both ends, therefore the core diameter d and the numerical aperture NA of the silica fiber are necessary to calculate the reflections on the connection point. As a next group, the operation conditions of the fiber amplifier are used. In this group the pumping directions, and signal and pump properties are included. Finally, the number of energy levels considered in the calculations and the number of TDFA segments in which the equation should be solved describe the general parameters of the model. Almost each of the previously described parameters was measured, except the emission radiative rates A_{ji} calculated by R. Caspary [58].

6.2   Model description

The model used for the TDFA simulations uses the Matlab® software, it is based on a fiber laser model, described in details in [58]. It simulates the performance of the amplifier in

the steady-state case. Since the amplifier is simulated numerically, the general equations describing its performance have to be given in their discrete form. The calculations have to be performed in three combined domains: energy levels, wavelengths, and spatial position. In other words, the TDF is divided in several segments, for which the occupation numbers of energy levels are calculated and the change in absorption and/or emission is evaluated. It is important to note that the indices i and j are used for energy levels, k is the index corresponding to wavelength and x denotes the position along the active fiber.

Since we consider amplifier in steady-state, we assume no change in the occupation number n of any energy level i, which corresponds to:

$$\frac{dn_i}{dt} = 0 \; . \tag{6.1}$$

Introducing the photon flux $\Phi(\nu)$ defined as the number of photons per unit area and per unit time interval, the rate equation for level i in the fiber segment x can be given as:

$$
\begin{aligned}
0 = \frac{dn_i}{dt} = &\sum_j \left[A_{ji} + W_{ji} + \sum_k f_k(\Phi_{kx}^{\rightarrow} + \Phi_{kx+1}^{\leftarrow})\sigma_{jik} \right] n_{jx} \\
&- \sum_j \left[A_{ij} + W_{ij} + \sum_k f_k(\Phi_{kx}^{\rightarrow} + \Phi_{kx+1}^{\leftarrow})\sigma_{ijk} \right] n_{ix} \; ,
\end{aligned}
\tag{6.2}
$$

where A_{ij} is the emission radiative rates, W_{ij} denotes the multiphonon non-radiative emissions rates and n_i is the relative occupation number of the energy level i. In our calculation the direction of the photon flux Φ plays an important role. Assuming the segment number x, $\Phi_{kx}^{\rightarrow}$ describes the flux leaving the previous fiber segment into the segment x, whereas $\Phi_{kx+1}^{\leftarrow}$ denotes the flux travelling in the opposite direction from the following segment $x + 1$. The sums in equation (6.2) correspond to change of the local occupation number of level i caused by transitions ending in level i (first sum) and beginning in level i (second sum). In fact, the first sum increases n_i, while the second sum is reducing it. The symbol f_k denotes the confinement factor defined as the ratio of the radiation field affected by the fiber core [58].

Equation (6.2) can be simplified formally by grouping the spontaneous radiative and non-radiative rates in a matrix B_{ij}^{sp} and defining a matrix B_{ijk}^{st} for terms of absorption and stimulated emission. They are given as:

$$
B_{ij}^{sp} = \begin{cases} -\sum_{j'} (A_{ij'} + W_{ij'}) & \text{for j = i} \\ A_{ji} + W_{ji} & \text{otherwise,} \end{cases}
\tag{6.3}
$$

and

$$
B_{ijx}^{st} = \begin{cases} -f_k \sum_{j'} \sigma_{ij'k} & \text{for j = i} \\ f_k \sigma_{jik} & \text{otherwise.} \end{cases}
\tag{6.4}
$$

The system of N energy levels is described by N rate equations, which are not linearly independent. In order to solve the set of the rate equations we exchange the rate equation for the ground level ($i = 0$) with the following formula:

$$\sum_i n_i(x) = 1 \ . \tag{6.5}$$

When the incoming and outgoing photon fluxes are known, the cumulative matrix B_{ijx} can be calculated as:

$$B_{ijx} = \begin{cases} 1 & \text{for i} = 0 \\ B_{ij}^{sp} + \sum_k B_{ijk}^{st}(\Phi_{kx}^{\rightarrow} + \Phi_{kx+1}^{\leftarrow}) & \text{otherwise.} \end{cases} \tag{6.6}$$

The rate equations in the fiber segment x are now just a set of linear equations

$$\sum_j B_{ijx}\, n_{jx} = \begin{cases} 1 & \text{for i} = 0 \\ 0 & \text{otherwise,} \end{cases} \tag{6.7}$$

which have to be solved to get the relative occupation number n_{jx} for any energy level j in the fiber segment x.

Solving the rate equations we obtain the relative occupation of the energy levels, which are the input values for the more complicated gain equation. For the photon flux travelling from left to the right the gain equation can be written as:

$$\frac{\Phi_{kx+1}^{\rightarrow}}{\Delta x} = w_k \sum_{ij} A_{ij} g_{ijk} n_I n_{ix} + \Phi_{kx}^{\rightarrow} \left(f_k \sum_{ij} \text{sign}(i - j)\sigma_{ijk} n_I n_{ix}\Delta x + 1 - \alpha_k \Delta x \right) \tag{6.8}$$

and for the flux travelling in opposite direction:

$$\frac{\Phi_{kx}^{\leftarrow}}{\Delta x} = w_k \sum_{ij} A_{ij} g_{ijk} n_I n_{ix} + \Phi_{kx+1}^{\leftarrow} \left(f_k \sum_{ij} \text{sign}(i - j)\sigma_{ijk} n_I n_{ix}\Delta x + 1 - \alpha_k \Delta x \right) \ , \tag{6.9}$$

where Δx is the fiber segment's length, g_{ij} is the normalized lineshape function, w_k is the fraction of the total spontaneous emission guided by the fiber core, n_I is the thulium density and α_k denotes the summarized fiber's background losses. The fraction of the total spontaneous emission guided by the fiber core depends on the numerical aperture of the thulium-doped fiber. It can be interpreted as a part of a full solid angle spanned by the acceptance angle of the fiber with given numerical aperture. Since the definition of the acceptance angle is correct only for multimode fibers, this definition is not fully correct. The w_k can not be determined more accurate, therefore for its mathematic description we use following equation:

$$w_k = 0.5\ (1 - \cos(\arcsin(NA)))\ . \tag{6.10}$$

For the fibers used in the amplifier setups the w_k was as small as 0.02 for high NA thulium-doped fiber and 0.006 for the TDF with the *NA* of 0.16.

The relatively complicated equations (6.8) and (6.9) can by simplified by creating matrices collecting all the known parameters of the spontaneous emission G_{kxi}^{sp}, absorption and stimulated emission G_{kxi}^{st} and background losses G_{kx}^{att}. These parameters are given by:

$$G_{kxi}^{sp} = w_k n_I \Delta x \sum_j A_{ij} g_{ijk} \; , \tag{6.11}$$

$$G_{kxi}^{st} = f_k n_I \Delta x \sum_j sign(i - j)\sigma_{ijk} \; , \tag{6.12}$$

and

$$G_{kx}^{att} = -\alpha_k \Delta x \; , \tag{6.13}$$

for $\alpha_k > 0$. Together with the occupation numbers n_{ix} calculated from the rate equations for fiber segment x, the photon fluxes can be calculated as:

$$\Phi_{kx+1}^{\rightarrow} = \sum_i G_{kxi}^{sp} n_{ix} + \left(1 + G_{kx}^{att} + \sum_i G_{kxi}^{st} n_{ix}\right) \Phi_{kx}^{\rightarrow} \; , \tag{6.14}$$

and

$$\Phi_{kx}^{\leftarrow} = \sum_i G_{kxi}^{sp} n_{ix} + \left(1 + G_{kx}^{att} + \sum_i G_{kxi}^{st} n_{ix}\right) \Phi_{kx+1}^{\leftarrow} \; . \tag{6.15}$$

Since the amplifier setup consists of both silica and fluoride fibers, the reflection caused by the mode field diameter mismatch R_k^{MFD} has to be taken into consideration. Moreover, the recirculation of the radiation, which takes place in the fiber ring laser used in one of the pumping schemes has an influence on the photon fluxes in the first $\Phi_{k1}^{\rightarrow}$ and last $\Phi_{km}^{\leftarrow}$ of the fiber segments. The boundary conditions modify the photon fluxes according to the following equations:

$$\Phi_{k1}^{\rightarrow} = (1 - CR_k^L)\, T_k^{MFD}\, \Phi_k^{L\rightarrow} + R_k^{MFD}\Phi_{k1}^{\leftarrow} + CR_k^L\, CR_k^R\, (T_k^{MFD})^2\, \Phi_{km}^{\rightarrow} \; , \tag{6.16}$$

and

$$\Phi_{km}^{\leftarrow} = (1 - CR_k^R)\, T_k^{MFD}\, \Phi_k^{R\leftarrow} + R_k^{MFD}\Phi_{km}^{\rightarrow} + CR_k^L\, CR_k^R\, (T_k^{MFD})^2\, \Phi_{k1}^{\leftarrow} \; , \tag{6.17}$$

where $T_k^{MFD} = 1 - R_k^{MFD}$ represents transmission through the connection formed by fibers with different mode field diameters and CR_k^L and CR_k^R correspond to the coupling ratio for the left and right fiber coupler forming the fiber laser cavity. The fluxes $\Phi_k^{L\rightarrow}$ and $\Phi_k^{R\leftarrow}$ enter the fiber amplifier from the left and right side, respectively. They represent any kind of radiation like pump, signal or amplified spontaneous emission. The quantities described above
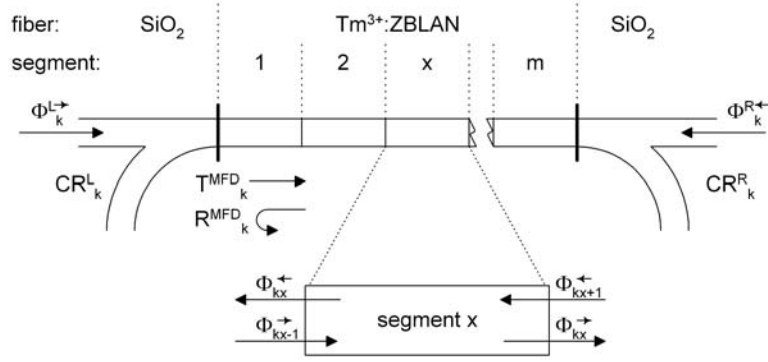
Figure 6.2: The assignment of the photon fluxes in the amplifier's model

are collected in figure 6.2.

Since the processes occurring in the fiber amplifier are already described in form of rate and gain equations, the only thing missing is the proper algorithm to solve the rate and gain equations and to predict the performance of the amplifier. The amplifier model can be divided in three layers schematically shown in figure 6.3 and the algorithm is included in the kernel. But before we describe it let us start with the outer layer, which is used as an interface between the user and the model. It is used to load such parameters as length and thulium concentration of the active fiber as well as signal and pump powers and wavelengths in any pumping configurations. The output results of the simulation in form of gain and signal-to-noise ratio (single values or graphs) are also calculated in this layer.

As next, the input data are combined with the spectroscopic parameters of the amplifier, which occurs in preparation layer. In the next step the input radiation is split into pump, signal and ASE bins and the initial photon fluxes are created. Every bin is characterized by its individual wavelength and power. This wavelength grouping is convenient in many cases, for example when the total ASE power has to be calculated, the simulation kernel, however does not make any difference between different types of wavelength bins. In the next step reflection caused by MFD mismatch between silica and fluoride fiber is calculated. The spectroscopic properties of thulium in fluoride glasses like absorption and emission cross-sections or lifetimes of the proper energy levels are used to calculate the help matrices described above in equations (6.3), (6.4) and (6.11) - (6.13). In the kernel the rate and gain equations are solved for every fiber segment. In the first step, the relative occupations for every energy level are calculated. They are necessary to further calculate the photon flux $\Phi_k^{\rightarrow}$ coming into the next fiber segment. This calculation is repeated as long as the photon flux in the last segment is calculated. After that, the $\Phi_{km}^{\leftarrow}$ is calculated according to equation (6.17). Since the left-to-right travelling flux is already calculated, the flux travelling in the opposite direc-
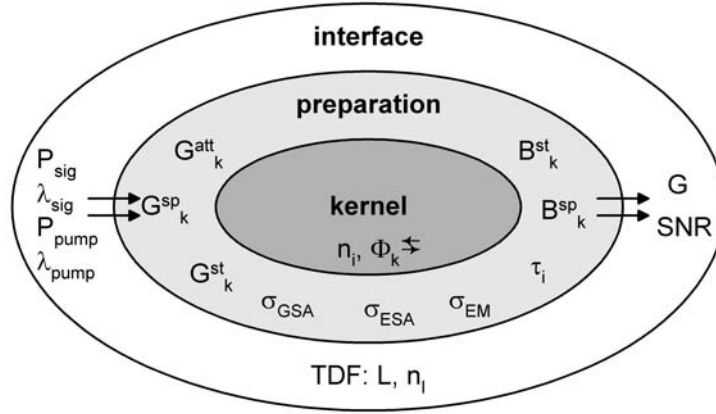
Figure 6.3: The layer structure of the TDFA model

tion is calculated using the same method. Both fluxes are calculated as long as the system converges, and the difference between actual and previous iteration is negligible. Since the TDFA is a complicated amplification system with many ASE bands accompanying the signal stimulated emission, special attention has to be paid to define the convergence parameter. This problem was described in more details in [58].

In the following sections, simulation results for three amplifier configurations will be presented. We will start with the simulation of the double-wavelength pumped gain shifted TDFA with the pump configuration 805 nm+1056 nm. As a second example we will report the simulation results for single-wavelength 1056 nm pumped TDFA using cross-relaxation leading to large gain in highly thulium-doped fibers. Finally, an advanced TDFA setup with co-operatively working fiber laser at approx. 1900 nm will be presented.

6.3   Special aspects of TDFA simulations

The simulations are an important step in the amplifier development process. They allow to reduce the costs of the experiments and help to create the devices fulfilling the initial requirements. In our case, the information about the advisable fiber parameters (like thulium doping, core diameter or numerical aperture) gathered from the simulations can be used as a feedback in the fiber manufacturing process. On the other hand, different aspects of amplifier performance and the way how do they influence the TDFA operation could be explained basing on simulation results. We will start our simulations with common dual-wavelength pumped TDFA.

6.3.1   Dual-wavelength pumped TDFA

One of the most common TDFA pumping schemes is using the optical radiation at 805 and 1056 nm. Since both pump wavelengths corresponds to resonant absorptions in thulium, one can expect very good performance of such a amplifier. Moreover, using pump power management one can achieve a gain-shift. All these aspects makes this type of TDFA interesting example for the simulation.

In first step, the gain spectra for different pump powers at 805 and 1056 nm were simulated. We assumed 2 m long TDF with core diameter of 3.2 μm, numerical aperture of 0.24, and thulium concentration of 5000 ppm. The co-directional pump direction was chosen. The pump power at 805 nm was kept constant and its value was 200 mW. The power of pump diode at 1056 nm was swept from 0 to 200 mW. The calculated gain spectra are shown in figure 6.4.
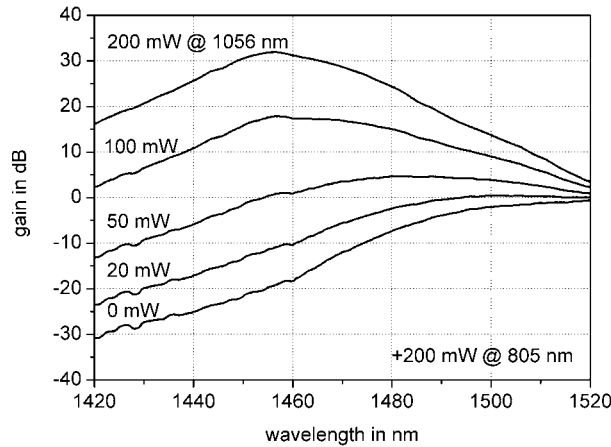
Figure 6.4: Simulated gain spectra for dual-wavelength pumped TDFA

Large pump power at 1056 nm was necessary to reach high amplification, which is not surprising. On the other hand, with increasing pump power at 1056 nm the gain spectrum changes its shape and wavelength of the maximum gain shift towards shorter wavelengths. The maximum gain of more than 33 dB was achieved for the signal wavelength at 1455 nm.

The gain shift beyond 1480 nm was observed at 50 mW of the pump power at 1056 nm and 200 mW at 805 nm. Since the gain shift can be observed only in partially inverted TDF, as it is also discussed in the next section, the population distribution and pump absorption along the active fiber, shown in figure 6.5, help to understand this process.

As shown in figure, both pumps are strongly absorbed at the beginning of the TDF. But
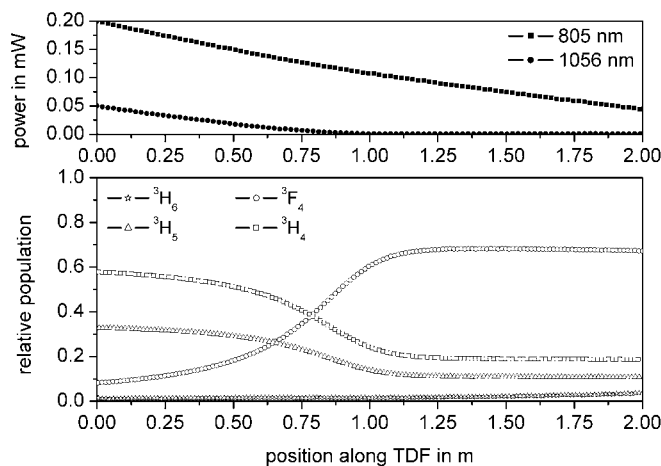
Figure 6.5: Pump power and relative population distribution in TDFA pumped with 805 and 1056 nm

since the power at 1056 nm is totaly absorbed along the first meter of the active fiber, the population inversion between lower and upper amplification energy levels can not be kept. On the other hand, strong pump radiation at 805 nm effectively populates $^3F_4$ level. This result in shifting of the gain spectrum towards longer wavelengths.

Unfortunately, results of these simulation do not agree with the measurements (compare chapter 7.3.1). It was observed, that for a fiber doped with 5000 ppm thulium already small pump radiation at 805 nm caused drastic decrease of the gain and its further enhancement caused total disappearing of the amplification. The intensive investigations yielded to conclusion, that gain reduction in this type of TDFA is caused by strong ASE radiation at 800 nm. Because of the non-negligible population of the upper amplification level the launching of pump power at 805 nm leads to forming of the fiber amplifier at this wavelength, which effectively depopulates $^3H_4$ level. The simulation performed before did not include the ASE in the wavelength region of 800 nm, which, is very important for the dual-wavelength pumped highly thulium-doped fiber amplifier.

6.3.2   Gain shifting process in single-wavelength pumped amplifier

Since the thulium-doped fiber amplifier operates primarily at wavelengths around 1460 nm, where the OH$^-$ absorption peak increases the attenuation in the transmission fibers, it is important to shift its gain maximum towards longer wavelengths. This can be managed by assuring low average population inversion between $^3H_4$ and $^3F_4$ levels, as it was the case

described in previous section. Unfortunately, the occupation is an internal property of the energy level and the operator can influence it only in a limited way. The gain-shift was observed in amplifiers employing a two-color pumping scheme [165, 166] as well as 1056 nm pumped amplifiers based on highly thulium-doped fibers [50]. The gain shift in the second amplifier type is caused by cross-relaxation. To simulate this process we expand the basic amplifier model and introduce a routine, which calculates the change in the occupation of the levels involved in this process according to a coupling factor X. This factor describes the change of population of the energy levels involved in the cross-relaxation process. The rate equations for the energy levels 0, 1, 4 (see figure 3.2) involved in this process changes and they include the cross-relaxation terms as follows:

$$
\begin{aligned}
&- X n_0 n_4 \text{ , for level } {}^3\mathrm{H}_4 \\
&+ X n_0 n_4 + X n_0 n_4 \text{ , for level } {}^3\mathrm{F}_4 \text{ ,} \\
&- X n_0 n_4 \text{ , for level } {}^3\mathrm{H}_6
\end{aligned}
\tag{6.18}
$$

where n_i is the relative occupation number of the energy level i.

Since the value of coupling factor X is not know, its value was estimated to be comparable with the radiative or non radiative rates. The cross-relaxation process is described in more details in chapter 7.2.1. As result of the energy transfer between neighboring thulium ions the local populations of the ${}^3\mathrm{F}_{2,3}$ and ground level decreases for the benefit of ${}^3\mathrm{F}_4$ level. The pump radiation is fully absorbed along the fiber length and the calculated population distribution along 2 meters of active fiber doped with 5000 ppm thulium is shown in figure 6.6. For the calculation the coupling factor X was set to $2000\,\mathrm{s}^{-1}$.

In the first part of the active fiber a population inversion between levels ${}^3\mathrm{H}_4$ and ${}^3\mathrm{F}_4$ is achieved due to the high pump absorption caused by strong ESA at 1056 nm and the cross relaxation process. Compared to the common TDFAs in which the population inversion is kept high along the fiber assuring high gain, here only part of the TDF is inverted. The population of the upper amplification level decreases after about 1 meter. This results in a gain shift of 18 nm compared to the common, low thulium-doped fiber amplifier, for which the cross-relaxation process is negligible. Comparable gain-shift was also measured for this amplifier as it is reported in chapter 7.2.2. The gain spectra of both amplifier types (TDFA and GS-TDFA) are shown in figure 6.7.

The maximum gain can be increased by applying higher pump power and/or by varying the length of the active fiber. However, the higher pump power results in the population inversion along the total length of the fiber, which shifts the amplification maximum to its original wavelength of 1460 nm. Therefore a careful pump management is one of the key issues in GS-TDFAs.

As shown in figure 6.6 the population of the ground state in thulium is very high. This
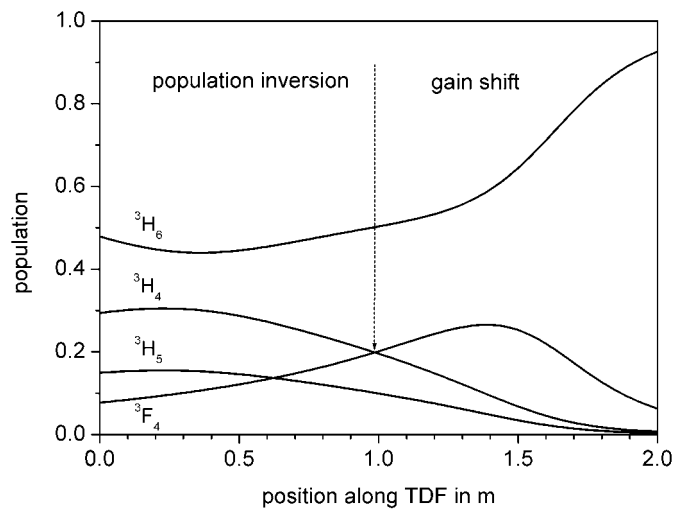
Figure 6.6: Population of the energy levels in gain shifted TDFA
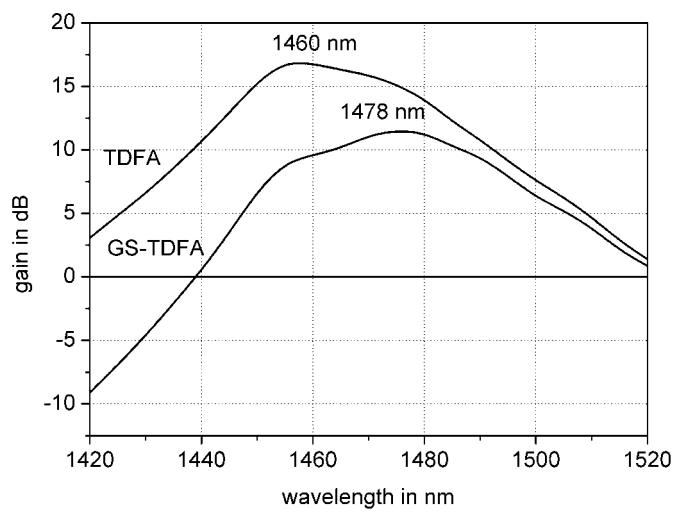
Figure 6.7: Gain spectrum of the standard and gain shifted TDFAs. For standard TDFA we assumed $X = 0\,\mathrm{s}^{-1}$ and 800+1050 nm pumping scheme whereas for GS-TDFA $X = 2000\,\mathrm{s}^{-1}$.

means, that only limited part of dopant ions (30 to 50 %) actively participates in the amplifi-

cation process. Due to the strong emission $^3H_4 \rightarrow ^3H_6$ at 800 nm, the upper amplification level is depopulated not only by the usable emission into the $^3F_4$ level, but also by the transition into the ground state. The total power of the second emission line is 10 times larger than that corresponding to $^3H_4 \rightarrow ^3F_4$ transition, which is shown in figure 6.8.
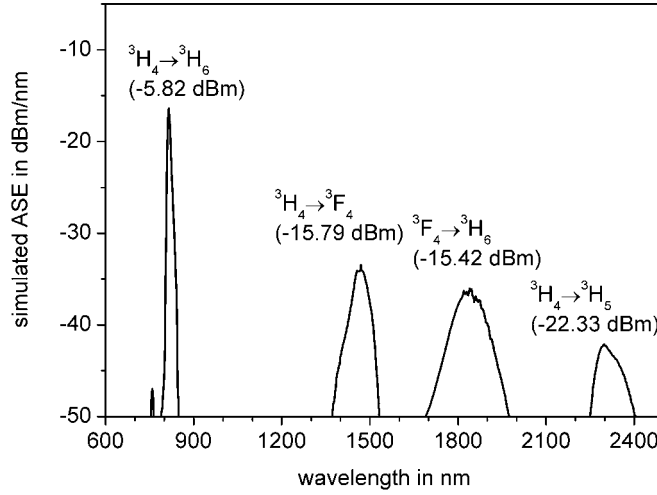
Figure 6.8: Calculated ASE powers for different emission lines in TDF

The simulation shows, that strong ASE centered at 800 nm limits the pump efficiency of the TDFA in this pumping scheme, which was also measured. On the other hand, it is difficult to suppress it using simple core/cladding guiding structure of the active fiber. Modifying the refractive index profile of the fiber or introducing a selective attenuator could lead to impairment of the unfavorable ASE and enhancement of the pumping efficiency. As an alternative, a host glass with smaller emission cross-section for the transition $^3H_4 \rightarrow ^3H_6$ can be used.

The simulation results are in very good agreement with measurements (compare chapter 7.2.2) and are the evidence on importance of the cross-relaxation process, which is responsible for high gain in highly-thulium doped fiber amplifiers. But because of the fact, that cross-relaxation seems to play very important role in this amplifier one should find a way to determine the coupling factor X. Moreover, we assumed only one cross-relaxation $(^3H_4,^3H_6) \rightarrow (^3F_4,^3H_4)$, which is not the only one energy transfer process in highly-doped TDF (see chapter 7.2.1). The advanced simulation should also include the second energy transfer $(^1G_4,^3H_6) \rightarrow (^3F_{2,3},^3F_4)$ which becomes important for high pump powers at 1056 nm.

6.3.3   TDFA with co-operating ring fiber laser

The TDFA suffers from the long lifetime of the $^3F_4$ level, which hinders the pumping process. The excited ions relax into this level and do not participate in the amplification. Therefore a second pump source with a wavelength corresponding to ESA starting from first excited level is employed to reduce the occupation of the $^3F_4$ level and help to create the population inversion between $^3H_4$ and $^3F_4$. The depopulation of the lower amplification level can be realized by a fiber laser operating at the wavelength of the $^3F_4 \rightarrow ^3H_6$ transition [167]. To simulate the fiber laser some modification in the model has to be done. We introduce two WDM couplers on both sides of the active fiber. They couple signal and 805 nm pump radiation together with the amplifier spontaneous emission at about 1850 nm. When the proper coupler arms are connected the ring cavity is formed and the laser oscillations are induced. A small part of the laser radiation (3 %) was coupled out of the laser ring to control its performance. The outgoing part of ASE corresponding to $^3F_4 \rightarrow ^3H_6$ transition is shown in figure 6.9. For the comparison, the corresponding spectrum with opened fiber ring was shown as well.
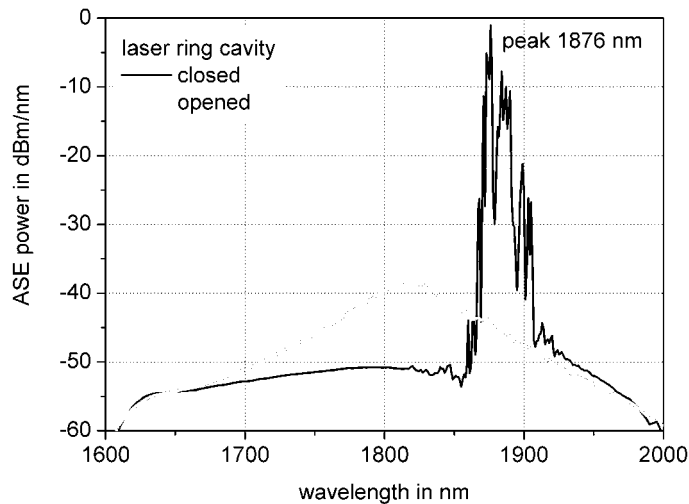
Figure 6.9: Simulated amplified spontaneous emission centered at around 1800 nm

It is important to note that the ASE power in the laser ring is almost 100 times higher than that detected at the amplifier output and shown in the figure. However the changes in the emission spectrum are more important than the absolute ASE power. It is obvious, that closing the ring cavity changes the emission spectrum and its peak shifts towards longer wavelengths and the bandwidth decreases. On one hand this is caused by the spectral char-

acteristic of the WDM coupler, on the other hand the starting laser oscillations narrow the ASE. The spectra around 1850 nm resembles superluminescence rather than pure laser oscillation. Pure one-wavelength laser operation was not observed (compare measurement results collected in chapter 7.4.1), but it is not necessary to improve the amplifier's performance. The ASE radiation with a peak wavelength of 1878 nm and a total power of about 12 dBm in the laser ring enhance the amplifier's gain by 7 dB compared to a TDFA pumped only at 805 nm. The signal wavelength was 1480 nm and its power was −30 dBm. The comparison of gain spectra for amplifier with co-operatively operating fiber laser and without it are shown in figure 6.10.
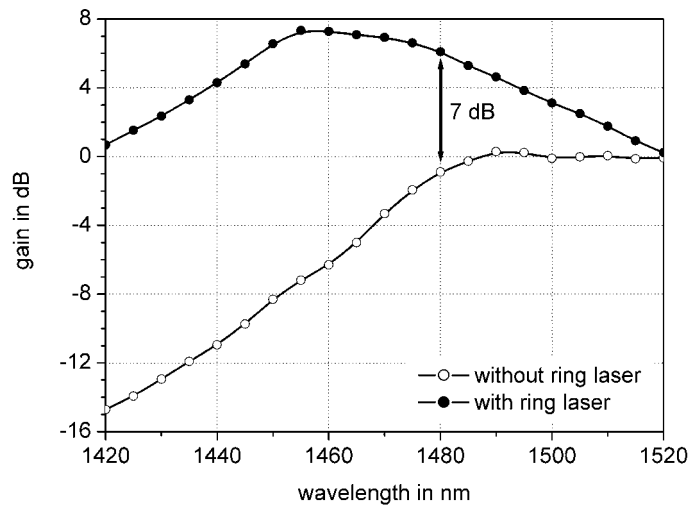
Figure 6.10: Improvement of the amplifier's performance by applying fiber laser at 1876 nm

As expected, amplifier pumped only at 805 nm does not show the signal amplification. For signal wavelengths below 1480 nm the gain is negative and increases slightly for larger wavelengths. Above 1485 nm the amplifier becomes transparent and does not attenuate the incoming signals. The gain spectrum of the TDFA with co-operatively working fiber laser is the same as for the common amplifier, which base on low thulium-doped fiber and does not show gain-shift. The maximum gain of 6.1 dB was expected to be achieved for 1460 nm. This value agree very well with the measurements (compare chapter 7.4.2) in which the maximum gain of about 11 dB was observed for 1485 nm indicating a 15 nm gain-shift not recorded in simulations.

The simulation of the gain shift process as well as the amplifier with fiber ring laser shows

that the model operates correctly. Since the number of parameters is large and their real values in many cases are unknown, one should not expect a quantitative agreement with the measurements. However, it was shown that the qualitative agreement between simulation and measurement is very well. Of course, the discrepancies between measurement and simulation can be used to gather the correction factors, which makes the simulations more close to reality. But it was not the aim of this work. It was much more important to understand the physical background of the amplifier and the relationships between different parameters and processes occurring in TDFA. It was found, that this requirements are fully met by our TDFA model.

7 Measurements on thulium-doped fiber amplifiers

In the previous chapters we focused on issues important for the development of the thulium-doped fiber amplifier. At that point we are ready to collect all previously gathered experiences and design an amplifier. This chapter starts with the description of the measurement results of the active fibers used for the amplifier investigations. Next, several experiments with single- and double-wavelength pumped TDFA will be reported. Special attention was paid to the cross-relaxation process responsible for the amplification in highly thulium-doped amplifiers, which is described in section 7.2.1. In section 7.4.1 the results of experiments on a fiber ring laser operating at about 1900 nm are presented. This laser was applied further in the amplifier setup, which leads to improvement in the TDFA performance as previously simulated.

7.1 Properties of active fibers

The thulium-doped fibers used for the experiments consist of two types of fluoride glasses. Typical core composition is

$$53ZrF_4 - 16BaF_2 - xLaF_3 - 3AlF_3 - 20NaF - 4PbF_2 - 0.125InF_3 - yTmF_3.$$
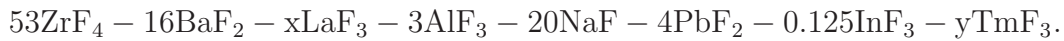
The numerical aperture of the fiber is determined by the cladding composition. In the case of fiber A (see table 7.1) the cladding composition was

$$53ZrF_4 - 20BaF_2 - 3.875LaF_3 - 3AlF_3 - 20NaF - 0.125InF_3,$$
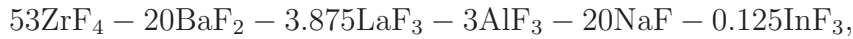
which leads to the numerical aperture of 0.16. For fibers B and C a HZBLAN cladding glass with the composition

$$43HfF_4 - 10ZrF_4 - 18.875BaF_2 - 3.5LaF_3 - 2.5AlF_3 - 22NaF - 0.125InF_3$$

was used. The concentration of thulium and lanthanum in the core glass are complementary and their total amount is 3.875 mol%. For fiber manufacturing, both glasses were melted in platinum crucibles under dry nitrogen atmosphere ($H_2O < 1$ ppm) at around 800 °C. The purity of the raw materials was 99.99 %. Casting the melt of cladding glass into a rotating mold leads to a tube of cladding glass. The melt of the core glass was filled into the cladding tube and this structure was elongated to sticks with a length of about 15 cm and a diameter of 2 - 3 millimeters. The sticks were afterwards placed in a second cladding tube and the fiber was drawn out of this preform using a furnace with the temperature of about 300 °C. In the last step fibers were coated with UV-curable acrylate to protect them from humidity and improve their mechanical stability.

Table 7.1: Parameters of thulium-doped fibers used for amplifier experiments

fiber	core diameter in μm	NA	c_{Tm} in mol%	α @ 1400 nm in dB/m
A	4.0	0.16	0.5	0.32
B	2.6	0.25	0.5	0.36
C	2.5	0.26	0.2	0.33

Three low-loss thulium-doped fibers were used for the amplifier experiments. Their basic parameters - core diameter, numerical aperture and attenuation are collected in table 7.1.

The fiber core and numerical aperture were measured indirectly by spectral investigation of the mode field diameter. Each measurement was performed three times and the mean value as well as the measurement accuracy were calculated. The accuracy was estimated as standard error of the mean value. In the next step the results were fitted using equations (5.3) and (5.4) given in chapter 5. The measurement results for fiber B are shown in figure 7.1.
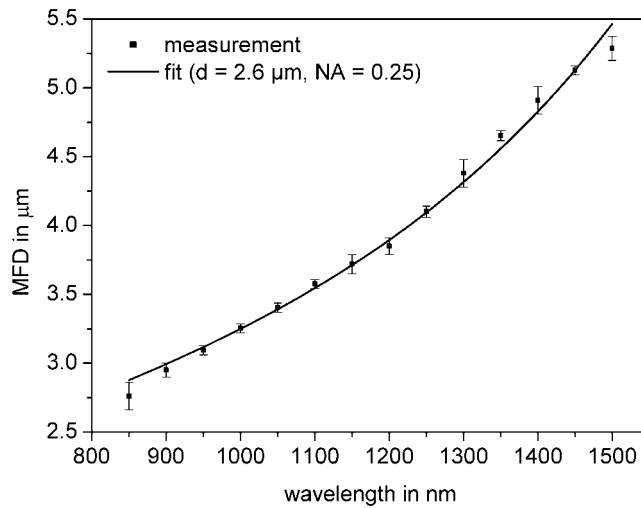
Figure 7.1: Spectrally measured mode field diameter of fiber B

Since the spectral attenuation of the thulium-doped fibers determines the efficiency of the signal amplification and is the criterium of the general fiber quality, its value was investigated in the wavelength region from 800 to 1600 nm. The spectral losses for all fibers are shown in figure 7.2.
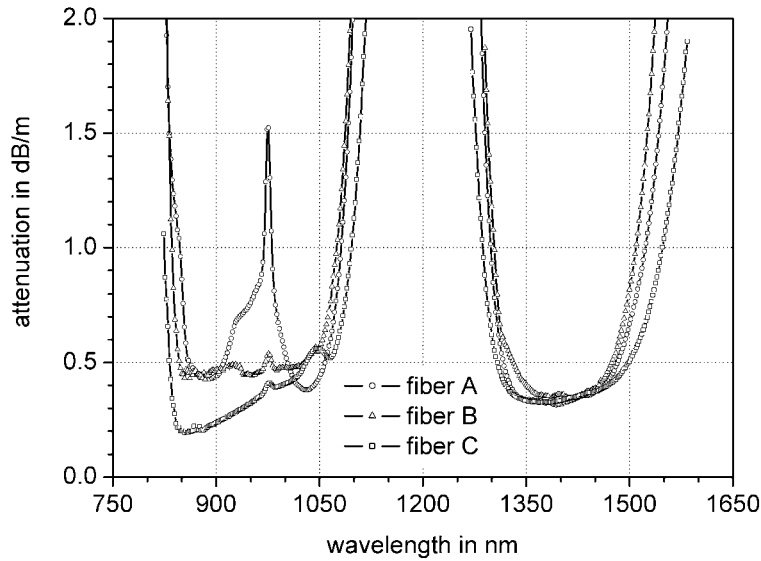
Figure 7.2: Attenuation of thulium-doped fibers used for TDFA experiments

The attenuation spectra for the fibers are similar and show three large attenuation bands around 800, 1200 and 1600 nm, which correspond to strong ground state absorptions. The minimum attenuation of 0.2 dB/m was recorded at 860 nm for fiber C. All fibers show a residual ytterbium absorption centered at 975 nm, which was measured to be very large for fiber A. This rest absorption is caused by impurity of some of the fluorides used in the preform.

7.2   Single-wavelength pumped TDFA

Single-wavelength pumped TDFAs are one of the amplifier types investigated in this work. Since there is no resonant GSA in thulium around 1050 nm, the efficiency of such an amplifier is weak and high pump power is required to reach significant gain. As mentioned in [50], an improvement of the amplifier's performance was observed when highly-doped TDF was used. This was the motivation for systematic investigations on the cross-relaxation process responsible for highly efficient amplification in single-wavelength pumped amplifiers.

7.2.1   Cross-relaxation in highly-doped active fiber

Cross-relaxation processes are often used in the amplifier or laser applications. They are present in many applications where one rare-earth ion acts as an active dopant and another operates as a sensitizer. Such a combination can be found in Er^{3+}/Yb^{3+} doped fiber amplifiers

[168] or Pr^{3+}/Yb^{3+} based up-conversion visible lasers [169, 170]. In highly thulium-doped fibers the distance between dopant ions is small enough to allow the exchange of the energy between neighboring ions [171–173]. The cross-relaxation in TDFA can be easily explained using the energy level diagram of thulium as it is shown in figure 7.3.
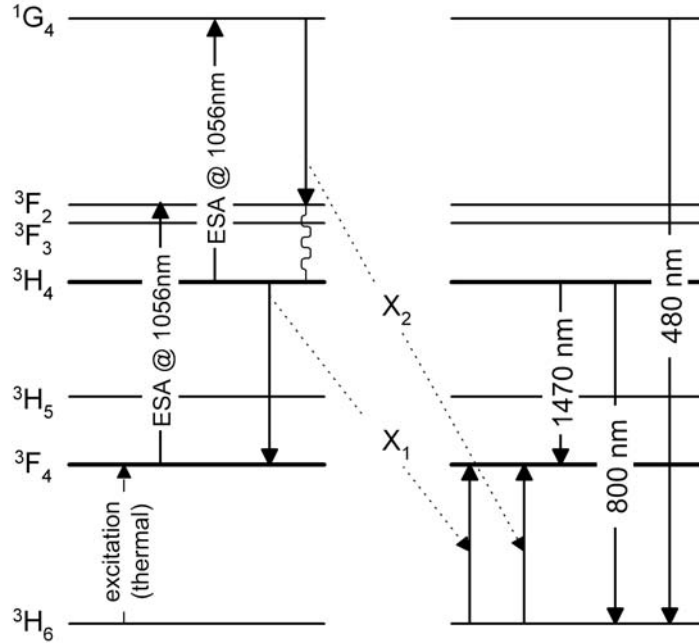
Figure 7.3: Cross-relaxation mechanism in highly thulium-doped fibers

We assume non-zero population of the first excited level, which is enough to start the energy transfer process. This is satisfied when the energy, which is enough to bridge the gap between $^3H_6$ and $^3F_4$ level, is absorbed. In our case the thermal excitation seems to be the most probable excitation mechanism. Due to the high excited-state absorption at 1055 nm, which is the pump wavelength, the ions change their energy state into $^3F_{2,3}$. Since the energy gap between levels $^3F_{2,3}$ and $^3H_4$ is very small, the thulium ions relax non-radiatively into upper amplification level. Due to the small distance between dopant ions in the active fiber the excited ion relaxes into $^3F_4$ level and its energy is used to excite another thulium ion from the ground into $^3F_4$ level. The energy transfer process (X_1) leads to depopulation of the ground level, and its efficiency depends on the thulium concentration.

Since the occupation of the energy states can not be measured directly, we decided to record and analyze the remaining pump power at 1056 nm as well as the luminescence corresponding to emission lines starting from $^3H_4$ level and centered at 800 and 1460 nm. The measurements were performed for 5000 and 2000 ppm thulium-doped fibers by increasing

pump power. The measurement setup used for these investigations is shown in figure 7.4. It consists of the laser diode emitting at 1056 nm (Lumics), a TDF module and an optical
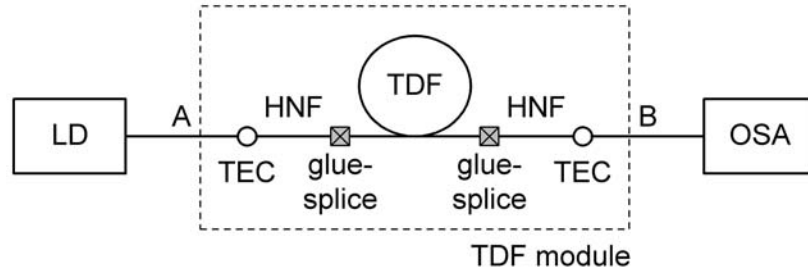
Figure 7.4: Setup used for investigations on cross-relaxation process

spectrum analyzer (AQ6317C, Ando) used to measure the optical power in the specified wavelength range. Because of the difference in the core diameters and numerical apertures of the TDF and silica transmission fiber (SMF-28, Corning), it was necessary to reduce the losses caused by the mode field diameter mismatch. For that reason a piece of high numerical aperture silica fiber (UHNA1, Nufern) called HNF was spliced between SMF-28 and TDF. The connection between SMF-28 and HNF was realized using the thermally-diffused expanded core (TEC) technique. The low-loss glue-splice technique, described in details in chapter 5, was applied to connect the silica and fluoride fiber. Typical attenuation of the glue-splice was 0.5 dB for flat-end fiber connection [174]. The length of the active fiber was 2.52 and 1.04 m for fibers with 2000 and 5000 ppm thulium respectively. The measurements were performed six times for every piece of fiber, three times for configuration A to B and three times in opposite direction. Such a measurement procedure allows to control the condition of the glue-splice, failure or increasing the attenuation of which can influence the results of the investigations. The pump power was swept from 0 to 260 mW and the remaining power together with the radiation at 800 nm and 1470 nm were measured using the OSA. The average pump power and luminescence for all six measurements are shown in figure 7.5.

In common amplifiers one can assume that the pump power is absorbed linearly with increasing pump power. This was also observed for 2000 ppm thulium-doped fiber, for which the pump absorption stayed almost constant at 85 % with increasing input power. This causes a linear increase in the occupation of the $^3H_4$ level and linear enhancement of the luminescence (or better spontaneous emissions (SE)) centered at 800 nm as well as at 1470 nm. In low-doped TDF the $^3H_4 \rightarrow {}^3H_6$ transition at 800 nm was 10 times stronger than the competitive $^3H_4 \rightarrow {}^3F_4$ TDFA transition, therefore only a small gain at 1470 nm can be expected. The pump absorption in 5000 ppm doped TDF in contrast is much stronger. For small input powers (up to about 100 mW), the fiber, which is 2.5 times shorter absorbs 98 % of the
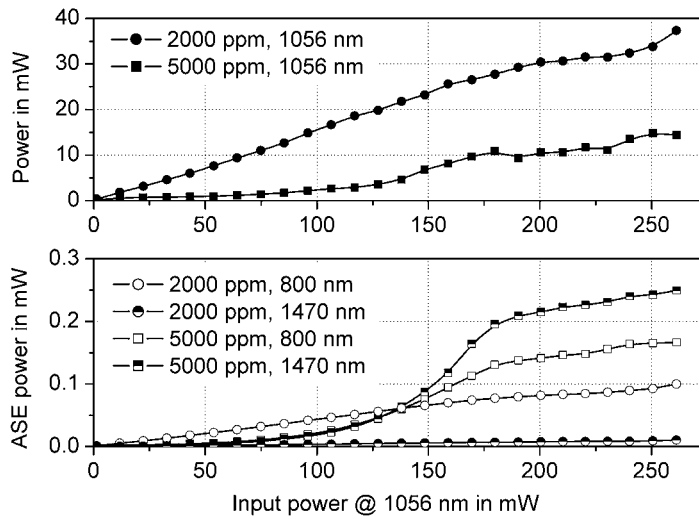
Figure 7.5: Remaining pump power and radiation at 800 and 1470 nm measured for 1.04 and 2.52 m of fiber B and C respectively

launched pump power. Together with the high absorption of the pump power a quadratic increase of the SE was observed. It can be explained by the fact, that cross-relaxation results in quadratic increase in the occupation of the lower amplification level. Strong ESA at 1056 nm causes similar increase in the population of $^3H_4$ state from which the 800 and 1470 nm emission lines start. As soon as the threshold power for the energy transfer is achieved, SE increase, but the $^3H_4 \rightarrow ^3F_4$ transmission was observed to be 1.5 times stronger than that centered at 800 nm. It is caused by the fact, that radiation at 800 nm is still the fluorescence corresponding to $^3H_4 \rightarrow ^3H_6$ transition, whereas much stronger emission centered at 1470 nm is the spontaneous emission which is **amplified** in the active fiber. For pump power higher than about 180 mW the both curves saturates and further increase of the pump power causes only their linear change as it was observed for less doped TDF. Doubling the TDF length results in decreasing the remaining pump power of about 50 % but only for low-doped TDF, as it is shown in figure 7.6. In the case of 2 meters highly thulium-doped fiber the pump power is completely absorbed. Like in the previous case, increasing the launched power causes non-linear pump absorption and population of higher lying levels. Also in this case ASE around 1470 nm is significantly higher than at 800 nm. Further increase of the pump power causes its saturation, however for the powers above 240 mW a second increase of both luminescence lines was observed. This can be explained by the second cross-relaxation process (X$_2$ in figure 7.3), which involves the $^1G_4$ level. Such a energy transfer was observed in thulium-doped fluoroindate glasses [171] and LaF$_3$ crystal [175]. The average population of the $^1G_4$ level seems to be larger for the longer active fibers and since the cross-relaxation is a two-photon
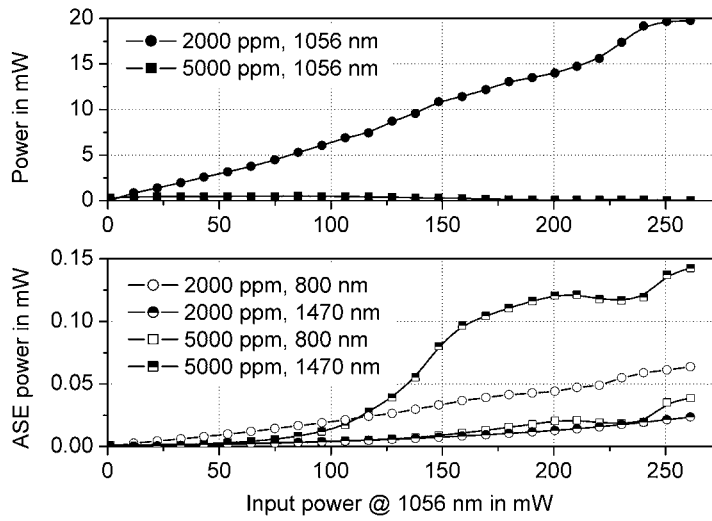
Figure 7.6: Remaining pump power and radiation at 800 and 1470 nm measured for 2.0 and 5.2 m of fiber B and C respectively

process, it changes quadratic for low pump powers, as it was shown in figure 7.7. On the other hand, it is obvious that the cross-relaxation process is more complex as previously described. Its main role is to excite the thulium ions and form the population inversion between $^3H_4$ and $^3F_4$ levels. Unfortunately, for pump powers above 160 mW the energy process causes also significant depopulation of the upper amplifier level, which leads to saturation of the radiation or even its decrease. However, further increase of the pump power at 1056 nm above 240 mW causes total depopulation of the $^3H_6$ level and increase of power of all luminescence lines.

The spontaneous emission centered at about 480 nm starting from $^1G_4$ level was recorded using a setup shown in figure 7.4. Instead of the OSA, a mini spectrometer optimized for the visible radiation was used (Ocean Optics, HR4000). Since the spectrometer measures the relative incoming radiation, the power gathered from the measured spectra were normalized. After initial almost linear increase of the radiation (region 1) significant drop of the power was observed (region 2). This corresponds to strong depopulation of the $^1G_4$ level. Small decrease or saturation of the SE powers in other measured bands was also observed, however the drop in the 480 nm SE radiation was larger. The ions leaving the $^1G_4$ populate the $^3F_{2,3}$ level from which they relax into $^3H_4$ level. Due to the previously explained energy transfer process $(^3H_4,^3H_6) \rightarrow (^3F_4,^3F_4)$ the occupation of the lower amplification level increases rapidly as well as the SE power at 800 and 1470 nm fluorescence lines. The strong ESA into $^3F_{2,3}$ and $^1G_4$ levels increases also the ASE power at 480 nm (region 3).

Since it was shown that the cross-relaxation is very efficient in highly-doped active fibers
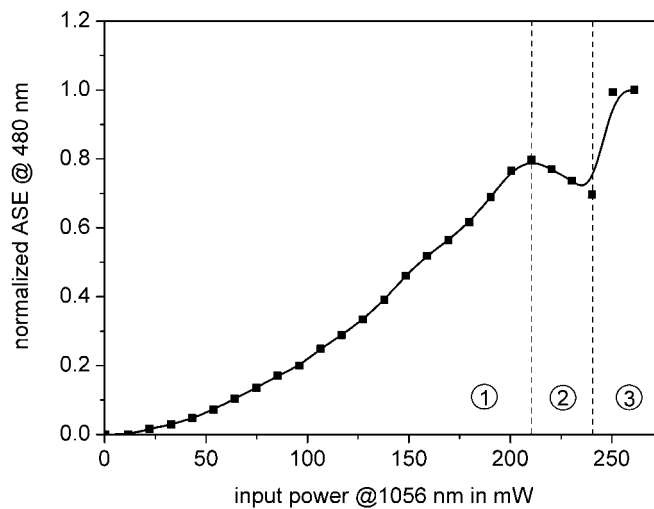
Figure 7.7: Luminescence corresponding to the emission line starting from $^1G_4$ level and centered at about 480 nm

pumped with 1056 nm, this pumping scheme was used in the TDFA, which leads to high gain and low noise figure, as described in next section.

7.2.2   Measurements on the fiber amplifier

The setup of single-wavelength pumped TDFA is shown in figure 7.8. It consists of a tunable
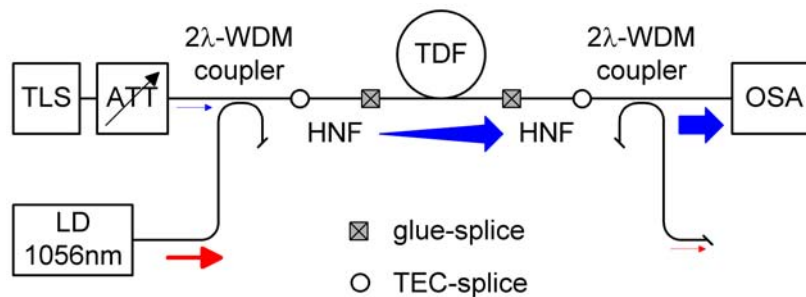
Figure 7.8: Setup of simple, single-wavelength pumped TDFA

laser source (Tunics Reference ES, GN Nettest), two 2λ-WDM couplers, pump diode (Lumics), thulium-doped fiber and optical spectrum analyzer (AQ6317C, Ando). The tuning range of

the TLS from 1390 to 1540 nm covers both S- and S$^+$-band and its power can be varied from -15 up to 10 dBm. For the investigations on small-signal performance of the TDFA a tunable attenuator (8157A, Hewlett Packard) with a dynamic range of 64 dB was used to suppress the signal radiation. The connection between the pump laser diode and the first WDM coupler was realized as TEC-splice (see chapter 5.2) and its attenuation was as low as 0.6 dB. The WDM couplers applied in the amplifier setup had the typical excess loss of 0.3 dB and their coupling ratios were optimized for central signal wavelength at 1470 nm. The open arms of both couplers were cut angularly to avoid unwanted reflections, which are critical for the amplifier performance. Investigations were performed for all fiber types. Since the mode field diameters of the thulium-doped fibers and transmission fiber (SMF-28, Corning) do not match very well as it is shown by the calculated curves in figure 7.9, short pieces of ultra high NA fibers were used on both sides of the B- and C-types of TDF. In the case of
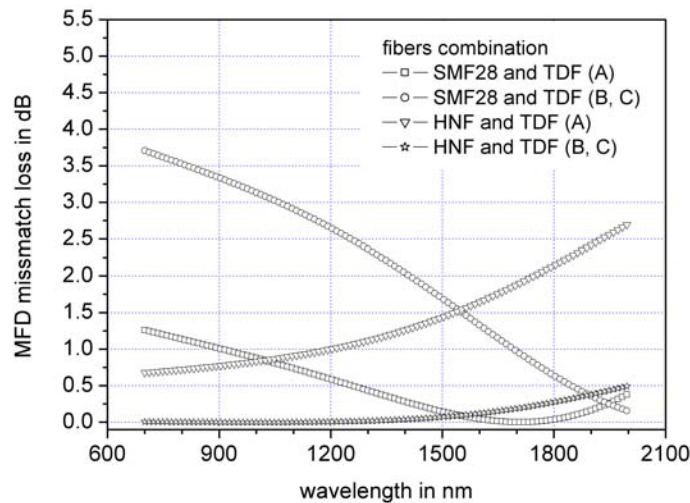
Figure 7.9: Attenuations caused by the MFD mismatch of TDFs and silica fibers used in the amplifier setup

A-type TDF, the low NA and core diameter of 4 μm lead to losses of about 0.8 dB for the pump wavelength and 0.2 dB for 1470 nm. Connecting B- or C-type of the TDF directly with the transmission silica fiber causes large attenuation of 3 dB and 1.8 dB for pump and signal wavelength respectively. Applying silica fiber with the core diameter of 2.9 μm and NA of 0.26 (HNF) decreases the losses below 0.05 dB for both pump and signal wavelength. The connections between SMF-28 and HNF were realized as TEC splices and low-loss glue-splice technique was applied to connect silica and fluoride fibers.

Since the basic setup of TDFA employing any pump configuration consists of pump source(s), WDM coupler(s), and active fiber, a compact case was developed to protect them.

Its photograph is shown in figure 7.10. The case was developed as a vertically expandable

Figure 7.10: Compact TDFA setup

system consisting of two different types of layers. The layer of laser diodes and WDM couplers is shown on the left side whereas the TDF layer is shown at the right side of figure 7.10. The dimensions of the layers are 300 x 210 mm and their thickness is about 20 mm. In order to assure good heat transport from the pump diode into the plate it was necessary to manufacture it out of aluminium. The inter stage fiber connections can by realized using the slit in the center of the each plate. For the mechanically sensitive glue-splices four grooves with the dimension of 70 x 6 x 5 mm were milled on the TDF plate. The layers can be stacked on each other, covered with plexiglass and fixed together with four screws placed at the corners. This compact construction makes it possible to design a robust TDFA, with many amplification stages and/or pump diodes.

Several parameters of the TDFA were measured, but since most of them can be evaluated from gain and noise figure measurements, they became standard amplifier experiments. Both of these values were measured with OSA in an automatic procedure consisting of two steps. As first, the input signal radiation from TLS was recorded and used later as a reference for the spectrum detected at the amplifier's output. Since the output power consists not only of the amplified signal but also broadband amplified spontaneous emission, the gain cannot be estimated by direct comparison of the output and input powers at the signal wavelength. The gain and noise figure were determined by applying amplifier analysis function, which is a feature of the optical spectrum analyzer. It is worth to note that this automatic procedure works properly for the gain estimation, but it was observed that the noise figure value calculated manually by OSA in some cases are not consistent with those wich were calculated from the measurement spectra. Therefore noise figure measurements were typically performed using OSA, but their results were also compared with the calculations performed basing on recorded amplification and reference spectra.

The gain and noise figure measurements show the influence of the parameters of active

fibers on the amplifier's performance. This makes possible to compare amplifiers basing on different types of active fibers, however such a comparison is not absolutely correct because of many unknown parameters of such a measurement as actual pump power in the active fiber or attenuation of the glue-splice. During long term measurements it was observed that the attenuation of the glue-splice increases stochastically (see chapter 5.4), and its actual value can not be estimated very accurately. The results of the investigations in form of spectra with largest gain and lowest noise figure for different fibers are shown in figure 7.11. The measurements were performed for a signal power of $-30\,$dBm and the co-directional pump power was $210\,$mW in the case of fiber B and C. The amplifier based on fiber A was pumped bi-directionally with $200\,$mW pump power from each side. The fiber lengths were 2, 1.8 and $5.2\,$m for fibers A, B and C respectively. As expected, the smallest gain was reached for am-
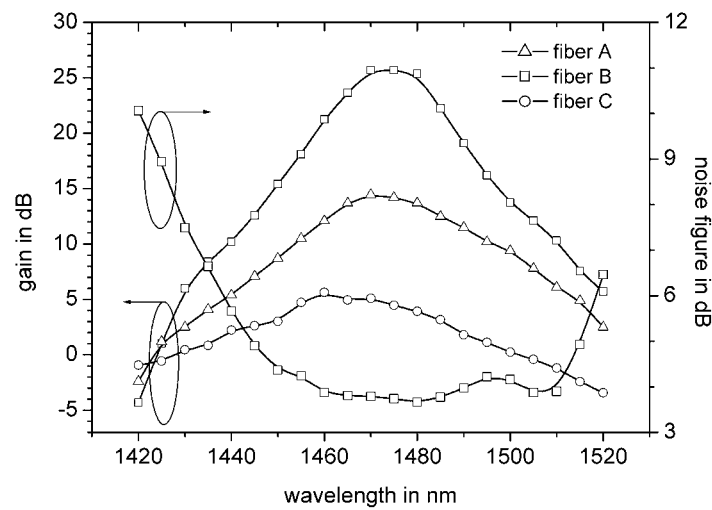
Figure 7.11: Gain and noise figure of single-pumped TDFAs basing on different types of the active fiber

plifier based on fiber C, which is the evidence of low efficiency of the cross-relaxation process in low thulium-doped fibers. The peak gain of $14.5\,$dB measured for bi-directionally pumped TDFA employing fiber A is relatively low, when concerning the pump conditions. The highest gain in this experiment (more than $25\,$dB) was achieved for TDFA based on fiber B and pump power used in this amplifier was about two times smaller than that used in TDFA based on low-NA thulium-doped fiber. This shows the importance of high pump power density, which has to be maintained in the core of the active fiber. On the other hand, the losses caused by mode field diameter mismatch for the active fiber and silica fiber are not negligible, which also influences the achievable gain. The noise figure was measured for all amplifiers, however only for amplifier employing fiber B its value was less than $6\,$dB. It is obvious, that a low

NF can be measured in amplifiers for which the population inversion between $^3H_4$ and $^3F_4$ is high, therefore the lowest noise figure value of 3.7 dB was measured for fiber B and it was reached at 1480 nm of signal wavelength.

A gain shift of about 15 nm compared to typical TDFA gain spectra known from the literature was observed for both 5000 ppm thulium-doped fibers. Such a behavior is consistent with the simulation results (compare chapter 6.3.2) and was also reported in [50] where a gain shift of 30 nm was measured for 8000 ppm TDF. However, the lifetimes of the amplification levels in highly-doped active fibers becomes lower, as it was reported in chapter 3.5. This causes limitation of the achievable signal gain. The dopant concentration of 5000 ppm used here seems not to suffer very much from decrease of the lifetime. The measured gain is comparable or even higher than that reported in the literature for this pumping configuration [50, 176].

The best performance of the TDFA was observed if fiber B was used as an active fiber, therefore further investigations with this pumping scheme were performed only with that fiber. One of the typical amplifier characteristics are the gain and noise figure spectra for different pump powers. They are shown in figure 7.12. As expected from the investigations on cross-relaxation in TDFA, low pump power causes only non-significant gain and large noise figure, which was measured to be larger than 9 dB. Increasing pump power leads to effective population of the $^3H_4$ and $^3F_4$ levels and form significant population inversion between them along the whole length of the thulium-doped fiber. The maximum inversion was achieved for 230 mW pump power, and the remaining power at 1056 nm was negligible. The high pump power leads to a gain of 21 dB with the excellent flatness of 1 dB over the 18 nm wavelength range without application of the gain flattening filter. Since the average occupations of the thulium energy levels show only minor variations for high pump powers, the noise figures show similar spectra and reach their minimum of 4 dB for the signal wavelength of about 1475 nm. The irregular shape of the noise figure spectra is caused by already mentioned not ideal automatic noise figure measurements performed using OSA.

For the applications of TDFAs as power amplifier its saturation power as well as pump power conversion efficiency (PCE) or quantum efficiency (QE)are of great importance. They were measured for 1.9 m long fiber (B-type) co-directionally pumped with the power of 210 mW. As a probe, the signal with the wavelength of 1470 nm was used and its power was swept from -30 to 2.5 dBm. The results of the investigations are shown in figure 7.13.

It is obvious, that the maximum gain of 25.4 dB and quantum efficiency of almost 10 % are limited by the available pump power. The QE for the TDFA based on similar active fiber and employing single wavelength pumping scheme was reported to be 17.5 % [47], however it is not clear whether this value is calculated for the amplifier or the active fiber only.

The PCE or QE curves shown in this work are always given for the active fiber, which is more suitable for comparing different pumping schemes without taking care of the losses
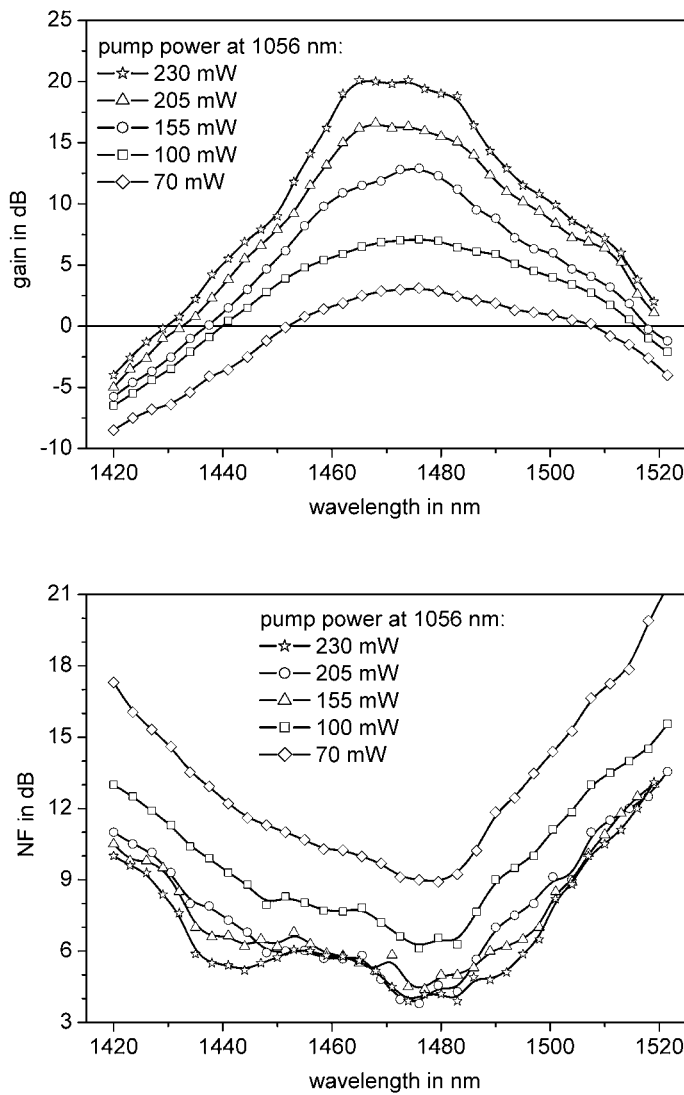
Figure 7.12: Gain and automatically measured noise figure spectra for different pump powers. Measurement conditions: signal: -20 dBm, TDF: 2.4 m, B-type, co-directional pumping

present in the setup. The signal gain decreases drastically with the increase of signal power and drops to 9.74 dB for -2.5 dBm of input power. The saturation power, defined as a power causing 3 dB reduction of the gain, was about -12 dBm, which is much lower than expected. Such a low saturation power can be caused only by too less pump power applied to the TDF. To author's knowledge, there is no study on saturation features of TDFAs, but since TDFA and EDFA behaves quite similarly, the conclusions gathered for EDFA measurements under
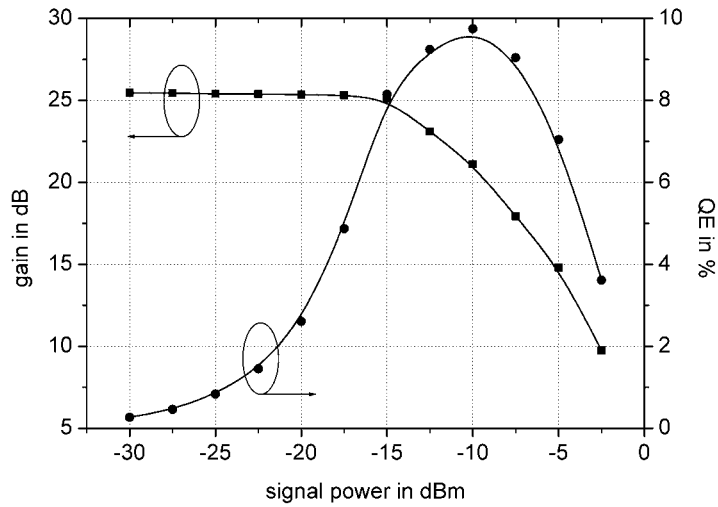
Figure 7.13: Gain saturation and quantum efficiency in single-wavelength co-directionally pumped TDFA. Signal wavelength: 1470 nm

different pump conditions [1] can be applied to our case. It was observed that the saturation power shifts towards larger values, when the gain increases. The gain enhancement can be realized by choosing longer TDFs and applying larger pump power.

7.3 Dual-wavelength pumped TDFA

Several dual-wavelength pump configurations were reported in the literature, but not each of them can be realized using laser diodes. Unfortunately, the pump power needed to achieve high gain and low noise figure operation is higher than about 250 mW, which was the maximum power of the laser diodes used in our investigations. However, a gain of several dB was measured using pumping schemes 805+1056 nm or 805+1412 nm, as described below.

7.3.1 Pumping scheme 805+1056 nm

The investigations on this pumping scheme were performed for B-type as well as for C-type TDF. The simple amplifier setup was extended by another 3λ-WDM coupler as it was shown in figure 7.14.

Laser diodes emitting at 1056 nm and 805 nm were used as pump 1 and pump 2 respectively. The 3λ-WDM coupler was optimized to couple 1056 nm pump and signal wavelength together with the radiation of pump at 805 nm. The experiments reported here were performed using 3λ-WDM coupler with number 9 from table 4.3. The complete amplifier setup
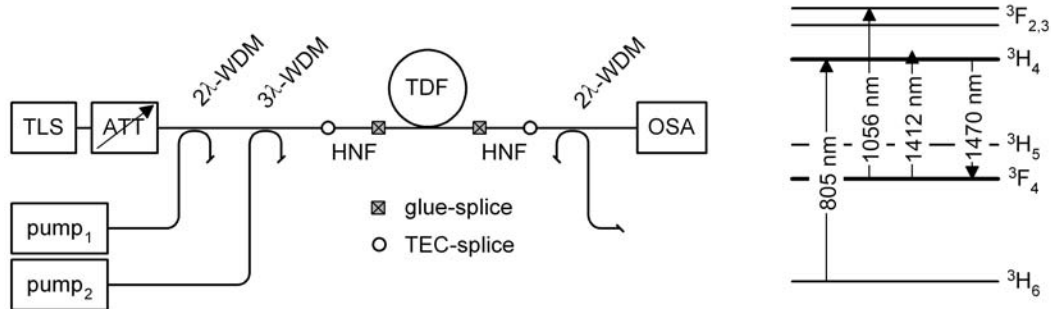
Figure 7.14: Setup and energy level diagram of the double-wavelength pumped TDFA

consists of similar coupler on the output side of the amplifier, but since the pump power at 805 nm is almost fully absorbed along the TDF it is not necessary to use it. Therefore we decided to use simple 2λ-WDM coupler on the output side of the amplifier to reject the remaining power at 1056 nm.

An interesting behavior was observed when fibers with different thulium concentrations were used. Due to the fact that there is no resonant ground-state absorption at 1056 nm one will expect that by introducing pump radiation at 805 nm the pump efficiency and gain increase. Such a behavior was observed only in low doped TDF. For $^{5000}\mathrm{p}_\mathrm{T}^\mathrm{pm}$DF, increasing the pump power at 805 nm leads to a decrease of the gain. The experiments were performed for -20 dBm signal power. The pump power at 1056 nm was kept constant during the whole experiment whereas the power of the other pump increased. The gain spectra of both amplifiers are shown in figure 7.15. The first value in the description of the pump power corresponds to the power at 1056 nm and the second to power at 805 nm. For highly thulium-doped fiber a gain of 20.6 dB at 1465 nm was measured when it was pumped with 1056 nm only. Additional radiation at 805 nm reduces the gain and already 3 mW of its power is sufficient to reduce the gain by 4 dB. It is caused by very strong fluorescence centered at 790 nm and corresponding to $^3\mathrm{H}_4{\rightarrow}^3\mathrm{H}_6$ transition, which depopulate upper amplification level. The pump radiation at 805 nm acts as an indicator for the stimulated emission which leads to originating an efficient amplifier operating at this wavelength.

It was also observed that the radiation at 805 nm causes flattening of the gain spectra, as it was measured for amplifier pumped with 170 mW at 1056 nm and 8 mW at 805 nm for which the gain between 1460 and 1500 nm changes with less than 2 dB.

A totaly different behavior, consistent with expectation, was observed when 2000 ppm TDF was used. The initial gain of 7.53 dB for the amplifier pumped with 1056 nm only was 10 times lower than that pumped with 152 mW at 1056 nm and 19 mW at 805 nm. In this case the cross-relaxation process is inefficient. In the 2000 ppm doped TDF pumped with 1056 nm only limited number of thulium ions populate the upper amplification level. This
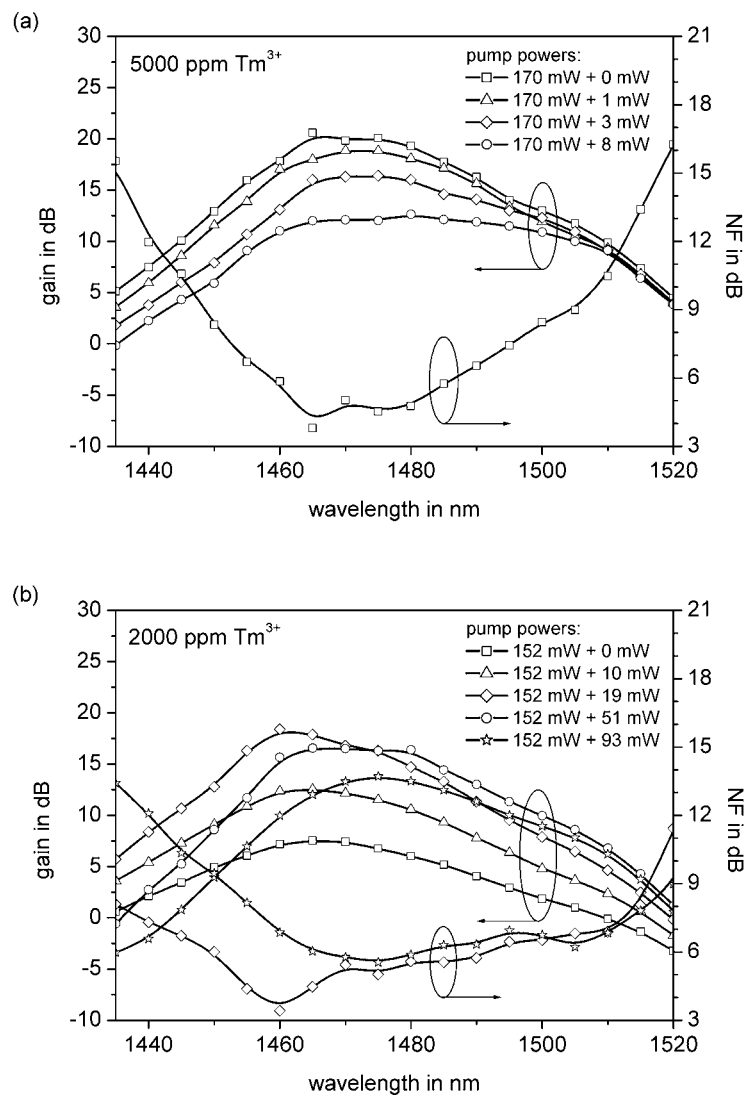
Figure 7.15: Gain and noise figure spectra of TDFAs based on: (a) 3.1 m 5000 ppm B-type and (b) 9.7 m 2000 ppm C-type TDF pumped with 805 and 1056 nm. Signal −20 dBm

can be significantly enhanced by using the GSA at 805 nm. However, too strong power at 805 nm (above 19 mW) leads to drop of the maximum gain and shift its spectrum towards longer wavelengths. This is caused by too low pump power at 1056 nm, which is fully absorbed in the first part of the TDF. The high power at 805 nm excite the thulium ions into the lower amplification level, but the population inversion can not be achieved, which causes the gain shift.

The minimum noise figures were measured for both amplifiers to be less than 4 dB for the pump powers assuring the highest gain. As observed for gain spectra, the corresponding noise figure of C-type based TDFA increases for larger powers at 805 nm and it reaches a minimum value of 5.5 dB for 1475 nm.

The saturation and PCE characteristics for C-type fiber-based TDFA are shown in figure 7.16. Also in this case the maximum gain was limited by the available pump powers,
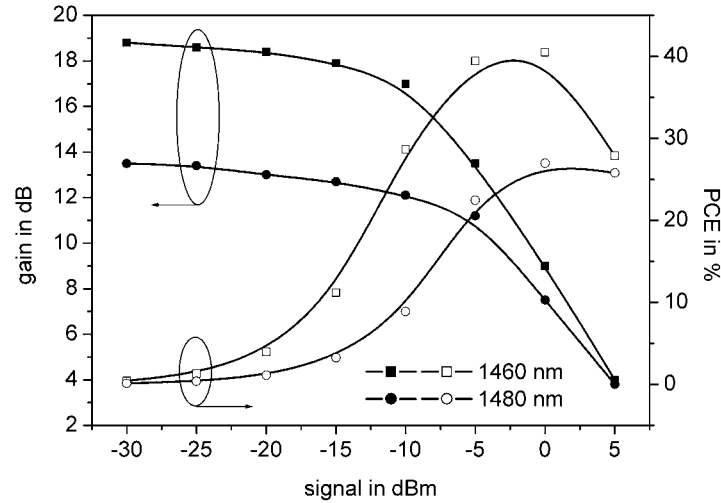
Figure 7.16: Saturation and PCE characteristic of TDFA co-directionally pumped with 805 and 1056 nm. Measurement conditions: TDF: 9.7 m, C-type, pump powers: 152 mW at 1056 nm and 19 mW at 805 nm.

especially at 1056 nm. Although, the laser diodes support up to 220 mW of the pump power, nevertheless the maximum power after both WDM couplers is slightly lower than 185 mW. Its maximum value can not be applied, because reflections at the glue-splices lead to laser oscilations at higher pump power levels. Cutting fluoride and silica fibers with an angle of 5° suppresses the reflections and makes it possible to use powers up to 170 mW. However, the manufacturing such glue-splices is much more time consuming and their application is critical only for amplifiers supporting very high gain.

Due to insufficient pump power the performance of the TDFA is not optimal. The gain decreases immediately for higher signal powers and its 3 dB reduction was estimated to be at around −7.5 dBm of the signal power. Nevertheless, a maximum PCE of 40 % recalculated for the active fiber was measured for this pumping scheme. This is almost 10 % larger than that reported in [177], which was measured for amplifier employing pump powers optimized

for the maximum gain at 1480 nm. The maximum PCE for that wavelength was measured to be 26 %, which is in good agreement with the literature.

7.3.2   Pumping scheme 805+1412 nm

Since the highest PCE was reported in literature for this pumping scheme, some investigations were performed also for this type of TDFA. The amplifier setup corresponds to that used before but a 1412 nm LD was used as diode 2. Unfortunately, the pump power at this wavelength was limited to 100 mW, which was too low to observe high gain. Moreover, the central wavelength of the pump diode was about 10 nm shorter than the peak wavelength of the $^3F_4 \rightarrow {}^3H_4$ transition used for creating population inversion between the amplifier energy levels. Finally, the $3\lambda - \text{WDM}$ coupler used to launch pump power at 1412 nm had to be very long, which resulted in its low mechanical and thermal stability. All these conditions reduced the available pump power to 60 mW. The gain and noise figure spectra of the amplifier based on 9.7 m of C-type TDF are shown in figure 7.17.
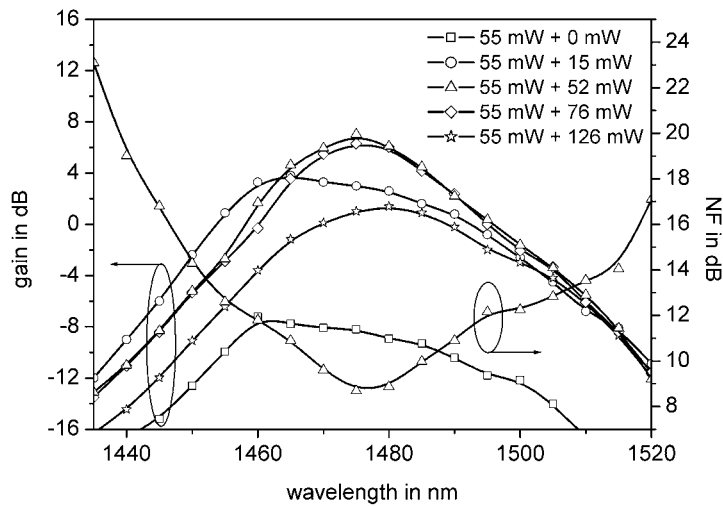
Figure 7.17: Gain and noise figure spectra of TDFA co-directionally pumped with 805 and 1412 nm. Measurement conditions: signal: -20 dBm, TDF: 9.5 m, C-type

The pump power at 1412 nm was kept constant whereas the power of 805 nm radiation was swept from 0 to 126 mW. For very low pump powers at 805 nm it is probable, that a small amplification occurred along a short part of the fiber, but no gain was observed at the amplifier output. Further increase of the 805 nm radiation led to some gain enhancement

and its shift to longer wavelengths. However, when the swept pump power was significantly higher than that emitted by the other diode the measured amplification was less than before. Also in this case the highest calculated PCE of about 15 % was much lower than the values reported in the literature [49, 165]. A PCE of 50 % was reached for TDFA pumped with 11 mW at 780 nm together with 460 mW at 1400 nm. The pump power at around 1400 nm used in this case was 8 times higher than in our case, which explains why our results are worse than expected.

7.4　TDFA with cooperatively working laser

The amplifiers described above operate efficiently by application of pump wavelengths corresponding to the excited-state absorption from $^3F_4$ level, which cause its depopulation needed to form population inversion. Another way to depopulate the $^3F_4$ level, using a cooperative fiber laser at about 1900 nm was proposed by R. Caspary [167].

It is obvious, that the occupation of the $^3F_4$ level is high because of the $^3H_6 \rightarrow {}^3H_4$ GSA, which in fact terminates in $^3F_4$ level. Moreover the lifetime of this energy level is very long, which results in the population inversion between two lowest energy levels. Forcing the laser emission, starting from the $^3F_4$ level closes the energy loop and makes the pumping with single laser source operating at about 800 nm efficient enough to observe the signal amplification. This idea was already investigated by the group of S. Tessarin [178]. The gain improvement of 6 dB was reported when a fiber laser was used simultaneously with the TDFA pumped with the Ti:Saphire laser.

The experiments with this type of amplifier were performed using the setup shown in figure 7.18. Together with TDFA setup the simplified energy level diagram is shown in the figure. The fiber laser was realized as a ring cavity consisting of two 3λ-WDM couplers and
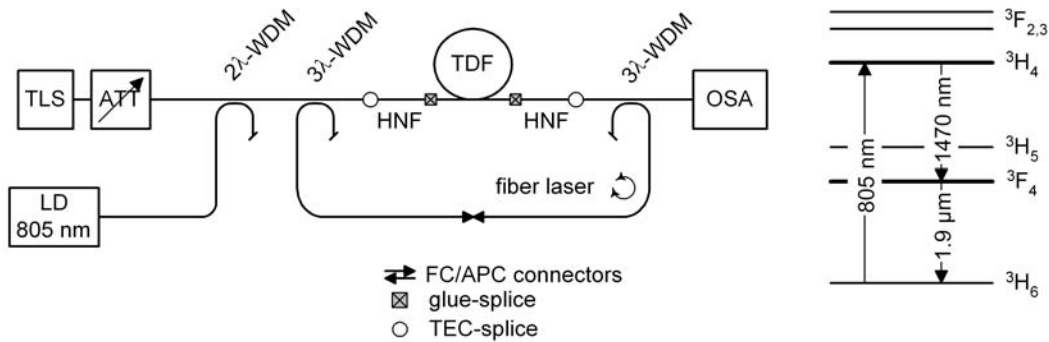
Figure 7.18: Setup of the TDFA using cooperatively working fiber laser

3.6 m of B-type TDF. The parameters of the couplers used in the amplifier setup were already given in tables 4.2 and 4.3 but since they are used for estimating power of the fiber laser, it is appropriate to recall them in table 7.2.

Table 7.2: Coupling ratios of the WDM couplers used in the amplifier setup

coupler	CR @ 790 nm in %	CR @ 1470 nm in %	CR @ 1850 nm in %
$2\lambda-$WDM: 805\1470 (6)	97	7	-
$3\lambda-$WDM: 805+1470\1850 (13b)	5	5	94
$3\lambda-$WDM: 805+1470\1850 (16)	96	3	98

Although this simple configuration assure the single-mode transversal operation, but longitudinally it is a multi-mode laser. Moreover, since there is no isolator inside the laser ring, the amplified spontaneous emission travels clockwise and counter-clockwise in the laser cavity. Finally, the propagation conditions for wavelengths above 1600 nm are not optimal, because of V-number, which is smaller than the guiding limit of 1.6 for fibers B and C. All these aspects result in radiation, which is in fact not a laser operation. It resembles more the superfluorescence [179], which is typically the preceding stage to pure laser operation. However, as it is shown below, the purely single-mode operation is not necessary to depopulate first excited state and improve performance of the amplifier. Although it is not fully correct,we will call this radiation source as fiber laser.

7.4.1   Fiber laser operating at around 1900 nm

The performance of the fiber laser was investigated for opened and closed ring cavity. In this experiment the laser radiation leaving the amplifier setup (about 2 % of its power) was measured using an InSb detector placed behind a monochromator. The results of these experiments are shown in figure 7.19. As expected from the simulation (see chapter 6.3.3), in the case of opened cavity only broad ASE around 1825 nm was observed. As soon as the laser ring is closed, the travelling ASE radiation becomes larger and narrower. Its central wavelength shifts to 1849 nm and the relatively large FWHM of 7 nm was observed for 250 mW of the pump power at 805 nm. The laser performance may be improved by using a double-clad thulium-doped fiber instead of the high NA fiber optimized for conventional pumping schemes as it was demonstrated in high-power fiber lasers [180]. Since the pump and signal radiations are launched into the fiber core, the total internal reflection occurs on the interface to the inner cladding. Coupling the laser radiation into the inner cladding with larger diameter improves the propagation conditions and the higher output power and narrower laser spectrum can be expected.
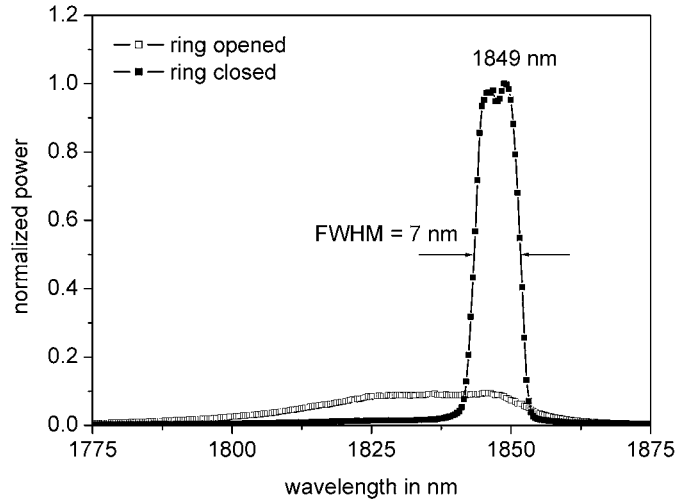
Figure 7.19: Emission spectra of the ring fiber laser

As shown in the next section, the pure laser operation is not necessary to reach an enhancement of the gain and noise figure characteristics, when the laser radiation is launched in the amplifier's setup.

7.4.2　Performance of the amplifier

To check the influence of the fiber laser on the gain and noise figure of the amplifier the measurements were performed with and without the laser. The pump power at 805 nm was kept constant and its value was 250 mW, whereas the signal power was −20 dBm. The results of our investigations are shown in figure 7.20. A large gain-shift was observed when the fiber ring was disconnected. For such a configuration a maximum gain of 2 dB was measured at 1510 nm. The noise figure was measured to be larger than 6.8 dB in the whole signal bandwidth.

The poor performance of the amplifier was distinctly improved after closing the laser ring. An amplifier gain of more than 10 dB and a noise figure of about 6.2 dB were measured for similar pump power. The fiber gain, defined as the amplification of the fiber itself without taking into account any losses present in the setup, was estimated to be about 14 dB, which is still lower than that for typical pumping schemes. The gain peak shifted towards shorter wavelengths and reached its maximum at 1485 nm. The gain enhancement of 22 dB for 1440 nm or 12 dB for 1485 nm is an evidence of positive influence of the laser radiation at 1849 nm. Depleting the $^3F_4$ level leads to increase of the number of ions, which interact with the pump radiation. This improves the energy circulation in the loop $^3H_6 \rightarrow {}^3H_4 \rightarrow {}^3F_4 \rightarrow {}^3H_6$.
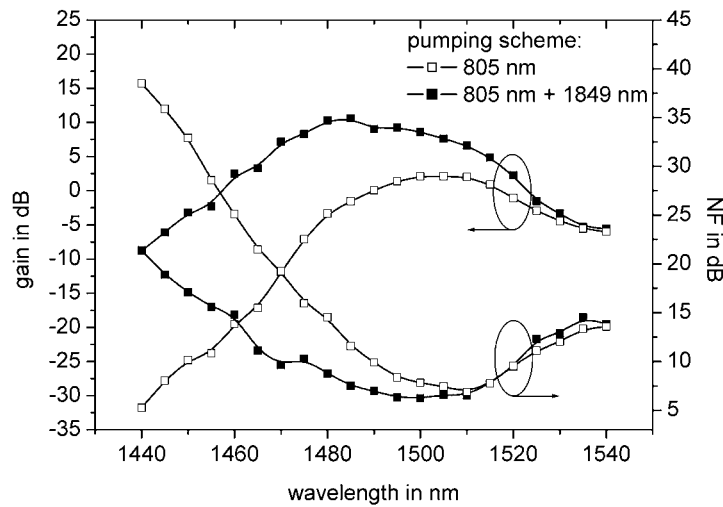
Figure 7.20: Comparison of gain and noise figure spectra for TDFA employing 805 nm pump together with the fiber laser at 1849 nm. Measurement conditions: signal: −20 dBm, TDF: 3.6 m, B-type

The performance of the amplifier depends on the pump power, but although pumping at 805 nm did not lead to high gain, it was interesting to know how the gain of the amplifier changes with increasing radiation of the fiber laser. It is obvious, that every laser starts to operate after exceeding the losses in the cavity. This occurs when the actual power is larger than the laser threshold power. Therefore one will expect significant change of the gain when the laser starts to operate. In order to measure simultaneously the gain of the amplifier and the power of the laser another 3λ-WDM coupler was connected on the output side of the setup. Its coupling ratio was 27 % for signal wavelength and 80 % for 1849 nm. Basing on the coupler ratios the measured output powers at signal wavelength as well as at 1850 nm were recalculated into the gain and laser power travelling in the ring cavity. The measurements were performed for the signal wavelength of 1485 nm, which corresponds to the peak wavelength of the gain spectrum. The signal power was kept constant (−20 dBm) whereas the pump power was swept from 0 to 250 mW with the step of 5 mW. The measurement results are shown in figure 7.21.

For the low pump power the fiber gain is negative and it increases slowly with the pump power. Optical transparency was achieved for 95 mW at 805 nm and almost linear gain enhancement with the coefficient of 0.016 dB/mW was observed up to the laser threshold power, which was found to be about 140 mW. The further increase in the power at 805 nm results in rapid gain increase, which is the result of the fiber laser operation. For the pump powers
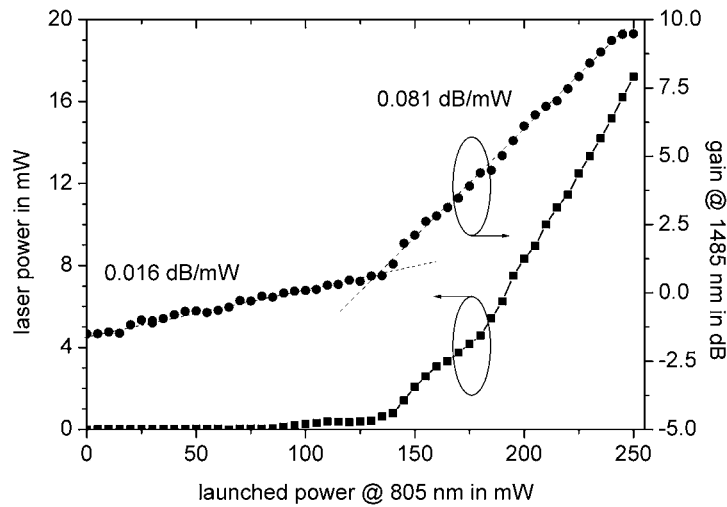
Figure 7.21: Gain and the laser power in the ring as a function of the pump power at 805 nm

above the threshold power of the laser the gain coefficient was estimated to be 0.081 dB/mW. The power of the fiber laser travelling in the ring cavity increases almost linearly with the power at 805 nm and its maximum value was measured to be about 17 mW.

The successful demonstration of the amplification process in this amplifier employing an advanced pumping technique opens new research possibilities for TDFAs. Optimizing the fiber geometry and development of new, high power pump diodes at the optimum operating wavelength at 790 nm can result in construction of less expensive TDFA. Since its price depends mostly on the costs of pump sources, a reduction in the number of pumps is always advantageous. On the other hand, an optimal designed fiber laser requires not only a special active fiber, but also transmission fibers and WDM-couplers.

Conclusions

The aim of this work was to develop and investigate laser diode pumped thulium-doped fiber amplifiers operating with different pumping schemes. An amplifier with gain of up to 25 dB and noise figure smaller than 4 dB was realized using single-wavelength pumping scheme and highly thulium-doped fibers. Moreover, a gain of up to 11 dB of the amplifier employing cooperatively operating laser at 1849 nm was achieved by employing advanced pump scheme. These two examples give a small impression of experiments contained in this work, therefore let us now recall all the most important results of our investigations.

They started with the spectroscopic experiments, in which thulium-doped ZBLAN and IBZP samples were investigated. We found that the oscillator strength of the GSA transition to upper amplification level is larger in IBZP compared to ZBLAN, but due to the different Stark splitting, the peak height on the other hand is much smaller. The significant ESA transition at 1050 nm used for pumping of the amplifier was found to be much smaller in the IBZP glass, whereas the other relevant ESA at 1400 nm is about 10 % larger. Also the emission cross-section of the amplifier transition was measured to be about 17 % larger in the IBZP glass. However, the competitive transition at 2300 nm is stronger by nearly the same factor, which does not show any significant advantage of the IBZP glass as a host for thulium.

The investigations on fiber couplers showed, that the manufacturing of reliable WDM couplers combining very distant wavelengths (e.g. 805 and 1850 nm) or wavelengths, which are very close to each other (e.g. 1412 and 1470 nm) is possible, however one has to take care about their thermal and mechanical stability. Long coupling lengths makes the coupler very sensitive, therefore they should be avoided.

The glue-splice technique is reported to be an reliable way to connect silica and fluoride fibers with attenuation as low as 0.5 dB. Nevertheless, it was found that it is not ready for the commercial application because of the limited lifetime of the glue-splices operating under high power conditions. The maximum high-power operation lifetime of up to 1000 hours may be not sufficient for commercial applications. However, the performance of the glue-splice can be improved when the endfaces of the fibers are ideally clean and the difference in linear expansion coefficients of both fibers is balanced.

The spectroscopic investigations as well as experiments on fiber couplers and the connection technique were required to simulate the TDFA and design its setup. Among different experiments with the fiber amplifier, special attention was paid on the cross-relaxation process, which was found to be very effective in 5000 ppm TDF. The measurements of fluores-

cence lines starting from $^3H_4$ and $^1G_4$ levels show evidence on two energy transfer processes, which depend on the thulium concentration. Except of the simple, single-wavelength pumping scheme, double-wavelength TDFAs were investigated, however it was found that the power of the pump laser diodes was not sufficient to achieve gain significantly higher than 20 dB. A PCE of 40 % was measured for TDFA employing 805 and 1056 nm pumping scheme. Moreover, the gain shift of 15 nm was observed for this type of amplifier based on 2000 ppm TDF. The maximum available power at 1412 nm was found to be too low to observe amplification in TDFA using 805+1412 nm pumping scheme.

The long lifetime of the lower amplification level, which results in its high occupation when pumping at 805 nm makes it necessary to use a two-steps pumping scheme. However, using a fiber laser operating on the $^3F_4 \rightarrow {}^3F_4$ transition it was possible to demonstrate gain in a TDFA pumped with 805 nm only. The power of the fiber laser travelling in the ring cavity was estimated to be about 17 mW, which is smaller than expected. Its small power is caused by poor propagation condition for wavelengths longer than 1600 nm.

The measurement results shown here are are in good agreement with that reported in the literature. On the other hand, this work summarizes the significant issues of TDFA design, which makes it interesting for designer of the optical transmission systems.

References

[1] E. Desurvire. *Rare-earth-doped fiber lasers and amplifiers*, chapter 10: *Erbium-doped fiber amplifiers*. Editor: M. J. F. Digonnet, Marcel Dekker Inc. New York, Basel, Hong Kong, second edition, 2001.

[2] T. Ito, K. Fukuchi, K. Sekiya, O. Ogasahara, R. Ohhira, and T. Ono. 6.4 Tb/s (160 x 40 GB/s) WDM transmission experiment with 0.8 bit/s/Hz spectral efficiency. In *Proceedings of European Conference on Optical Communication, paper: PDP 1.1*, 2000.

[3] G. Veith, B. Wedding, and Bülow, H. *Optische Kommunikationstechnik (engl. Optical communications technology)*, chapter 25: *Übertragungsstrecken mit Zeitmultiplex (engl. Transmission lines with the time multiplexing)*. Editors: E. Voges, K. Petermann, Springer Verlag, Berlin Heidelberg, 2002.

[4] T. Yamamoto, E. Yoshida, K. R. Tamura, K. Yonenaga, and M. Nakazawa. 640-Gbit/s optical TDM transmission over 92 km through a dispersion-managed fiber consisting of single-mode fiber and "reverse dispersion fiber". *IEEE Photonics Technology Letters*, 12(3):353–355, 2000.

[5] K. Don, A. Coombe, M. Kunigonis, M. Lundergan, O. Seung, and Vodhanel R. S. 16-channel coarse wavelength division multiplexing transmission over 70 km of low-water-peak fiber with 40 Gb/s aggregate capacity. In *Proceedings of the Asia-Pacific Optical and Wireless Communications Conference (SPIE Proceedings)*, volume 1, 2002.

[6] T. Sakamoto, S. Nobua, S. Koike, K. Hadama, and K. Naoya. 4 channel x 10 Gbit/s optical module for CWDM links. In *Proceedings of 54th Electronic Components and Technology Conference*, volume 1, 2004.

[7] G.694.1 (06/02) Spectral grids for WDM applications: DWDM frequency grid, 2002.

[8] T. Kasamatsu, Y. Yano, and H. Sekita. Novel 1.50 μm band gain-shifted thulium-doped fiber amplifier by using dual wavelength pumping of 1.05 μm and 1.56 μm. In *Proceedings of the Conference Optical Amplifier and their Applications, paper: PDP1*, 1999.

[9] B. Zhu, L. Leng, L. E. Nelson, Y. Qian, L. Cowsar, S. Stulz, C. Doerr, L. Stulz, S. Chandrasekhar, S. Radic, D. Vengsarkar, Z. Chen, J. Park, K. S. Feder, H. Thiele, J. Bromage, L. Gruner-Nielsen, and S. Knudsen. 3.08 Tbit/s (77 x 42.7 Gbit/s) WDM transmission over 1200 km fibre with 180 km repeater spacing using dual C- and L-band hybrid Raman/erbium-doped inline amplifiers. *Electronics Letters*, 37(13):844–845, 2001.

[10] K. Fukuchi, T. Kasamatsu, M. Morie, R. Ohhira, T. Ito, K. Sekiya, D. Ogasahara, and T. Ono. 10.92 Tb/s (230 x 40 Gb/s) triple-band/ultra-dense WDM optical-repeatered transmission experiment. In *Proceedings of Optical Fiber Communications Conference (OFC), paper: PD24*, 2001.

[11] M. J. Conelly. Semiconductor optical amplifiers and their applications. In *Proceedings of IASTED International Conference on Optical Communications Systems and Networks (OCSN), tutorial*, 2005.

[12] P. P. Iannone and N. J. Frigo. Applications of SOAa in optical acces and metro networks. In *Proceedings of the Conference Optical Amplifiers and Their Applications, paper: OTuC1*, 2001.

[13] P. P. Iannone, K. C. Reichmann, M. Birk, N. J. Frigo, C. Derosier, R. M. Cassagnettes, T. Garret, A. Verlucco, S. Perrier, and J. Philipsen. A 160 km transparent metro WDM ring network featuring cascaded erbium-doped waveguide amplifiers. In *Proceedings of the Optical Fiber Communication Conference, paper: WBB3*, 2001.

[14] I. Van de Voorde, M. O. van Deventer, P. J. M. Peters, P. Crahay, E. Jaunart, A. J. Philips, J. M. Senior, X. Z. Qiu, J. Vandewege, J. J. M Binsma, and P. J. Vetter. Network topologies for SuperPON. In *Proceedings of the Optical Fiber Communication Conference, pp: 57-58*, 1997.

[15] D. M. Spirit. *Optical fibre lasers and amplifiers*, chapter 6: *Silica fibre amplifiers and systems.* Editor: P. W. France, Blackie Glasgow and London, 1991.

[16] N. Edagawa. *Rare earth doped fiber lasers and amplifiers*, chapter 12: *Fiber amplifiers in telecommunication systems.* Editor: M. J. F. Digonnet, Marcel Dekker Inc. New York, Basel, Hong Kong, 1993.

[17] S. V. Chernikov, S. A. E. Lewis, and J. R. Taylor. Broadband Raman amplifiers in the spectral range of 1480 - 1620 nm. In *Proceedings of Optical Fiber Communications Conference*, pages 117–119, 1999.

[18] Y. Akasaka, L. Kazovsky, R. Huang, D. Harris, and S. Yam. New pumping scheme on distributed Raman amplifier over novel transmission fiber aimed at 40 Gb/s based terrestrial network. In *Proceedings of the European Conference on Optical Communication, paper: 05.2.1*, 2002.

[19] L. Labrunie, F. Boubal, E. Brandon, L. Buet, N. Darbois, D. Dufournet, V. Harvard, P. Le Roux, M. Mesic, L. Piriou, A. Tran, and J.-P. Blondel. 1.6 Terabit/s (160 x 10.66 Gbit/s) unrepeated transmission over 321 km using second order pumping distributed Raman amplification. In *Proceedings of the Conference Optical Amplifier and their Applications, paper: PD3*, 2001.

[20] T. Naito. A broadband distributed Raman amplifier for bandwidths beyond 100 nm. In *Proceedings of Optical Fiber Communications Conference, paper: TuR1*, 2002.

[21] L. Helczynski and A. Berntson. Comparison of EDFA and bidirectionally pumped Raman amplifier in a 40-Gb/s RZ transmission system. *IEEE Photonics Technology Letters*, 13(7):669–671, 2001.

[22] Y. Qian, C. G. Jørgensen, B. Palsdottir, L. Gruner-Nielsen, S. Dyrbøl, J. S. Andersen, and P. B. Gaarde. Bi-directionally pumped discrete Raman amplifier with optimised dispersion compensation for non-shifted transmission fibre. In *Proceedings of the European Conference on Optical Communication, paper: 04.1.6*, 2002.

[23] P. M. Krummrich, R. E. Neuhauser, C. Fürst, and C. Glingener. Raman plus EDFA vs. Raman only amplification in terrestrial long haul WDM transmission. In *Proceedings of the Conference Optical Amplifier and their Applications, paper: OMD5*, 2001.

[24] H. S. Chung, W. Lee, M. J. Chu, Y. B. Lee, H. H. Lee, and D. Lee. A low-noise L-band EDFA with a 1500 nm Raman-pumped dispersion-compensating fiber section. *IEEE Photonics Technology Letters*, 15(4):522–524, 2003.

[25] R. J. Mears, L. Reekie, I. M. Jauncey, and D. N. Payne. High-gain rare-earth-doped fiber amplifier at 1.54 µm. In *Technical digest of Optical Fiber Communication Conference, paper: WI2*, 1987.

[26] M. Suyama, K. Nakamura, S. Kashiwa, and Kuwahara H. 14.4 dB gain of erbium-doped fiber amplifier pumped by 1.490 µm laser diode. In *Technical digest of Optical Fiber Communication Conference, paper: PD6*, 1989.

[27] R. S. Vodhanel, R. I. Laming, V. Shah, L. Curtis, D. P. Bour, W. L. Barnes, J. D. Minelly, and F. J. Tarbox, E. J. Favire. Highly efficient 978 nm diode pumped erbium-doped fibre amplifier with 24 dB gain. *Electronics Letters*, 25(20):1386–1388, 1989.

[28] J. R. Armitage, C. G. Atkins, R. Wyatt, B. J. Ainslie, and S. P. Craig. Spectroscopic studies of Er^{3+}-doped single mode fibres. In *Proceedings of Laser and Electro-optics Conference*, 1988.

[29] E. Desurvire, C. R. Giles, and J. R. Simpson. Saturation-induced crosstalk in high-speed erbium-doped fiber amplifiers at $\lambda=1.53$ µm. In *Proceedings of Optical Fiber Communication Conference, paper: TuG7*, 1989.

[30] K. Hagimoto, K. Iwatsuki, A. Takada, M. Nakazawa, M. Saruwatari, K. Aida, K. Nakagawa, and M. Horiguchi. A 212 km non-repeated transmission experiment at 1.8 Gb/s using LD pumped Er^{3+}-doped fibre amplifiers in an IM/direct-detection repeater system. In *Proceedings of Optical Fiber Communication Conference, paper: PD-15*, 1989.

[31] S. Saito, T. Imai, T. Sugie, N. Ohkawa, Y. Ichihashi, and T. Ito. Coherent transmission experiment over 2223 km at 2.5 Gbit/s using erbium-doped fibre amplifiers. *Electronics Letters*, 26(10):669–671, 1990.

[32] A. Righetti, F. Fontana, G. Delrosso, G. Grasso, M. Z. Iqbal, J. L. Gimlett, R. D. Standley, J. Young, N. K. Cheung, and E. J. Tarbox. 11 Gbit/s, 260 km transmission experiment using a directly-modulated 1536 nm DFB laser with two Er-doped fibre amplifiers and clock recovery. *Electronics Letters*, 26(5):330–332, 1990.

[33] A. R. Chraplyvy, J. M. Delavaux, R. M. Derosier, G. A. Ferguson, D. A. Fishman, C. R. Giles, J. A. Nagel, B. M. Nyman, J. W. Sulhoff, R. E. Tench, R. W. Tkach, and J. L. Zyskind. 1420 km transmission of sixteen 2.5 Gb/s channels using silica-fiber-based EDFA repeaters. *IEEE Photonics Technology Letters*, 6(11):1371–1373, 1994.

[34] P. F Wysocki, R. E. Tench, M. Andrejco, D. J. Digiovanni, and I. Jayawardene. Options for gain-flattened erbium-doped fiber amplifiers. In *Proceedings of Optical Fiber Communication Conference, paper: WF2*, 1997.

[35] Y. Ohishi, A. Mori, M. Yamada, H. Ono, Y. Nishida, and K. Oikawa. Gain characteristics of tellurite-based erbium-doped fiber amplifiers for $1.5\,\mu$m broadband amplification. *Optics Letters*, 23(4):274–276, 1998.

[36] Y. Bin Lu and P. L. Chu. Gain flattening by using dual-core fiber in erbium-doped fiber amplifier. *IEEE Photonics Technology Letters*, 12(12):1616–1617, 2000.

[37] J. F. Massicott, J. R. Armitage, R. Wyatt, B. J. Ainslie, and S. P. Craig-Ryan. High gain, broadband $1.6\,\mu$m Er^{3+} silica doped fiber amplifier. *Electronics Letters*, 26(20):1645–1646, 1990.

[38] N. Shimojoh, T. Naito, T. Tanaka, Nakamoto; H., T. Ueki, and M. Suyama. 640 Gbit/s (64 x 10 Gbit/s) WDM transmission over 10.127 km using L-band EDFAs. *Electronics Letters*, 36(2):155–156, 2000.

[39] T. Matsuda, T. Kotanigawa, T Kataoka, and A. Naka. 54 x 42.7 Gbit/s L- and U-band WDM signal transmission experiments with in-line hybrid optical amplifiers. *Electronics Letters*, 40(6):380–381, 2004.

[40] B. C. Collings, M. L. Mitchell, L. Boivin, and W. H. Knox. A 1021 channel WDM system. *IEEE Photonics Technology Letters*, 12(7):906–908, 2000.

[41] H. Ono, M. Yamada, T. Kanamori, S. Sudo, and Y. Ohishi. $1.58\,\mu$m band fluoride-based Er^{3+}-doped fibre amplifier for WDM transmission systems. *Electronics Letters*, 33(17):1471–1472, 1997.

[42] A. J. G. Ellison, D. E. Goforth, B. N. Samson, J. D. Minelly, J. P. Trentelman, and D. L. McEnroe. Extending the L-band to 1620 nm using MCS fiber. In *Proceedings of Optical Fiber Communication Conference, paper: TuA2*, 2001.

[43] M. A. Arbore, Y. Zhou, G. Keaton, and T. Kane. 34 dB gain at 1500 nm in S-band EDFA with distributed ASE suppression. In *Proceedings of European Conference on Optical Communication, paper: 02.2.2*, 2002.

[44] B. Cole and M. L. Dennis. S-band amplification in a thulium doped silicate fiber. In *Proceedings of Optical Fiber Communication Conference, paper: TuQ3*, 2001.

[45] A. Cucinotta, F. Poli, and S. Selleri. Gain characteristics of thulium-doped tellurite fiber amplifiers by dual-wavelength (800 nm+1064 nm) pumping. In *Proceedings of Optical Fiber Communication Conference, paper: FB1*, 2003.

[46] T. Komukai, T. Yamamoto, T. Sugawa, and Y. Miyajima. $1.47 \mu m$ band Tm^{3+} doped fluoride fibre amplifier using a $1.064 \mu m$ upconversion pumping scheme. *Electronics Letters*, 29(1):110–112, 1993.

[47] R. M. Percival and J. R. Williams. Highly efficient $1.064 \mu m$ upconversion pumped $1.47 \mu m$ thulium doped fluoride fibre amplifier. *Electronics Letters*, 30(20):1684–1685, 1994.

[48] E. Zhang, S. Wilson, D. Crippa, R. Di Muro, and A. Maroney. Tm-doped fiber amplifiers in the 1480 nm region with 980 nm/1550 nm pumps. In *Proceedings of the Conference Optical Amplifier and their Applications, paper: OWB2*, 2001.

[49] F. Roy. Recent advances in thulium-doped fiber amplifiers. In *Proceedings of Optical Fiber Communication Conference, paper: ThZ1*, 2002.

[50] S. Aozasa, T. Sakamoto, T. Kanamori, K. Hoshino, and M. Shimizu. Gain-shifted thulium-doped fibre amplifiers employing novel high concentration doping technique. *Electronics Letters*, 36(5):418–419, 2000.

[51] J. Masum-Thomas. A 70 nm wide S-band amplifier by cascading TDFA and Raman fibre amplifier. In *Proceedings of Optical Fiber Communication Conference, paper: WdD9*, 2001.

[52] K. Shikano, M. Shimizu, K. Kato, H. Masuda, A. Mori, and K. Oikawa. Ultra-wide-band hybrid tellurite/silica fiber Raman amplifier. In *Proceedings of Optical Fiber Communications Conference, paper: ThB6*, 2002.

[53] A. Kobyakov and M. Vasilyev. Effect of pump depletion on the noise figure of distributed Raman amplifiers. In *Proceedings of CLEO/QELS Conference, paper: CWL3*, 2002.

[54] H. Scholze. *Glas: Natur, Struktur und Eigenschaften (engl. Glass: nature, structure and properties)*, chapter 2: *Natur und Struktur des Glasses (engl. Nature and structure of the glass)*. Springer Verlag, Berlin, Heildelberg, New York, 2 edition, 1977.

[55] http://cst-www.nrl.navy.mil/lattice.

[56] A. Bahl and U. Unrau. *Optische Kommunikationstechnik (engl. Optical communications technology)*, chapter 22.9: *Glaser mit niedriger Phononenergie (LPE-Gläser) (engl. Low phonon energy glasses)*. Editors: E. Voges, K. Petermann, Springer Verlag, Berlin Heidelberg, 2002.

[57] M. Poulain. *Fluoride glasses*, chapter 2: *Glass systems and structures*. Critical reports on applied chemistry, vol. 27. Editor: A. E. Comyns, John Willey & Sohns, Chichester, New York, 2002.

[58] R. Caspary. *Applied rare-earth spectroscopy for fiber laser optimization*. Doctoral disertation, Gemeinsame Fakultät für Maschinenbau und Elektrotechnik der Technische Universität Braunschweig, 2001.

[59] B. Sartorius, C. Bornholdt, O. Brox, U. Feiste, and M. Möhrle. Towards the all-optical 3R regenerator: performance of the optical clock. In *Proceedings of European Conference on Optical Communication, paper: ThA2*, 1999.

[60] P. C. Becker, N. A. Olsson, and J. R. Simpson. *Erbium doped fiber amplifiers. Fundamentals and technology*, chapter 4.6: Er^{3+}-Er^{3+} *interaction effects*. Academic Press, 1999.

[61] J. L. Gimlett and N. K. Cheung. Effects of phase-to-intensity noise conversion by multiple reflections on gigabit-per-second DFB laser transmission systems. *IEEE Journal of Lightwave Technology*, 7(6):888–895, 1989.

[62] D. M. Baney, P. Gallion, and Tucker R. S. Theory and measurement techniques for the noise figure of optical amplifiers. *Optical Fiber Technology*, 6:122–154, 2000.

[63] M. L. Dakss, B. Pedersen, G. R. Joyce, and W. J. Miniscalco. Signal output power and noise in erbium-doped fiber power amplifiers. In *Proceeding of Society of Photo-Optical Instrumentation Engineers Conference*, volume 1581, pages 235–250, 1991.

[64] M. Alonso and E. J. Finn. *Quantenphysik (engl. Quantum physics)*. Addison-Wesley Publishing Company, Second edition, 1988.

[65] B. R. Judd. Optical absorption intensities of rare-earth ions. *Physical Review*, 127(3):750–761, 1962.

[66] G. S. Ofelt. Intensities of crystal spectra of rare-earth ions. *Journal of Chemical Physics*, 37(3):511–520, 1962.

[67] M. M. Kozak, D. Goebel, R. Caspary, and W. Kowalsky. Spectroscopic properties of thulium doped zirconium fluoride and indium fluoride glasses. *Journal of Non-Crystalline Solids*, 351(24-26):2009–2021, 2005.

[68] M. Poulain, M. Poulain, J. Lucas, and P. Brun. Verres fluores au tetrafluorure de zirconium - proprietes optiques d'un verre dope au Nd^{3+} (engl. Fluoride Glasses Containing Tetrafluoride of Zirconium - Optical Properties of a Glass doped with Nd^{3+}). *Materials Research Bulletin*, 10:243–246, 1975.

[69] S. F. Carter, P. W. France, M. W. Moore, and C. R. Day. Crystallization in a ZBLANP core glass and optical fibres. *Material Science Forum*, 19-20:511–513, 1987.

[70] H. M. Pask, A. C. Tropper, D. C. Hanna, B. N. Samson, R. D. T. Lauder, P. R. Barber, L. Reekie, J. L. Archambault, S. T. Davey, and D. Szebesta. Upconversion laser action in Pr^{3+}-doped ZBLANP fiber pumped by an Yb-doped silica fiber laser. In *Advanced Solid State Laser, Conference Proceedings, paper: ATuD1*, 1994.

[71] T. Sakamoto, M. Shimizu, T. Kanamori, Y. Oshi, Y. Terunuma, M. Yamada, and S. Sudo. Tm-Ho-doped ZBLYAN fiber amplifiers for $1.4\,\mu$m-band. In *Technical Digest of Fifth Optoelectronic Conference, paper: 13B2-2*, 1994.

[72] M. Baricco, L. Battezzati, M. Braglia, G. Cocito, M. Gava, J. Kraus, and S. Mosso. Nucleation and growth of crystals in a ZBLYALiPb glass. *Journal of Non-Crystalline Solids*, 289(1-3):144–150, 2001.

[73] C. Jacoboni, A. le Bail, and R. de Pape. Fluoride glasses of 3d transition metals. *Glass Technology*, 24(3):164–167, 1983.

[74] J.-J. Videau, B. Dubois, and J. Portier. Chimie de l'etat solide. - Verres a base de fluorure d'indium. (engl. Solid-State Chemistry: Glasses on the Basis of Indium Fluoride). *Comptes Rendus de l'Academie des Scieces*, 297:483–485, 1983.

[75] A. Brenier, C. Pedrini, B. Moine, J. L. Adam, and C. Pledel. Fluorescence mechanisms in Tm^{3+} singly doped and Tm^{3+}, Ho^{3+} doubly doped Indium-based fluoride glasses. *Physical Review B - Condensed Matter*, 41(8):5364–5371, 1990.

[76] W. Ryba-Romanowski, S. Golab, G. Dominiak-Dzik, M. Zelechower, and J. Gabrys-Pisarska. Excited state relaxation dynamics and non-radiative energy transfer in fluoroindate glass singly doped with thulium and doubly doped with thulium and terbium. *Journal of Alloys & Compounds*, 325:215–222, 2001.

[77] L. Wetenkamp. *Charakterisierung von laseraktiv dotierten Schwermetallfluorid-Gläsern und Faserlasern (engl.Characterization of Laser-actively Doped Heavy-metal Fluoride Glasses and Fiber Lasers)*. Doctoral disertation, Gemeinsame Fakultät für Maschinenbau und Elektrotechnik der Technische Universität Braunschweig, 1991.

[78] L. Wetenkamp, T. Westendorf, G. F. West, and A. Kober. The effect of small composition changes on the refractive index and material dispersion in ZBLAN heavy-metal fluoride glass. *Material Science Forum*, 32-33:471–476, 1988.

[79] D. R. Lide. *CRC Handbook of chemistry and physics*. CRC Press, Boca Raton, 76th edition, 1995-1996.

[80] M. Pollnau, J. Schneider, U. B. Unrau, W. Luthy, and H. P. Weber. Pr^{3+} co-doped $2.8\,\mu$m erbium fiber laser. In *Proceedings of the CLEO/Europe-EQEC Conference, paper: 13B2-2*, 1996.

[81] J. Schneider, C. Carbonnier, and U. B. Unrau. Characterization of a Ho^{3+}-doped fluoride fiber laser with a $3.9\,\mu$m emission wavelength. *Applied Optics*, 36(33):8595–8600, 1997.

[82] R. M. Percival, D. Szebesta, C. P. Seltzer, S. D. Perrin, S. T. Davey, and M. Louka. A $1.6\,\mu$m pumped $1.9\,\mu$m thulium doped fluoride fiber laser and amplifier of very high efficiency. *IEEE Journal of Quantum Electronics*, 31(3):489–493, 1995.

[83] W. C. Hasz, J. H. Whang, and C. T. Moynihan. Comparison of physical properties of ZrF_4- and HfF_4-based melts and glasses. *Journal of Non-Crystalline Solids*, 161:127–132, 1993.

[84] G. Lei, J. E. Anderson, M. I. Buchwald, B. C. Edwards, and R. I. Epstein. Determination of spectral linewidths by Voigt probes in Yb^{3+}-doped fluorozirconate glasses. *Physical Review B - Condensed Matter*, 57(13):7673–7678, 1998.

[85] M. Poulain. *Fluoride glass fiber optics*, chapter 1: *Fluoride glass composition and processing*. Editors: I. D. Aggarwal, G. Lu, Academic Press, 1991.

[86] Y. Messaddeq, A. Delben, M. A. Aegerter, A. Soufiane, and M. Poulain. New fluoroindate glass compositions. *Journal of Material Research*, 8(4):885–889, 1993.

[87] H. Inoue, K. Soga, and A. Makishima. Simulation of the optical properties of Tm:ZBLAN glass. *Journal of Non-Crystalline Solids*, 306(1):17–29, 2002.

[88] E. R. Taylor, L. N. Ng, N. P. Sessions, and H. Buerger. Spectroscopy of Tm^{3+}-doped tellurite glasses for 1470 nm fiber amplifier. *Journal of Applied Physics*, 92(1):112–117, 2002.

[89] S. D. Jackson and T. A. King. Theoretical modeling of Tm-doped silica fiber lasers. *IEEE Journal of Lightwave Technology*, 17(5):948–956, 1999.

[90] Y. Akasaka, H. Inoue, S. S. Yam, and Y. Kubota. Thulium doped fiber amplifier for the first window from 790 nm to 850 nm with 690 nm/1400 nm dual pumping. In *Proceedings of the OFC/NFOEC Conference, paper: OWF3*, 2005.

[91] A. Florez, M. Florez, Y. Messaddeq, M. A. Aegerter, and P. Porcher. Application of standard and modified Judd-Ofelt theories to thulium doped fluoroindate glass. *Journal of Non-Crystalline Solids*, 247:215–221, 1999.

[92] J. Gabrys-Pisarska, M. Zelechower, W. A. Pisarski, S. Golab, M. Baluka, and W. Ryba-Romanowski. Optical properties of fluoroindate glasses doped with rare earth ions. *Optica Applicata*, 30(4):517–528, 2000.

[93] C. Guery, J. L. Adam, and J. Lucas. Optical properties of Tm^{3+} ions in indium-based fluoride glasses. *Journal of Luminescence*, 42:181–189, 1988.

[94] J. Mendez-Ramos, F. Lahoz, I. R. Martin, A. B. Soria, A. D. Lozano-Gorrin, and V. D. Rodriguez. Optical properties and upconversion in Yb^{3+}-Tm^{3+} co-doped oxyfluoride glasses and glass ceramics. *Molecular Physics*, 101(7):1057–1065, 2003.

[95] K. Kadono, T. Yazawa, M. Shojiya, and Y. Kawamoto. Judd-Ofelt analysis and luminescence property of Tm^{3+} in $Ga_2S_3 - GeS_2 - La_2S_3$ glasses. *Journal of Non-Crystalline Solids*, 274(1-3):75–80, 2000.

[96] S. Guy, A. M. Jurdyc, B. Jacquier, and W. M. Meffre. Excited states Tm spectroscopy in ZBLAN glass for S-band amplifier. *Optics Communications*, 250(4-6):344–354, 2005.

[97] J. Q. Xu, M. Prabhu, J. R. Lu, K. Ueda, and D. Xing. Efficient double-clad thulium-doped fiber laser with a ring cavity. *Applied Optics*, 40(12):1983–1988, 2001.

[98] M. M. Kozak, D. Goebel, T. Kowalsky, and C. Caspary. Excited state absorption spectroscopy for thulium-doped zirconium fluoride fiber. *submitted to Optics Communications*, 2005. doi:10.1016/j.optcom.2005.08.012.

[99] T. et al Sakamoto. Thulium-doped fluoride fiber amplifiers for 1.4 µm and 1.6 µm operation. In *Proceedings of the Optical Amplifiers and Their Applications Conference, paper: ThC3*, 1996.

[100] D. E. McCumber. Einstein relations connecting broadband emission and absorption spectra. *Physical Review*, 136(4A):954–957, 1964.

[101] W. L. Barnes, R. I. Laming, E. J. Tarbox, and P. R. Morkel. Absorption and emission cross section of Er^{3+} doped silica fibers. *IEEE Journal of Quantum Electronics*, 27(4):1004–1010, 1991.

[102] M. Naftaly, S. Shen, and A. Jha. Spectroscopy of Nd^{3+}, Tm^{3+} and Er^{3+} ions in tellurite glasses and fibres for broadband optical fibre amplifiers in the 1350 nm to 1600 nm range. In *Proceedings of SPIE Conference on Design, Fabrication and Characterisation of Photonic Devices*, volume 3896, 1999.

[103] P. Peterka, B. Faure, W. Blanc, M. Karasek, and B. Dussardier. Theoretical modelling of S-band thulium - doped silica fibre amplifiers. In *Proceedings of 11th International Workshop on Optical Waveguide Theory and Numerical Modelling*, 2003.

[104] E. M. Arsent'eva, N. V. Nikonorov, N. V. Ovcharenko, A. V. Chukharev, A. S. Rokhmin, and A. K. Przhevuskii. Spectroluminescence properties of highly refractive thulium-doped laser glasses. *Journal of Optical Technology*, 70(11):782–788, 2003.

[105] W. J. Minisalco. *Rare earth doped fiber lasers and amplifiers*, chapter 2: *Optical and electronic properties of rare earth ions in glasses*. Editor: M. J. F.Digonnet, Marcel Dekker, Inc., 1993.

[106] J. Nilsson, S. U. Alam, J. A. Alvarez-Chavez, P. W. Turner, W. A. Clarkson, and A. B. Grudinin. High-power and tunable operation of erbium-ytterbium co-doped cladding-pumped fiber lasers. *IEEE Journal of Quantum Electronics*, 39(8):987–994, 2003.

[107] D. L. Dexter. A theory of sensitized luminescence in solids. *Journal of Chemical Physics*, 21(5):836–850, 1953.

[108] I. R. Martin, V. D. Rodriguez, R. Alcala, and R. Cases. Cross-relaxation for Tm^{3+} ions in Indium-based glasses. *Journal of Chemical Physics*, 161:294–296, 1993.

[109] B. Villacampa, V. M. Orera, R. I. Merino, R. Cases, P. J. Alonso, and R. Alcala. Optical properties of $ZnF2 - CdF2$ glasses doped with 4f ions. *Materials Research Bulletin*, 26(8):741–748, 1991.

[110] B. M. Walsh and N. P. Barnes. Comparison of Tm : ZBLAN and Tm : silica fiber lasers; Spectroscopy and tunable pulsed laser operation around 1.9 μm. *Journal of Alloys & Compounds*, 78(3-4):325–333, 2004.

[111] K.-S. Lim, P. Babu, C. K. Jayasankar, S. Lee, V.-T. Pham, and H.-J. Seo. Optical spectroscopy of thulium-doped oxyfluoroborate glass. *Journal of Alloys & Compounds*, 385(1-2):12–18, 2004.

[112] S. K. Sheem and T. G. Giallorenzi. Singlemode fiber-optical power divider: encapsuled etching technique. *Optics Letters*, 4(1):29–31, 1979.

[113] S. Masuda and T. Iwama. Single-mode fiber optic directional coupler. *Applied Optics*, 21(19):3484–3488, 1982.

[114] Y. Murakami and S. Sudo. Coupling characteristics measurements between curved waveguides using a two-core fiber coupler. *Applied Optics*, 20(3):417–422, 1981.

[115] R. A. Bergh, G. Kottler, and Shaw H. J. Single-mode fibre optic directional coupler. *Electronics Letters*, 16(7):260–261, 1980.

[116] B. P. Pal. *Electromagnetic fields in unconventional materials and structures*, chapter 9.3: *Side-polished fiber half-couplers and components*, pages 387–405. Wiley Series in Microwave and Optical Engineering. Editors: O. N. Singh, A. Lakhtakia, A Wiley-Interscience Publication, New York, 2000.

[117] I. Yokohama, K. Okamoto, and Noda J. Fiber-coupler fabrication with automatic fusion-elongation processes for low excess loss and high coupling-ratio accuracy. *IEEE Journal of Lightwave Technology*, LT-5(7):910–915, 1987.

[118] Y. Takeuchi, M. Hirayama, S Sumida, and O. Kobayashi. Characteristics of ceramic microheater for fiber coupler fabrication. *Japanese Journal of Applied Physics*, 37(6B):3665–3668, 1998.

[119] J. Bures, S. Lacroix, and J. Lapierre. Analyse d'un coupleur bidirectionnel a fibres optiques monomodes fusionnées (engl. Analyse of the single-mode bidirectional optical fiber coupler). *Applied Optics*, 22(12):1918–1922, 1983.

[120] A. Ankiewicz, A. W. Snyder, and X.-H. Zheng. Coupling between parallel optical fiber cores - critical examination. *IEEE Journal of Lightwave Technology*, LT-4(9):1317–1323, 1986.

[121] Q. Wang, S. L. He, F. R. Chen, and A. Biswas. An effective and accurate method for the design of directional couplers. *IEEE Selected Topics in Quantum Electronics*, 8(6):1233–1238, 2002.

[122] A. Biswas. Theory of optical couplers. *Optical and Quantum Electronic*, 35(3):221–235, 2003.

[123] A. Grellier. *Characterisation of optical fibre tapering using a* CO_2 *laser*. Doctoral disertation, Subject of Physics, The University of Kent at Canterbury, 2000.

[124] W. J. Stewart and J. D. Love. Design limitation on tapers and couplers in single mode fibers. In *Proceedings of IOOC-ECOC Conference*, pages 559–562, 1985.

[125] J.D. Love and W. M. Henry. Quantifing loss minimisation in single-mode fibre tapers. *Electronics Letters*, 22(17):912–914, 1986.

[126] S. Lacroix, R. Bourbonnais, F. Gonthier, and J. Bures. Tapered monomode optical fibers: understanding large power transfer. *Applied Optics*, 24(17):4421–4425, 1986.

[127] J.D. Love, W. M. Henry, W. J. Stewart, R. J. Black, S. Lacroix, and F. Gonthier. Tapered single-mode fibres and devices; 1. Adiabaticity criteria. In *IEE Proceedings: J - Optoelectronics*, volume 138(5), pages 343–354, 1991.

[128] T. A. Birks. *Optical fiber taper components*. Doctoral disertation, University of Limerick, Irland, 1990.

[129] M. D. Feit and J. A. Fleck Jr. Light propagation in graded-index optical fibers. *Applied Optics*, 17(24):3990–3998, 1978.

[130] M. D. Feit and J. A. Fleck Jr. Propagating beam theory of optical fibers cross coupling. *Journal of Optical Society of America*, 71(11):1361–1372, 1981.

[131] V. J. Tekippe. Passive fiber-optic components made by the fused biconical taper process. *Fiber and Integrated Optics*, 9:97–123, 1990.

[132] A. Mori, Y. Ohishi, and S. Sudo. Erbium-doped tellurite glass fibre laser and amplifier. *Electronics Letters*, 33(10):863–864, 1997.

[133] A. Mori, T. Sakamoto, K. Kobayashi, K. Shikano, K. Oikawa, K. Hoshino, T. Kanamori, Y. Ohishi, and M. Shimizu. $1.58\,\mu m$ broad-band erbium-doped tellurite fiber amplifier. *IEEE Journal of Lightwave Technology*, 20(5):822–827, 2002.

[134] M. Yamada, T. Kanamori, Y. Terunuma, K. Oikawa, M. Shimizu, S. Sudo, and K. Sagawa. Fluoride-based erbium-doped fiber amplifier with inherently flat gain spectrum. *IEEE Photonics Technology Letters*, 8(7):882–884, 1996.

[135] J. Labs and D. Krabe. Untersuchung von Verbindungstechnologien für das nichtlösbare Verbindungen von Fasern zur Leitung von Strahlung mit $\lambda > 2\mu m$ (engl. Research on joining technologies for permanent splices of fibers for guiding radiation with $\lambda > 2\mu m$). *Report BMBF*, 13N6768, 1998.

[136] B. B. Harbison, W. I. Roberts, and I. D. Aggarwal. Fusion splicing of heavy metal fluoride glass optical fibre. *Electronics Letters*, 25(18):1214–1215, 1989.

[137] L. Rivoallan and J. Guilloux. Fusion splicing of fluoride glass optical fibre with CO_2 laser. *Electronics Letters*, 24(12):756–757, 1988.

[138] L. Rivoallan, J. Guilloux, and P. Lamouler. Monomode fibre fusion splicing with CO_2 laser. *Electronics Letters*, 19(2):54–55, 1983.

[139] Patent DE OS 2823787 GO2 B5/14.

[140] M. Kihara, S. Tomita, and M. Matsumoto. Loss characteristics of thermally diffused expanded core fiber. *IEEE Photonics Technology Letters*, 4(12):1390–1391, 1992.

[141] NTT-AT. Technical information of TEC fiber, 2002.

[142] J. Labs. *Verbindungstechnik für Lichtwellenleiter. Schweißen von Glasfasern (engl. Joining techniques for waveguides. Fibers splicing.)*, chapter 3: *Verbindung (Kopplung) Lichtwellenleiter-Lichtwellenleiter* (engl. Connection waveguide-waveguide). DVS-Verlag GmbH, Düsseldorf, 1989.

[143] K. Shiraishi, T. Yanagi, and S. Kawakami. Light-propagation characteristics in thermally diffused expanded core fibers. *IEEE Journal of Lightwave Technology*, 11(10):1584–1591, 1993.

[144] H. Hanafusa, M. Horiguchi, and J. Noda. Thermally diffused expanded core fibres for low-loss and inexpensive photonic components. *Electronics Letters*, 27(21):1968–1971, 1991.

[145] J. S. Harper, C. P. Botham, and S. Hornung. Tapers in single-mode optical fibre by controlled core diffusion. *Electronics Letters*, 24(4):245–246, 1988.

[146] D. Marcuse. Loss analysis of single mode fiber splices. *Bell Systems Technical Journal*, 56(5):703–718, 1977.

[147] Y. Nishida, K. Fujiura, K. Hoshino, M. Shimizu, M. Yamada, K. Nakagawa, and Y. Ohishi. Reliability of fluoride fiber module for optical amplifier use. *IEEE Photonics Technology Letters*, 11(12):1596–1598, 1999.

[148] Y. Yamada, F. Hanawa, T. Kitoh, and T. Maruno. Low-loss and stable fiber-to-waveguide connection utilizing UV curable adhesive. *IEEE Photonics Technology Letters*, 4(8):906–908, 1992.

[149] P. W. France, M. G. Drexhage, J. M. Parker, M. W. Moore, S. F. Carter, and J. V. Wright. *Fluoride glass optical fibres*, chapter 1: *Perspective and overview*. Blackie, Glasgow and London; CRC Press, 1990.

[150] M. R. Shahriari, T. Iqbal, G. H. Sigel, and G. Merberg. Synthesis and characterization of aluminium fluoride-based glasses and optical fibers. *Material Science Forum*, 32-33:99–106, 1988.

[151] J. S. Sanghera and I. D. Aggarwal. *Infrared fiber optics*, chapter 3: *Fluoride glass-based fibers*. CRC Press Inc., Boca Raton, 1998.

[152] http://telecom-info.telcordia.com.

[153] E. A. Y. Fisher. Adhesives for fiber optics assembly: making the right choice. *Photonics Spectra*, 2:82–89, 2003.

[154] H. Renner. *Optische Kommunikationstechnik (engl. Optical communications technology)*, chapter 4: *Einmodenfasern* (engl. Single mode fibers). Editors: E. Voges, K. Petermann, Springer Verlag, Berlin Heidelberg, 2002.

[155] E. Brinkmeyer. *Optische Kommunikationstechnik (engl. Optical communications technology)*, chapter 3: *Optische Fasern: Grundlagen* (engl. Optical fibers: basics). Editors: E. Voges, K. Petermann, Springer Verlag, Berlin Heidelberg, 2002.

[156] J. R. Armitage. Three-level fiber laser amplifier: a theoretical model. *Applied Optics*, 27(23):4831–4836, 1988.

[157] C. Barnard, P. Myslinski, J. Chrostowski, and M. Kavehrad. Analytical model for rare-earth-doped fiber amplifiers and lasers. *IEEE Journal of Quantum Electronics*, 30(8):1817–1830, 1994.

[158] R. M. Jopson and A. A. M. Saleh. Modeling of gain and noise in erbium-doped fiber amplifiers. In *Fiber Laser Sources and Amplifiers III, Proceedings SPIE*, volume 1581, pages 114–119, 1991.

[159] C. R. Giles and E. Desurvire. Modeling erbium-doped fiber amplifiers. *IEEE Journal of Lightwave Technology*, 9(2):271–283, 1991.

[160] P. Krummrich. *Praseodym-dotierte Faserverstärker für den Wellenlengenbereich um $1,3\,\mu$m (engl. Praseodymium-doped fiber amplifier for the wavelength region around $1.3\,\mu$m)*. Doctoral disertation, Gemeinsame Fakultät für Maschinenbau und Elektrotechnik der Technische Universität Braunschweig, 1995.

[161] M. M. Kozak, R. Caspary, and U. B. Unrau. Computer aided EDFA design, simulation and optimization. In *Proceedings of International Conference on Transparent Optical Networks, paper: We.B.2*, 2001.

[162] T. P. Baraniecki, M. M. Kozak, U. B. Unrau, E. M. Pawlik, and K. M. Abramski. Comparison of laboratory measurements on an EDFA with simulation results obtained using EDFA_Design®. In *Proceedings of International Conference on Transparent Optical Networks, paper: We.P.24*, 2001.

[163] W. J. Lee and B. Min. Study on the pumping wavelength dependency of S^+-band Fluoride based Thulium doped fiber amplifiers. In *Proceedings of Optical Fiber Communication Conference, paper: TuQ5*, 2001.

[164] A. Rieznik, G. Wiederhecker, H. Fragnito, M. Carvalho, M. Sundheimer, A. Gomes, C. Bastos-Filho, and J. Martins-Filho. Black box model for thulium doped fiber amplifiers. In *Proceedings of Optical Fiber Communication Conference, paper: FB2*, 2003.

[165] F. Roy, A. Le Sauze, P. Baniel, and D. Bayart. $0.8\,\mu$m$+1.4\,\mu$m pumping for gain-shifted TDFA with power conversion efficiency exceeding 50 %. In *Proceedings of Conference Optical Amplifiers and Their Applications, paper: PD4*, 2001.

[166] T. Kasamatsu and Y. Yano. Tm-doped fiber amplifiers for S-band. In *Proceedings of Conference Optical Amplifiers and Their Applications, paper: OWB1*, 2001.

[167] R. Caspary. Optisches Verstärkersystem (engl. Optical amplifier system). *Patent application: 103 27 947.4, Priority date: 20.06.2003*.

[168] P. F. Wysocki, N. Park, and D. Digiovanni. Dual stage erbium doped, erbium/ytterbium codoped fiber amplifier with up to $+26$ dBm output power and a $0.017\,\mu$m flat spectrum. *Optics Letters*, 21(21):1744–1746, 1996.

[169] H. Zellmer, P. Riedel, and A. Tunnermann. Visible upconversion lasers in praseodymium ytterbium doped fibers. *Applied Physics B - Lasers and Optics*, 69(5-6):417–421, 1999.

[170] R. Caspary, T. P. Baraniecki, M. M. Kozak, and W. Kowalsky. Visible upconversion fiber lasers in ring configuration. In *SPIE Conference Optics and Optoelectronics, paper: 5958-27*, 2005.

[171] I. R. Martin, V. D. Rodriguez, Y. Guyot, S. Guy, G. Boulon, and M. F. Joubert. Room temperature photon avalanche upconversion in Tm^{3+}-doped fluoroindate glasses. *Journal of Physics - Condensed Matter*, 12(7):1507–1516, 2000.

[172] Y. S. Han, D. J. Lee, and J. Heo. $1.48\,\mu$m emission properties and the cross-relaxation mechanism in chalcohalide glass doped with Tm^{3+}. *Journal of Non-Crystalline Solids*, 321(3):210–216, 2003.

[173] H. Inoue, K. Moriwaki, N. Tabata, K. Soga, A. Makshima, and Y. Akasaka. Simulation of the optical properties of Tm: ZBLAN glass. II. Energy transfer between Tm^{3+} ions under single- and dual - wavelength excitation. *Journal of Non-Crystalline Solids*, 336(2):135–147, 2004.

[174] M. M. Kozak, W. Kowalsky, and R. Caspary. Low-loss glue splicing method to join silica and fluoride fibres. *Electronics Letters*, 41(16):897–899, 2005.

[175] B. C. Collings and A. J. Silversmith. Avalanche upconversion in LaF_3:Tm^{3+}. *Journal of Non-Crystalline Solids*, 62(6):271–279, 1994.

[176] T. Sakamoto, S. Aozasa, T. Kanamori, K. Hoshino, and M. Shimizu. High gain and low noise TDFA for 1500 nm band employing novel high concentration doping technique. In *Proceedings of Optical Fiber Communication Conference, paper: PD4*, 2000.

[177] A. Gomes, M Carvalho, M. Sundheimer, C. Bastos-Filho, J. Martins-Filho, J von der Weid, and W. Margulis. Low pump power, short-fiber dual-pumped (800 nm+1050 nm) TDFA. In *Proceedings of Optical Fiber Communication Conference, paper: FB5*, 2003.

[178] S. Tessarin, M. Lynch, J. F. Donegan, and G. Maze. Tm^{3+}-doped ZBLAN fibre amplifier at $1.49\,\mu$m with co-operative lasing at $1.88\,\mu$m. *Electronics Letters*, 41(16):899–900, 2005.

[179] M. J. F. Digonnet. *Rare-earth-doped fiber lasers and amplifiers*, chapter 6: *Broadband fiber sources*. Editor: M. J. F. Digonnet, Marcel Dekker Inc. New York, Basel, Hong Kong, Second edition, 2001.

[180] A. Martinez-Rios, A. N. Starodumov, H. Po, Y. Wang, and A. A. Demidov. Efficient operation of double-clad Yb^{3+}-doped fiber lasers with a novel circular cladding geometry. *Optics Letters*, 28(18):1642–1644, 2003.

Publications

Parts of this work were published in papers and presented on the conferences:

[A1] R. Caspary, T. Baraniecki, M. M. Kozak, W. Kowalsky. Recent Progress on S-Band Fiber Amplifiers, *REW-Workshop*, PTB Braunschweig, Germany, (10-11.04.2003)

[A2] M. M. Kozak, R. Caspary and W. Kowalsky. Thulium-doped Fiber Amplifier for the S-Band, *6th International Conference on Transparent Optical Networks, paper: We.B1.6*, Wroclaw, Polen, (04-08.07.2004)

[A3] R. Caspary, M. M. Kozak and W.Kowalsky. Fluoride glass fiber amplifier the S-band, *7th International Conference on Optoelectronics, Fiber Optics and Photonics, paper: FBR 2.2*, Kochi, India, (09-11.12.2004)

[A4] M. M. Kozak, D. Goebel, R. Caspary and W.Kowalsky. Spectroscopic Properties of Thulium Doped Zirconium Fluoride and Indium Fluoride Glasses, *Journal of Non-Crystalline Solids* vol. 351, no. 24-26, pp.: 2009-2021, 2005

[A5] M. M. Kozak, R. Caspary, W. Kowalsky. Thulium-dotierte Faserverstärker: Spektroskopie, Simulation und Messung, (engl. Thulium-doped fiber amplifier: spectroscopy, simulation and measurement) *Diskussionssitzung: Messung und Modellierung in der Optischen Nachrichtentechnik, MMONT 2005*, Hamburg-Blankenese (01-03.06.2005)

[A6] M. M. Kozak, W. Kowalsky, R. Caspary. Low-loss glue-splicing method for joining silica and fluoride fibers for fiber amplifier applications, *Electronics Letters*, vol. 41, no. 16, pp.: 897-899, 2005

[A7] M. M. Kozak, D. Goebel, W. Kowalsky and R. Caspary. Excited State Absorption Spectroscopy for Thulium-Doped Zirconium Fluoride Fiber Optics Communication, *Optics Communication - Article in Press*, DOI:10.1016/j.optcom.2005.08.012

[A8] R. Caspary, T. P. Baraniecki, M. M. Kozak and W. Kowalsky. Visible upconversion fiber lasers in ring configuration *SPIE Conference Optics and Optoelectronics 2005, paper: 5958-27*, Warsaw, Poland (28.08-02.09.2005)

[A9] M. M. Kozak, D. Goebel, R. Caspary and W. Kowalsky. Systematic investigations of avalanche effect in highly thulium-doped fiber amplifier, under review, 2005

[A10] M. M. Kozak, D. Goebel, W. Kowalsky and R. Caspary. Diode-pumped thulium-doped ZBLAN fiber amplifier with the simultaneously operating fiber ring laser at $1.85\,\mu$m, under review, 2005